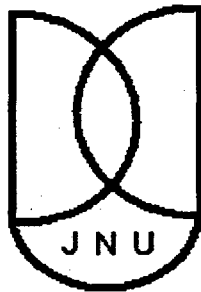


Clustering and Aggregation in Far-From-Equilibrium Systems

Thesis Submitted for the Degree of
DOCTOR OF PHILOSOPHY

Anupam Mukherjee

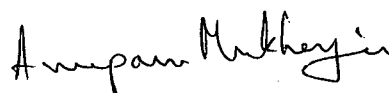


School of Physical Sciences
Jawaharlal Nehru University
New Delhi – 110067.

July 2009

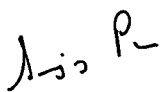
Declaration

I hereby declare that the work carried out in this thesis is entirely original. It was carried out by me in the School of Physical Sciences, Jawaharlal Nehru University, New Delhi. I further declare that it has not formed the basis for the award of any degree, diploma, membership or similar title of any university or institution.



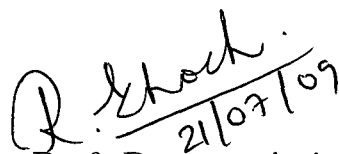
Anupam Mukherjee

School of Physical Sciences,
Jawaharlal Nehru University,
New Delhi - 110067.



Prof. Sanjay Puri

Thesis Supervisor
School of Physical Sciences
Jawaharlal Nehru University
New Delhi - 110067.



Prof. Rupamanjari Ghosh

Dean
School of Physical Sciences
Jawaharlal Nehru University
New Delhi - 110067.

Dedicated to
My Grandparents

Acknowledgments

I take this opportunity to acknowledge and convey my gratefulness in words to all those people who helped and gave me the possibility to complete this thesis.

Foremost, I am deeply indebted to my supervisor Prof. Sanjay Puri for his continuous support and tremendous encouragement during my PhD program. His confidence in me has motivated me to perform to the best of my ability. He has offered me so much advice, patiently listening my doubts, and always guiding me in the right direction. Present form of the thesis would not have been possible without his overall concern throughout the period.

I acknowledge a prolific interaction with Prof. M. Zannetti, who introduced me to the intriguing properties of aging and response function in Ising system during his short visit to SPS. I am grateful to Prof. D. Kumar for his valuable guidance and discussions in various aspects of the domain growth problem. I am also grateful to Prof. G. Barkema and my colleague A. Singh for the collaboration in control of structure formation in phase-separating Systems.

I gratefully acknowledge the financial support I received from the Department of Science & Technology, India, in the form of a research fellowship.

I would also like to thank the faculty, staff and students of SPS for their help and support during the course of my thesis work. In particular, I would like to thank Prof. R. Ghosh for her kind help and encouragement in various stages. Among my fellow colleagues, I would like to mention Awadhesh, Prabhat, Gaurav, Anuja and Shaista. I would also like to thank my friends Vinayak, Udit and Swagato for their support, help and encouragement.

I humbly convey my gratitude to Prof. S. Bhanja, St. Xaviers College, Kolkata and Prof. D. Roy, Jadavpur University for exposing to me the world of physics and

inspiring me to pursue in research as a career.

Last but not the least, I am very grateful to my parents and my sister for their understanding and support during these years. Especially, I would like to give my sincere thanks to my wife, Suparna whose patience and love enabled me to complete this work.

Contents

Declaration	iii
Acknowledgments	iv
1 Introduction to Kinetics of Phase Transitions	1
1.1 Introduction	1
1.1.1 Classification of Nonequilibrium Systems	2
1.1.2 Phase Ordering Dynamics: Two Paradigms	3
1.2 Kinetic Ising Models with Nonconserved Dynamics	7
1.2.1 Spin-Flip Glauber Dynamics	8
1.2.2 Mean-Field Approximation and Time-Dependent Ginzburg-Landau Equation	12
1.3 Kinetic Ising Models with Conserved Dynamics	14
1.3.1 Spin-Exchange Kawasaki Dynamics	14
1.3.2 Mean-Field Approximation and Cahn-Hilliard Equation	18
1.4 Domain Growth in Systems with Non- conserved Kinetics	20
1.4.1 Ginzburg-Landau Free Energy	20

1.4.2	Interface Motion	24
1.4.3	Correlation Functions and Structure Factors	25
1.4.4	Growth Exponents	26
1.4.5	Ohta-Jasnow-Kawasaki Theory	27
1.5	Domain Growth in Systems with Conserved Kinetics	34
1.6	Overview of Chapters 2-4: Our Studies of Kinetics of Phase Transitions	39
2	Control of Structure Formation in Phase-Separating Systems	44
2.1	Introduction	44
2.2	Phase Separation in the Kawasaki-Ising Model with Time-Dependent Temperature	46
2.2.1	First Quench	48
2.2.2	First Heating	52
2.2.3	Second Quench	58
2.2.4	Further Heating and Quenching	63
2.3	Cahn-Hilliard-Cook Model for Phase Separation	66
2.4	Summary and Discussion	73
3	Temperature-Dependence of Domain-Growth Kinetics	75
3.1	Introduction	75
3.2	Domain Growth at Different Quench Temperatures	76
3.3	Time-Scales and Surface Energy	81
3.3.1	Domain Growth at Low Temperatures	82
3.3.2	Domain Growth at at High Temperatures	84
3.3.3	Estimating the Surface Tension	90
3.4	Summary and Discussion	94

4	Aging in Ferromagnets with Quenched Disorder	98
4.1	Introduction	98
4.2	Domain Growth in Disordered Systems	100
4.3	Numerical Results	104
4.3.1	Dynamical Scaling and Growth Laws	104
4.3.2	Autocorrelation and Response Functions	108
4.4	Summary and Discussion	118
5	Introduction to Dynamical Properties of Granular Gases	122
5.1	Granular Systems	122
5.1.1	Dynamical Properties of Granular Gases	123
5.2	Implementation of Event-Driven Algorithm	126
5.2.1	Collision of Particles	127
5.2.2	Sketch of the Algorithm	129
5.3	Improved Event-Driven Algorithm	131
5.3.1	Domain Decomposition	135
5.3.2	Asynchronous Updating	137
5.3.3	Event Management	137
5.3.4	Deletion of Invalid Events	141
5.4	Kinetic Theory of Granular Gases	144
5.4.1	The Boltzmann-Enskog Equation for Inelastic Gases	145
5.5	Overview of Chapter 6: Our Studies of Dynamical Properties of Granular Gases	150
6	Pattern Formation in Freely-Evolving Granular Gases	153
6.1	Introduction	153
6.2	Theoretical Background	155

6.2.1	Haff's Law in Monodispersed Systems	155
6.2.2	Formation of Clusters	160
6.3	Detailed Numerical Results	163
6.3.1	Homogeneous Cooling State and Crossovers	164
6.3.2	Inhomogeneous Cooling State	167
6.3.3	Correlation Functions and Structure Factors	169
6.3.4	Aging in Granular Gases	176
6.4	Haff's Law in Polydispersed Systems	179
6.4.1	Differential Collision Frequency and Differential Collision Rate	179
6.4.2	Case with Different Inelasticities	182
6.4.3	Case with Different Masses	185
6.4.4	Case with Different Initial Temperatures	188
6.5	Summary and Discussion	190

Chapter 1

Introduction to Kinetics of Phase Transitions

1.1 Introduction

Many systems exist in multiple phases, depending on the values of external parameters, e.g., temperature, pressure, etc. Consider a system which has been rendered thermodynamically unstable by a rapid change of parameters. This system will evolve towards its new equilibrium state. This nonequilibrium evolution is usually referred to as *kinetics of phase transitions* or *phase ordering dynamics* or *domain growth* or *coarsening*.

The study of kinetics of phase transitions is of great relevance for both scientific research and technological applications. The characteristics of equilibrium phase transitions have been extensively studied, especially using the framework of renormalization group methods [1, 2]. However our understanding of the nonequilibrium aspects of phase transitions is not so good. Apart from the scientific interests, the study of nonequilibrium phase transitions can suggest novel techniques in materials

manufacturing and processing [3, 4, 5].

1.1.1 Classification of Nonequilibrium Systems

Before we proceed, it is useful to define nonequilibrium or out-of-equilibrium systems. A physical system is said to be out-of-equilibrium if (1) the macroscopic variables (e.g., pressure, temperature, etc.) are time-dependent, or (2) there are macroscopic currents of quantities like heat, mass, charge, etc. We emphasize the term “macroscopic” here as the microscopic constituents of a system (e.g. atoms, molecules) always have complex dynamics. We will subsequently use the term “steady state” to describe systems with macroscopic currents even though the macroscopic variables do not change with time, e.g., fluid confined between two plates at different temperatures. Thus, steady-state systems are not equilibrium systems. Broadly speaking, there are four classes of nonequilibrium systems:

- (1) Systems which are near equilibrium and approaching equilibrium. This class of systems can be studied using linear response theory (LRT), which describes nonequilibrium behavior in terms of equilibrium correlation functions [6].
- (2) Systems which are far-from-equilibrium and approaching equilibrium. This class of systems is typically described by nonlinear evolution equations, and cannot be understood in the framework of LRT.
- (3) Systems which are near-steady-state and approaching a steady state.
- (4) Systems which are far-from-steady-state and approaching a steady state.

We have deliberately avoided making a clear distinction between “near” and “far” in (1)-(4) above. This depends on the particular system being studied. Essentially, a linear description applies when a system is near-equilibrium or near-steady-state.

1.1.2 Phase Ordering Dynamics: Two Paradigms

In this thesis, we are interested in the evolution of a multi-phase system, which is rendered thermodynamically unstable by a rapid change (quench) of external parameters, e.g. temperature, pressure, etc. Let us consider two paradigmatic problems in this context.

First consider a paramagnet \rightarrow ferromagnet transition. The phase diagram of a ferromagnet in the temperature (T) and magnetic field (h) is shown in Figure 1.1.

At high temperature ($T > T_c$) and zero magnetic field ($h = 0$), the spins are randomly oriented, and the resulting magnetization is zero. Below the critical temperature ($T < T_c$), the system prefers to be in a spontaneously magnetized state even if there is no magnetic field.

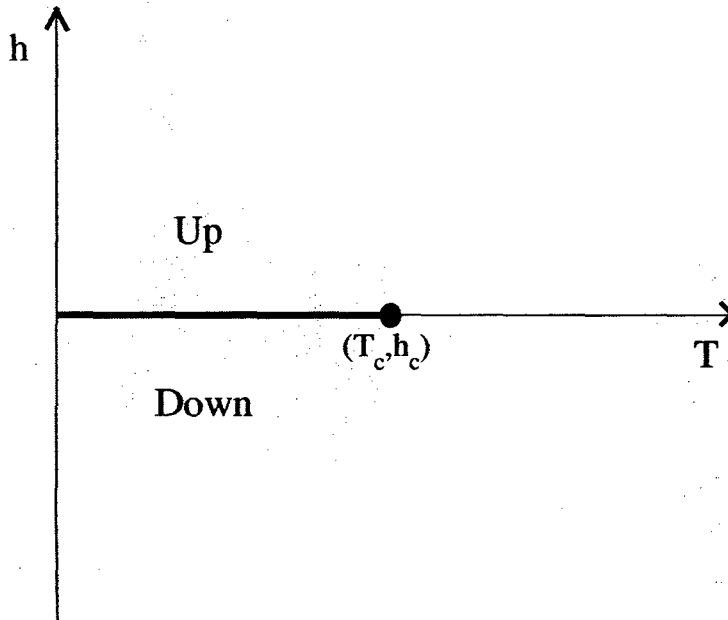


Figure 1.1: Phase diagram of a ferromagnet in the (T, h) -plane. The point $(T_c, h_c = 0)$ corresponds to a second-order critical point. The line $(T < T_c, h_c = 0)$ is a line of first-order phase transitions. When a disordered system is suddenly quenched below the critical temperature, the final equilibrium state is ferromagnetic, i.e., spins are aligned in either the “up” or “down” directions.

Consider a disordered magnet, which is quenched to $T < T_c$ ($h = 0$) at time $t = 0$. At the new temperature, the preferred equilibrium state is the magnetized state. The evolution dynamics of the magnet is shown in Figure 1.2.

The evolution of the system is characterized by the emergence and growth of domains enriched in either up or down spins. As time $t \rightarrow \infty$, the system approaches

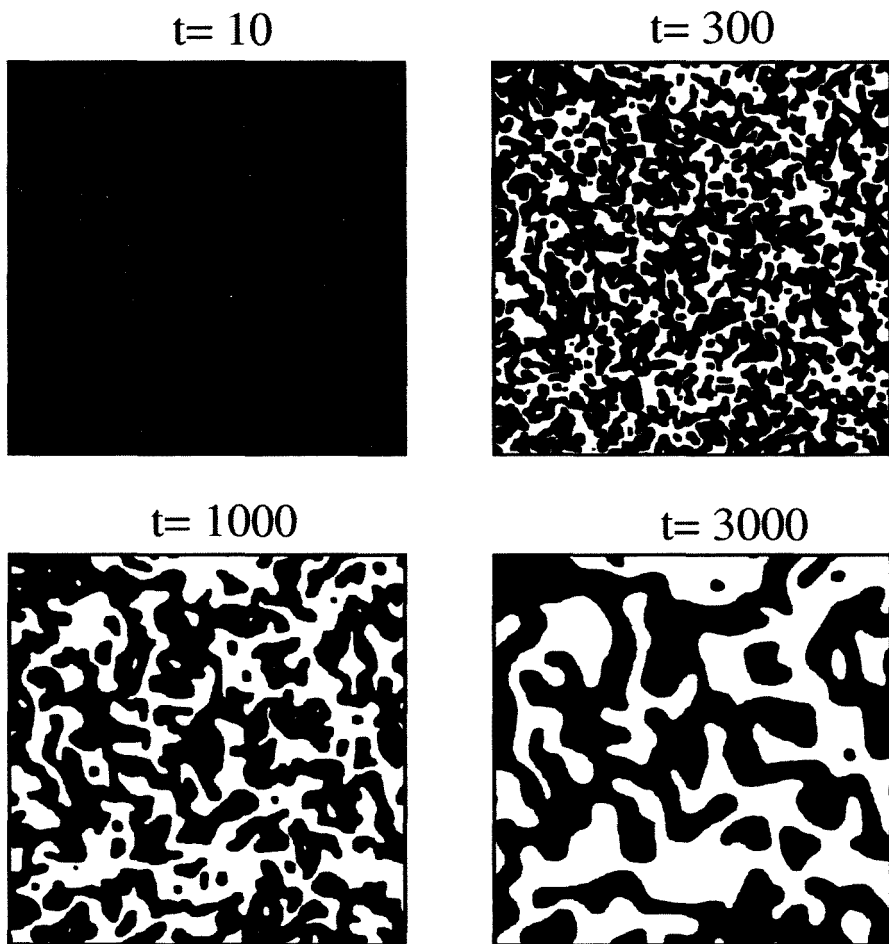


Figure 1.2: The evolution snapshots of a spin-1/2 ferromagnet from a random initial configuration. These snapshots are obtained from a Monte Carlo (MC) simulation of the Ising model with spin-flip Glauber kinetics (see Sec.1.2). Time is measured in units of Monte Carlo steps (MCS). The system temperature is $T = 0.5$. Note that critical temperature for 2d Ising system is $T_c \simeq 2.269$. The black regions denote up-spins and the white regions denote down-spins. The snapshots at later times are statistically self-similar to those at the earlier times, apart from a scale factor.

an equilibrium state, which is a single domain of either up or down spins at $T = 0$. For nonzero T , the equilibrium state consists of a domain with mostly up (and some down) spins or mostly down (and some up) spins.

Next, consider a binary mixture (AB), whose phase diagram is shown in Figure 1.3. The system is homogeneous at high temperatures. When the mixture is quenched below the coexistence curve, the system prefers to be in a phase-separated state or segregated state. In this case, the evolution is characterized by the emergence and growth of A-rich and B-rich domains (see Figure 1.4).

Notice that the evolution shown in Figure 1.4 conserves the initial composition of

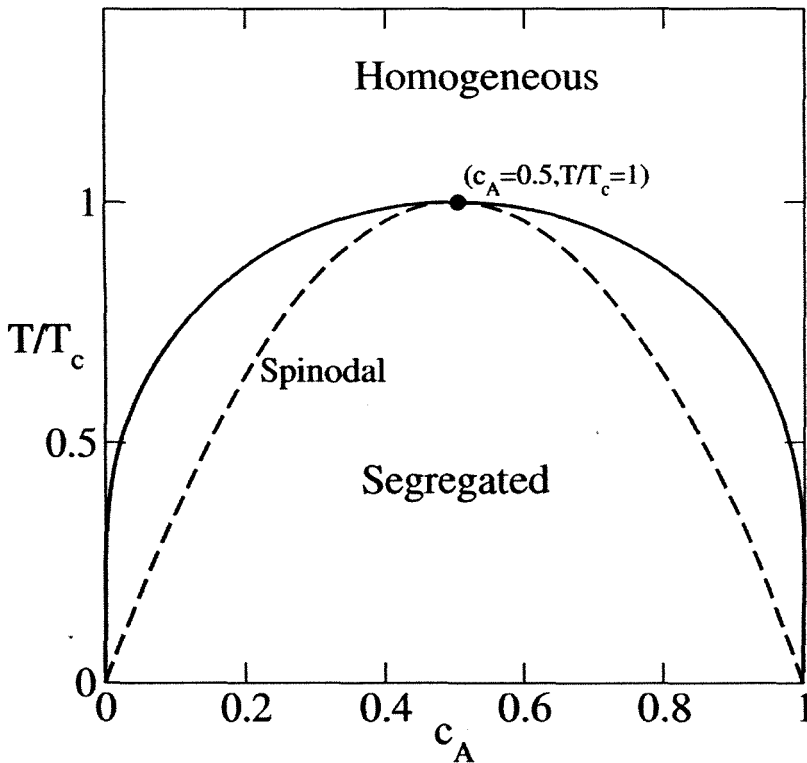


Figure 1.3: Phase diagram of a binary mixture (AB) in the plane of concentration of A (c_A) and temperature (T/T_c). The point ($c_A = 0.5, T/T_c = 1$) is a second-order critical point. When the system is quenched below the critical point, the system segregates into a phase-separated state, characterized by the A-rich and B-rich regions. The homogeneous system is metastable between the coexistence and spinodal curves, and unstable below the spinodal lines.

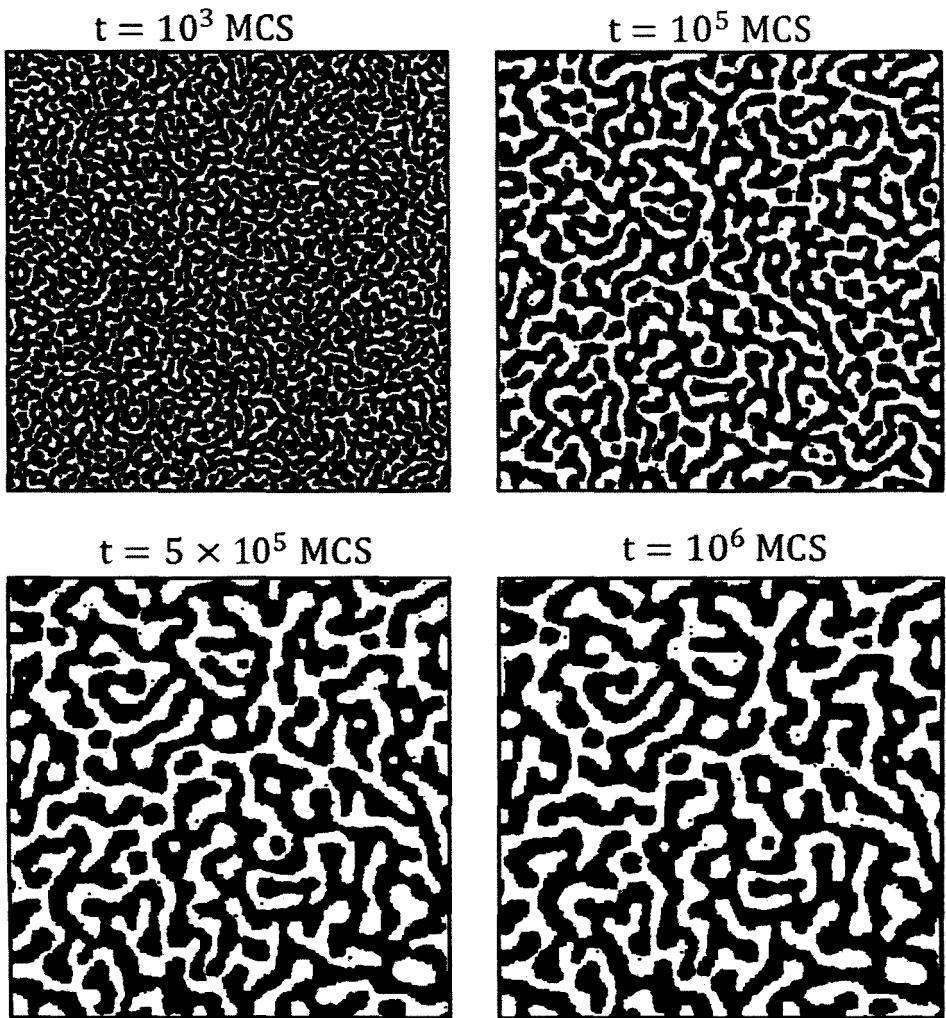


Figure 1.4: Phase ordering dynamics in a binary mixture (AB) after it is quenched below the critical temperature. These snapshots are obtained from MC simulations of the Ising model with spin-exchange Kawasaki kinetics (see Sec.1.3). The system temperature is $T = 1$ (in reduced scale of β). Again, notice that the critical temperature for a 2d binary mixture is $T_c \simeq 2.269$, same as that of spin-1/2 ferromagnet [see Fig. 1.2]. The black and white regions refer to A-rich and B-rich regions. Notice that the evolution dynamics conserves the initial composition of the mixture as neither A or B are destroyed. It is also evident that the patterns evolve are self-similar apart from a scale factor.

the mixture as neither A nor B are destroyed. The evolution of the ordering magnet is referred to as the *case with nonconserved order parameter*, whereas the evolution of the phase-separating mixture is described as the *case with conserved order parameter*.

We will expand on the usage of these terms later.

In most cases, an exact solution for the nonlinear time-dependent evolution of phase ordering systems is not possible. However the presence of domain boundaries or defects in these systems (cf. Figure 1.2 and Figure 1.4) provides a convenient tool to analyze the evolution dynamics [7, 8, 9, 10].

1.2 Kinetic Ising Models with Nonconserved Dynamics

The Ising model is the simplest model for an interacting many-body system. Consider a set of N spins $\{S_i\}$, which are fixed on a lattice with sites $\{i\}$. These spins are coupled through a position-dependent exchange interaction J_{ij} . It is assumed that the interactions are axially symmetric. Hence, only the z -component of the spins is relevant. For simplicity, we consider the case with spin-1/2 particles with projections $S_i^z = \pm 1$ (in units of $\hbar/2$). The Hamiltonian can be written as follows:

$$H = - \sum_{\langle ij \rangle} J_{ij} S_i S_j, \quad \text{where } S_i = \pm 1. \quad (1.1)$$

In Eq. (1.1), we have dropped the superscript z on the spin variables. The subscript $\langle ij \rangle$ denotes a summation over nearest-neighbor pairs only. We usually consider the case when the interactions are independent of the position ($J_{ij} = J$), i.e., the system is translationally invariant. The corresponding Ising Hamiltonian is

$$H = -J \sum_{\langle ij \rangle} S_i S_j, \quad \text{where } S_i = \pm 1. \quad (1.2)$$

The Ising Hamiltonian yields the phase diagram in Figs. 1.1 and 1.3, when studied in the appropriate ensemble. Let us next consider the *kinetics of Ising models*. Again, we restrict ourselves to the spin-1/2 case in Eq. (1.1). The generalization to higher spin models is straightforward. The Ising spin variables do not have any intrinsic dynamics. This can be verified by evaluating the Poisson bracket of the Hamiltonian and an arbitrary spin. Therefore, we associate stochastic dynamics with spin variables by assuming that the system is in contact with a heat bath which generates random spin flips ($S_i \rightarrow -S_i$) [11]. The resulting kinetic Ising model is referred to as the Glauber model [12] and is appropriate for describing the ordering dynamics of paramagnetic \rightarrow ferromagnetic transitions.

1.2.1 Spin-Flip Glauber Dynamics

Let us now consider the evolution of the probability distribution of the spin configuration $\{S_i\}$ for a system evolving via Glauber dynamics. The conditional probability $P(\{S_i^0\}, 0 | \{S_i\}, t)$ is defined as the probability that the i^{th} spin is in state $\{S_i\}$ at time t , provided that the system configuration was $\{S_i^0\}$ at time $t = 0$. Hence, we can write the master equation for evolution of the probability distribution as follows:

$$\begin{aligned} \frac{d}{dt} P(\{S_i\}, t) = & - \sum_{j=1}^N W(S_1, \dots, +S_j, \dots, S_N | S_1, \dots, -S_j, \dots, S_N) P(\{S_i\}, t) \\ & + \sum_{j=1}^N W(S_1, \dots, -S_j, \dots, S_N | S_1, \dots, +S_j, \dots, S_N) P(\{S_i'\}, t), \end{aligned} \quad (1.3)$$

where we have suppressed the argument $(\{S_i^0\}, 0)$. The first term on the RHS denotes the loss term due to a spin-flip $S_j \rightarrow -S_j$, and the second term is the gain of probability due to a spin-flip. Equation (1.3) assumes that the underlying stochastic process is Markovian and the state $\{S_i\}$ at time $t + dt$ depends only on the previous state at t .

The natural choice of the transition probability $[W(\{S_i\})|\{S'_i\}]$ for the change $\{S_i\} \rightarrow \{S'_i\}$ is such that the ensemble approaches the equilibrium distribution $P_{\text{eq}}(\{S_i\})$ as $t \rightarrow \infty$:

$$P_{\text{eq}}(\{S_i\}) = \frac{1}{Z(T, h, N)} \exp[-\beta(H\{S_i\} - hM)], \quad (1.4)$$

where M is the magnetization, $M = \sum_{i=1}^N S_i$; and $\beta = (k_B T)^{-1}$. Here, $Z(T, h, N)$ is the partition function and it is defined as a sum over all configurations:

$$Z = \sum_{\{S_i\}} \exp[-\beta(H - hM)]. \quad (1.5)$$

A sufficient condition to ensure equilibration of the system is the *detailed-balance condition* [13]:

$$W(\{S_i\}|\{S'_i\})P_{\text{eq}}(\{S_i\}) = W(\{S'_i\}|\{S_i\})P_{\text{eq}}(\{S'_i\}). \quad (1.6)$$

Equation (1.6) implies that the ratio of transition probabilities for a move $\{S_i\} \rightarrow \{S'_i\}$ and the inverse move $\{S'_i\} \rightarrow \{S_i\}$ depends only on the enthalpy change $\delta(H - hM)$. Equation (1.6) cannot uniquely specify the transition probability. The two most frequent choices are [14]

$$W(\{S_i\}|\{S'_i\}) = \frac{\lambda}{2} \left[1 - \tanh\left(\frac{\beta\delta(H - hM)}{2}\right) \right], \quad (1.7)$$

or

$$W(\{S_i\}|\{S'_i\}) = \begin{cases} \lambda \exp[-\beta\delta(H - hM)], & \text{if } \delta(H - hM) > 0 \\ \lambda, & \text{if } \delta(H - hM) < 0 \end{cases} \quad (1.8)$$

where λ^{-1} can be interpreted as a unit of Monte Carlo time.

Next we calculate the enthalpy change $\delta(H - hM)$ for the spin-flip Ising model when $S_j \rightarrow -S_j$.

We have:

$$\begin{aligned} (H - hM)_{\text{initial}} &= -JS_j \sum_{L_j} S_{L_j} - hS_j + \text{other terms}, \\ (H - hM)_{\text{final}} &= JS_j \sum_{L_j} S_{L_j} + hS_j + \text{other terms}, \end{aligned} \quad (1.9)$$

where L_j denotes the nearest neighbors of the site j . We also note that the configuration states $\{S_i\}$ and $\{S'_i\}$ differ only in the spin $S_j = -S'_j$. Hence, the change in enthalpy can be written as

$$\delta(H - hM) = 2JS_j \sum_{L_j} S_{L_j} + 2hS_j. \quad (1.10)$$

Thus, using Eqs. (1.3) and (1.7), we can rewrite the master equation as

$$\begin{aligned} \frac{d}{dt} P(\{S_i\}, t) &= -\frac{\lambda}{2} \sum_{j=1}^N \left[1 - S_j \tanh \left(\beta J \sum_{L_j} S_{L_j} + \beta h \right) \right] P(\{S_i\}, t) \\ &+ \frac{\lambda}{2} \sum_{j=1}^N \left[1 + S_j \tanh \left(\beta J \sum_{L_j} S_{L_j} + \beta h \right) \right] P(\{S'_i\}, t). \end{aligned} \quad (1.11)$$

In obtaining Eq. (1.11), we have factored out S_j from the tanh function in Eq. (1.7). This can be done as S_j only takes values $+1$ or -1 . With the help of the master equation, we can now easily obtain the evolution of the magnetization. We define the magnetization as

$$\langle S_k \rangle = \sum_{\{S_i\}} S_k P(\{S_i\}, t). \quad (1.12)$$

Next we multiply both sides of Eq. (1.11) by S_k and sum over all possible configurations.

The resulting equation is

$$\begin{aligned} \frac{d}{dt} \langle S_k \rangle = & -\frac{\lambda}{2} \sum_{j=1}^N \sum_{\{S_i\}} S_k \left[1 - S_j \tanh \left(\beta J \sum_{L_j} S_{L_j} + \beta h \right) \right] P(\{S_i\}, t) \\ & + \frac{\lambda}{2} \sum_{j=1}^N \sum_{\{S_i\}} S_k \left[1 + S_j \tanh \left(\beta J \sum_{L_j} S_{L_j} + \beta h \right) \right] P(\{S'_i\}, t). \end{aligned} \quad (1.13)$$

The RHS of the equation simplifies further if we write the terms $j = k$ and $j \neq k$ separately, and change the variable in the configuration sum of the second term as

$S_j = -S_j$:

$$\begin{aligned} \frac{d}{dt} \langle S_k \rangle = & -\frac{\lambda}{2} \sum_{\substack{j=1 \\ j \neq k}}^N \sum_{\{S_i\}} S_k \left[1 - S_j \tanh \left(\beta J \sum_{L_j} S_{L_j} + \beta h \right) \right] P(\{S_i\}, t) \\ & + \frac{\lambda}{2} \sum_{\substack{j=1 \\ j \neq k}}^N \sum_{\{S_i\}} S_k \left[1 - S_j \tanh \left(\beta J \sum_{L_j} S_{L_j} + \beta h \right) \right] P(\{S_i\}, t) \\ & - \frac{\lambda}{2} \sum_{\{S_i\}} S_k \left[1 - S_k \tanh \left(\beta J \sum_{L_k} S_{L_k} + \beta h \right) \right] P(\{S_i\}, t) \\ & + \frac{\lambda}{2} \sum_{\{S_i\}} -S_k \left[1 - S_k \tanh \left(\beta J \sum_{L_k} S_{L_k} + \beta h \right) \right] P(\{S_i\}, t). \end{aligned} \quad (1.14)$$

The first two terms cancel each other and finally the resulting expression is

$$\begin{aligned} \lambda^{-1} \frac{d}{dt} \langle S_k \rangle = & - \sum_{\{S_i\}} S_k \left[1 - S_k \tanh \left(\beta J \sum_{L_k} S_{L_k} + \beta h \right) \right] P(\{S_i\}, t) \\ = & - \langle S_k \rangle + \left\langle \tanh \left(\beta J \sum_{L_k} S_{L_k} + \beta h \right) \right\rangle, \end{aligned} \quad (1.15)$$

where we have used $S_k^2 = 1$

1.2.2 Mean-Field Approximation and Time-Dependent Ginzburg-Landau Equation

No analytical solution exists for Eq. (1.15) for $d \geq 2$. The reason for this is if we expand the RHS of Eq. (1.15), it yields a coupled set of equations for higher-order correlation functions. However, we can simplify the equation using the mean-field approximation, i.e., by replacing the average of the product of spins by the product of their averages. Thus, in Eq. (1.15) the angular brackets denoting the statistical average can be taken inside the tanh-function to obtain

$$\lambda^{-1} \frac{d}{dt} \langle S_k \rangle = - \langle S_k \rangle + \tanh \left(\beta J \sum_{L_k} \langle S_{L_k} \rangle + \beta h \right). \quad (1.16)$$

Equation (1.16) is nonlinear due to the presence of the tanh-function, and it can only be handled numerically. However, further simplification can be obtained by expanding the tanh-function and retaining only leading-order terms. For simplicity, we consider $h = 0$, i.e., zero magnetic field. We can now Taylor-expand various terms on the RHS of Eq. (1.16) as follows:

$$\sum_{L_k} \langle S_{L_k} \rangle \simeq q\psi(\vec{r}_k, t) + a^2 \nabla^2 \psi(\vec{r}_k, t) + \dots \text{higher-order terms}. \quad (1.17)$$

Here, q is the coordination number of a lattice site, and a is the lattice spacing.

Furthermore,

$$\begin{aligned}
\tanh\left(\beta J \sum_{L_k} \langle S_{L_k} \rangle\right) &\simeq \beta J \sum_{L_k} \langle S_{L_k} \rangle - \frac{1}{3} \left(\beta J \sum_{L_k} \langle S_{L_k} \rangle\right)^3 \\
&\quad + \dots \text{higher-order terms} \\
&\simeq \frac{T_c}{T} \psi(\vec{r}_k, t) - \frac{1}{3} \left(\frac{T_c}{T}\right)^3 \psi(\vec{r}_k, t)^3 + \frac{T_c}{qT} a^2 \nabla_k^2 \psi(\vec{r}_k, t) \\
&\quad + \dots \text{higher-order terms.}
\end{aligned} \tag{1.18}$$

Here, we have introduced the mean-field critical temperature $T_c = qJ/k_B$. Replacing Eq. (1.18) in Eq. (1.16), we obtain

$$\begin{aligned}
\lambda^{-1} \frac{\partial}{\partial t} \psi(\vec{r}, t) &= \left(\frac{T_c}{T} - 1\right) \psi(\vec{r}, t) - \frac{1}{3} \left(\frac{T_c}{T}\right)^3 \psi(\vec{r}, t)^3 + \frac{T_c}{qT} a^2 \nabla^2 \psi(\vec{r}, t) \\
&\quad + \dots \text{other terms.}
\end{aligned} \tag{1.19}$$

Equation (1.19) is known as the time-dependent Ginzburg Landau equation or TDGL equation. The above small-amplitude expansions are only valid for $T \simeq T_c$, when the order parameter is small. However, it is generally believed that the TDGL equation is valid for any arbitrary quench to $T < T_c$.

Notice that the noise term is missing from Eq. (1.19). The noise term can be introduced in the TDGL equation if we approximate higher-order correlations as fluctuations.

1.3 Kinetic Ising Models with Conserved Dynamics

1.3.1 Spin-Exchange Kawasaki Dynamics

The Glauber model, which assumes single-spin-flip processes, successfully models nonconserved kinetics. Clearly, the Glauber model is not applicable when describing either phase separation or order-disorder transitions in binary mixtures. The appropriate microscopic dynamics should then involve random exchange of A-atoms and B-atoms at neighboring sites. The Ising Hamiltonian in Eq. (1.1) is still applicable but the spin-value $S_i = +1$ corresponds to an A-atom, and $S_i = -1$ corresponds to a B-atom. This is known as the Kawasaki spin-exchange model [15, 16] and successfully describes the conserved dynamics of binary mixtures (AB). In practice, this diffusive exchange is only possible through vacancies (which are present in a small concentration) and the system should be described as a ternary (ABV) mixture [17, 18]. However, the kinetics is simplified by assuming that the vacancy concentration is sufficiently small that it can be ignored, and the underlying stochastic process is taken to be a spin-exchange. The corresponding master equation is as follows:

$$\begin{aligned} \frac{d}{dt}P(\{S_i\}, t) = & - \sum_{j=1}^N \sum_{k \in L_j} W(S_1, \dots, S_j, S_k, \dots, S_N | S_1, \dots, S_k, S_j, \dots, S_N) P(\{S_i\}, t) \\ & + \sum_{j=1}^N \sum_{k \in L_j} W(S_1, \dots, S_k, S_j, \dots, S_N | S_1, \dots, S_j, S_k, \dots, S_N) P(\{S'_i\}, t). \end{aligned} \tag{1.20}$$

The first term on the RHS is the loss of probability for the state $\{S_i\}$ due to the spin exchange $S_j \leftrightarrow S_k$. The second term on the RHS is the gain term for the probability

of the state $\{S_i\}$ due to a spin exchange. We consider nearest-neighbor exchanges only, i.e., site $k \in L_j$, where L_j denotes the nearest neighbors of j .

We note that a binary mixture is described by an ensemble with fixed (T, M, N) , where the magnetization is defined as $M = \sum_{i=1}^N S_i = N_A - N_B$, and is conserved. (Here, N_A and N_B are the numbers of A-atoms and B-atoms, respectively.) Hence the corresponding equilibrium distribution is

$$P_{\text{eq}}(\{S_i\}) = \frac{1}{Z(T, M, N)} \exp(-\beta H) \delta_{\sum_i S_i, M}, \quad (1.21)$$

where the Kronecker delta function ensures that the probability distribution conserves the total magnetization M . The partition function $Z(T, M, N)$ is defined as

$$Z(T, M, N) = \sum_{\{S_i\}} \exp(-\beta H) \delta_{\sum_i S_i, M}. \quad (1.22)$$

Further, we choose a transition probability of the Suzuki-Kubo form [19]:

$$W(\{S_i\} | \{S'_i\}) = \frac{\lambda}{2} \left[1 - \tanh\left(\frac{\beta \delta H}{2}\right) \right], \quad (1.23)$$

where δH is the change in energy due to the spin-exchange $S_j \leftrightarrow S_k$.

For the Ising model, we have

$$\begin{aligned} H_{\text{initial}} &= -JS_j \sum_{L_j \neq k} S_{L_j} - JS_k \sum_{L_k \neq j} S_{L_k} - JS_j S_k + \text{other terms}, \\ H_{\text{final}} &= -JS_k \sum_{L_j \neq k} S_{L_j} - JS_j \sum_{L_k \neq j} S_{L_k} - JS_j S_k + \text{other terms}. \end{aligned} \quad (1.24)$$

Hence we get

$$\delta H = J (S_j - S_k) \left[\sum_{L_j \neq k} S_{L_j} - \sum_{L_k \neq j} S_{L_k} \right]. \quad (1.25)$$

Using Eq. (1.25), $W(\{S_i\}|\{S'_i\})$ can be written as

$$W(\{S_i\}|\{S'_i\}) = \frac{\lambda}{2} \left[1 - \tanh \left(\frac{\beta J}{2} (S_j - S_k) \left[\sum_{L_j \neq k} S_{L_j} - \sum_{L_k \neq j} S_{L_k} \right] \right) \right].$$

This term can be simplified by using the fact that $(S_j - S_k)/2 = 0, \pm 1$, which can be factored out of the tanh-function. Then,

$$W(\{S_i\}|\{S'_i\}) = \frac{\lambda}{2} \left[1 - \frac{(S_j - S_k)}{2} \tanh \left(\beta J \left[\sum_{L_j \neq k} S_{L_j} - \sum_{L_k \neq j} S_{L_k} \right] \right) \right]. \quad (1.26)$$

The master equation (1.20) has the form

$$\begin{aligned} \frac{d}{dt} P(\{S_i\}, t) = & - \frac{\lambda}{2} \sum_{j=1}^N \sum_{k \in L_j} \left\{ 1 - \frac{(S_j - S_k)}{2} \tanh \left(\beta J \left[\sum_{L_j \neq k} S_{L_j} - \sum_{L_k \neq j} S_{L_k} \right] \right) \right\} P(\{S_i\}, t) \\ & + \frac{\lambda}{2} \sum_{j=1}^N \sum_{k \in L_j} \left\{ 1 + \frac{(S_j - S_k)}{2} \tanh \left(\beta J \left[\sum_{L_j \neq k} S_{L_j} - \sum_{L_k \neq j} S_{L_k} \right] \right) \right\} P(\{S'_i\}, t). \end{aligned} \quad (1.27)$$

We obtain the evolution equation of the magnetization by multiplying both sides

of Eq. (1.27) with S_n and summing over all configuration states:

$$\begin{aligned} \frac{d}{dt} \langle S_n \rangle = & -\frac{\lambda}{2} \sum_{\{S_i\}} \sum_{j=1}^N \sum_{k \in L_j} S_n \left\{ 1 - \frac{(S_j - S_k)}{2} \tanh \left(\beta J \left[\sum_{L_j \neq k} S_{L_j} - \sum_{L_k \neq j} S_{L_k} \right] \right) \right\} P(\{S_i\}, t) \\ & + \frac{\lambda}{2} \sum_{\{S_i\}} \sum_{j=1}^N \sum_{k \in L_j} S_n \left\{ 1 + \frac{(S_j - S_k)}{2} \tanh \left(\beta J \left[\sum_{L_j \neq k} S_{L_j} - \sum_{L_k \neq j} S_{L_k} \right] \right) \right\} P(\{S'_i\}, t). \end{aligned} \quad (1.28)$$

The equation can then be further simplified by using the variable transformation $S_j = S_k$ and $S_k = S_j$ in the second term on the RHS. This leads to a cancellation of all terms except for $n = j$, and the only remaining terms are

$$\begin{aligned} \frac{d}{dt} \langle S_n \rangle = & -\frac{\lambda}{2} \sum_{\{S_i\}} \sum_{k \in L_n} S_n \left\{ 1 - \frac{(S_n - S_k)}{2} \tanh \left(\beta J \left[\sum_{L_n \neq k} S_{L_j} - \sum_{L_k \neq n} S_{L_k} \right] \right) \right\} P(\{S_i\}, t) \\ & + \frac{\lambda}{2} \sum_{\{S_i\}} \sum_{k \in L_n} S_k \left\{ 1 + \frac{(S_k - S_n)}{2} \tanh \left(\beta J \left[\sum_{L_n \neq k} S_{L_j} - \sum_{L_k \neq n} S_{L_k} \right] \right) \right\} P(\{S_i\}, t) \\ = & -\frac{\lambda}{2} \left\langle \sum_{k \in L_n} (S_n - S_k) \left\{ 1 - \frac{(S_n - S_k)}{2} \tanh \left(\beta J \left[\sum_{L_n \neq k} S_{L_n} - \sum_{L_k \neq n} S_{L_k} \right] \right) \right\} \right\rangle. \end{aligned} \quad (1.29)$$

After some calculation [20], we finally get

$$\begin{aligned} 2\lambda^{-1} \frac{d}{dt} \langle S_n \rangle = & -q \langle S_n \rangle + \sum_{L_n} \langle S_{L_n} \rangle \\ & + \sum_{k \in L_n} \left\langle (1 - S_n S_k) \tanh \left[\beta J \left(\sum_{L_n \neq k} S_{L_n} - \sum_{L_k \neq n} S_{L_k} \right) \right] \right\rangle. \end{aligned} \quad (1.30)$$

Equation (1.30) has no analytical solutions for $d \geq 2$, like its counterpart for Glauber kinetics, Eq. (1.15). In the next subsection, we will invoke the mean-field approxi-

mation to simplify the above equation.

1.3.2 Mean-Field Approximation and Cahn-Hilliard Equation

As in the Glauber case, Eq. (1.30) can be truncated by using the mean-field approximation, i.e., by replacing expectation values of a function of spin variables by the function of the expectation values of the spin variables. The simplified equation can be written as follows:

$$2\lambda^{-1} \frac{d}{dt} \langle S_n \rangle = -q \langle S_n \rangle + \sum_{L_n} \langle S_{L_n} \rangle + \sum_{k \in L_n} (1 - \langle S_n \rangle \langle S_k \rangle) \tanh \left[\beta J \left(\sum_{L_n} \langle S_{L_n} \rangle - \sum_{L_k} \langle S_{L_k} \rangle \right) \right]. \quad (1.31)$$

Here we note that the restriction on the summation inside the tanh-function in Eq. (1.30) is removed. Also the correct MF solution in this case is

$$\langle S_k \rangle_{\text{eq}} = \tanh \left(\beta J \sum_{L_k} \langle S_{L_k} \rangle_{\text{eq}} \right). \quad (1.32)$$

This can be verified by inserting Eq. (1.32) in the RHS of Eq. (1.31) [7].

We can further simplify Eq. (1.31) by using the identity,

$$\tanh(x - y) = \frac{\tanh x - \tanh y}{1 - \tanh x \tanh y},$$

where $x = \beta J \sum_{L_n} \langle S_{L_n} \rangle$ and $y = \beta J \sum_{L_k} \langle S_{L_k} \rangle$. Then the third term on the RHS of

Eq. (1.31) can be simplified as

$$(1 - \langle S_n \rangle \langle S_k \rangle) \left(\frac{\tanh x - \tanh y}{1 - \tanh x \tanh y} \right) \simeq (\tanh x - \tanh y). \quad (1.33)$$

Hence, we can write Eq. (1.31) as

$$\begin{aligned} 2\lambda^{-1} \frac{d}{dt} \langle S_n \rangle &\simeq \sum_{L_n} (\langle S_{L_n} \rangle - \langle S_n \rangle) \\ &+ \sum_{k \in L_n} \left[\tanh \left(\beta J \sum_{L_n} \langle S_{L_n} \rangle \right) - \tanh \left(\beta J \sum_{L_k} \langle S_{L_k} \rangle \right) \right] \\ &= \Delta_D \left[\langle S_n \rangle - \tanh \left(\beta J \sum_{L_n} \langle S_{L_n} \rangle \right) \right], \end{aligned} \quad (1.34)$$

where Δ_D is the discrete Laplacian operator. Following Eq. (1.19), we can Taylor-expand Eq. (1.34) to obtain an order-parameter evolution equation as follows:

$$\begin{aligned} 2\lambda^{-1} \frac{\partial}{\partial t} \psi(\vec{r}, t) &= -a^2 \nabla^2 \left[\left(\frac{T_c}{T} - 1 \right) \psi(\vec{r}, t) - \frac{1}{3} \left(\frac{T_c}{T} \right)^3 \psi(\vec{r}, t)^3 \right. \\ &\quad \left. + \frac{T_c}{qT} a^2 \nabla^2 \psi(\vec{r}, t) \right] + \text{other terms}, \end{aligned} \quad (1.35)$$

where a is the lattice spacing.

Equation (1.35) is known as the Cahn-Hilliard (CH) equation and is the standard model for phase separation in binary mixtures [21].

1.4 Domain Growth in Systems with Non-conserved Kinetics

1.4.1 Ginzburg-Landau Free Energy

Let us now discuss the phenomenological modeling of phase ordering systems. Recall that there are two paradigmatic problems in this context: (a) ordering of a ferromagnet or the *case with nonconserved order parameter*, and (b) segregation of a binary mixture or the *case with conserved order parameter*. First, we discuss the nonconserved case.

Magnetism is a quantum-mechanical phenomenon involving electrons and their spins. The microscopic description of interacting electrons is very complicated and material-dependent. Moreover it is also not a very useful way to describe paramagnetic \rightarrow ferromagnetic transitions. The degrees of freedom which describe the transition are long-wavelength collective excitations of spins. Therefore, we can coarse-grain the magnet to a scale larger than the lattice spacing, and define a magnetization vector field $\vec{\psi}(\vec{r})$, which represents the average of spins in the vicinity of \vec{r} . The magnetization is the proper order parameter in such situations, and the thermodynamic state can be achieved by minimizing the relevant free energy of the system as a function of $\vec{\psi}$. For simplicity, we discuss the case with scalar order parameter $\psi(\vec{r})$, as in the Ising model.

A general free energy or Ginzburg-Landau free energy can be written following some basic symmetries, such as [1]

- Locality of the magnetization: The free energy should depend on the local mag-

netization and short-range interactions expressed through a gradient expansion:

$$\beta G[\psi] = \int d\vec{x} f(\psi(\vec{x}), \nabla\psi, \dots). \quad (1.36)$$

- Rotational symmetry: In the absence of a magnetic field, the system should be isotropic in space and therefore invariant under the reflection, $\psi = -\psi$.
- The above considerations yield the Taylor-expanded free energy of the system as follows:

$$\beta G[\psi] = \int d\vec{x} \left[\frac{t}{2} \psi^2 + \frac{u}{4} \psi^4 + \frac{K}{2} (\nabla\psi)^2 + \frac{L}{2} (\nabla^2\psi)^2 + \dots - h\psi \right]. \quad (1.37)$$

Equation (1.37) is known as the Ginzburg-Landau free energy and it depends on the phenomenological parameters t, u, K , etc. These are functions of microscopic interactions, as well as external parameters such as the temperature, e.g., $t \simeq a(T - T_c)$, $u > 0$, $K > 0$, etc. Thermodynamic quantities can now be obtained by minimizing the Landau free-energy density [1, 22, 23]:

TH-16967

$$g(\psi, h) = \frac{t}{2} \psi^2 + \frac{u}{4} \psi^4 - h\psi. \quad (1.38)$$

Near the critical point, ψ is small and it is justified to keep only lower powers in the expansion of $g(\psi, h)$.

The behavior of $g(\psi, h)$ depends sensitively on the sign of t – see Fig. 1.5. The Ginzburg-Landau free energy implies paramagnetic behavior for $t > 0$ and ferromagnetic behavior for $t < 0$. We can identify the parameter t with a reduced temperature, $t = a(T - T_c)/T_c$. With this identification, we can now introduce the TDGL equation [cf. Eq. (1.19)] as the dissipative (overdamped) relaxation of the ferromagnetic

530.13
M8967

CI

TH

21



TH16967



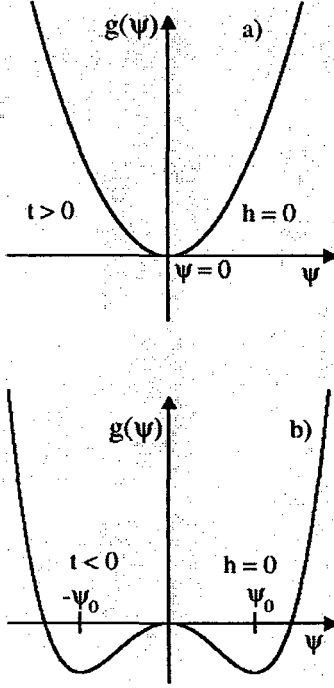


Figure 1.5: The sketch shows the Landau free-energy density $g(\psi)$ as a function of the order parameter ψ . The sensitivity on the sign of t is also illustrated. (a) For $t > 0$, the global minima is located at $\psi = 0$, reflecting the paramagnetic phase. (b) For $t < 0$ there exist degenerate global minima at $\psi_0 = \pm\sqrt{-t/u}$, which corresponds to a ferromagnetic phase.

system to its free-energy minimum:

$$\frac{\partial}{\partial t} \psi(\vec{r}, t) = -\Gamma \frac{\delta G[\psi]}{\delta \psi} + \theta(\vec{r}, t). \quad (1.39)$$

Here, Γ is the inverse damping coefficient, and $\delta G[\psi]/\delta \psi$ is the functional derivative of the free-energy functional. The Gaussian white noise term is also space and time dependent and satisfies the fluctuation-dissipation relation:

$$\overline{\theta(\vec{r}, t)} = 0, \quad (1.40)$$

$$\overline{\theta(\vec{r}, t) \theta(\vec{r}', t')} = 2\Gamma k_B T \delta(\vec{r} - \vec{r}') \delta(t - t'), \quad (1.41)$$

where the bars denote an average over the Gaussian noise ensemble.

For the ψ^4 -free energy in Eq. (1.37), the TDGL equation has the form

$$\frac{\partial}{\partial t} \psi(\vec{r}, t) = \Gamma [a(T_c - T) \psi - u\psi^3 + h + K\nabla^2 \psi] + \theta(\vec{r}, t). \quad (1.42)$$

This equation can be further recast into a dimensionless form by introducing rescaled variables (considering the case with $T < T_c$):

$$\begin{aligned} \psi' &= \frac{\psi}{\psi_0}, & \psi_0 &= \sqrt{\frac{a(T_c - T)}{u}}, \\ t' &= a(T_c - T) \Gamma t, \\ \vec{r}' &= \sqrt{\frac{a(T_c - T)}{K}} \vec{r}, & \xi &= \sqrt{\frac{2K}{a(T_c - T)}}, \\ h' &= \frac{h}{a(T_c - T) \psi_0}, \\ \theta' &= \frac{\theta}{a(T_c - T) \psi_0}. \end{aligned} \quad (1.43)$$

Using these rescaled variables, the TDGL equation becomes

$$\frac{\partial}{\partial t} \psi(\vec{r}, t) = \psi - \psi^3 + h + \nabla^2 \psi + \theta(\vec{r}, t), \quad (1.44)$$

where we have dropped the primes. In these dimensionless variables, the noise correlations are as follows:

$$\begin{aligned} \overline{\theta(\vec{r}, t)} &= 0, \\ \overline{\theta(\vec{r}, t) \theta(\vec{r}', t')} &= 2\epsilon \delta(\vec{r} - \vec{r}') \delta(t - t'), \\ \epsilon &= \frac{k_B T u [a(T_c - T)]^{(d-4)/2}}{K^{d/2}}. \end{aligned} \quad (1.45)$$

For $h = 0$, the system prefers to be in a ferromagnetic state with spins up or down. Domains enriched in up and down spins emerge, and the length scale of the domains $L(t)$ grows with time. In the following subsection, we will study in detail the evolution dynamics of the TDGL equation based on motion of interfaces.

1.4.2 Interface Motion

We consider the deterministic TDGL equation [i.e., Eq. (1.44) without noise] and set $h = 0$:

$$\frac{\partial}{\partial t}\psi(\vec{r}, t) = \psi - \psi^3 + \nabla^2\psi. \quad (1.46)$$

The equilibrium solution of Eq. (1.46) corresponds to either $\psi = 1$ or $\psi = -1$. There can also be a kink or interface which is obtained as the solution of

$$\psi - \psi^3 + \frac{d^2\psi}{dz^2} = 0. \quad (1.47)$$

The kink solution of Eq. (1.47) is

$$\psi_s(z) = \tanh\left[\pm\frac{(z - z_0)}{\sqrt{2}}\right], \quad (1.48)$$

where z_0 is the center of the kink. The solutions with positive and negative signs are called *kinks* and *anti-kinks*, respectively. The kink solution has $\psi \rightarrow -1$ as $z \rightarrow -\infty$ and $\psi \rightarrow 1$ as $z \rightarrow \infty$. However, in the interface region it differs from ± 1 , and its width is given by the correlation length ($\xi = \sqrt{2}$).

The dynamics of interfacial motion can be understood by the Allen-Cahn equation of motion [24]. We first express the TDGL equation in terms of interfacial coordinates (n, \vec{a}) . We have

$$\vec{\nabla}\psi = \frac{\partial\psi}{\partial n}\Big|_t \hat{n}, \quad (1.49)$$

where \hat{n} is the unit vector normal to the interface in the direction of increasing ψ .

Also,

$$\nabla^2\psi = \frac{\partial^2\psi}{\partial n^2}\Big|_t \hat{n} \cdot \hat{n} + \frac{\partial\psi}{\partial n}\Big|_t \vec{\nabla} \cdot \hat{n}. \quad (1.50)$$

Now the TDGL equation can be written in interfacial coordinates (n, \vec{a}) :

$$-\frac{\partial\psi}{\partial n}\Big|_t \frac{\partial n}{\partial t}\Big|_\psi = \psi - \psi^3 + \frac{\partial^2\psi}{\partial n^2}\Big|_t + \frac{\partial\psi}{\partial n}\Big|_t \vec{\nabla} \cdot \hat{n}. \quad (1.51)$$

This can be further simplified if the interfaces are already settled to a steady state:

$$\frac{\partial\psi}{\partial n}\Big|_t = \vec{\nabla} \cdot \hat{n}. \quad (1.52)$$

We recognize that $\partial n/\partial t\Big|_\psi = v(\vec{a})$, where v is the normal interfacial velocity in direction \hat{n} . This yields the Allen-Cahn equation:

$$v(\vec{a}) = -\vec{\nabla} \cdot \hat{n} = -K(\vec{a}), \quad (1.53)$$

where K is the local curvature of the interface. Next we note that $K \sim 1/L$ and $v \sim dL/dt$. Thus, combining these two, we get the diffusive growth law: $L(t) \sim t^{1/2}$.

1.4.3 Correlation Functions and Structure Factors

The study of evolving morphologies of phase ordering systems involves calculation of the equal-time correlation function $C(\vec{r}, t)$, and the structure factor $S(\vec{k}, t)$, which is the Fourier transform of the correlation function.

The correlation function is defined as

$$C(\vec{r}, t) = \frac{1}{V} \int d\vec{R} \left[\langle \psi(\vec{R}, t) \psi(\vec{R} + \vec{r}, t) \rangle - \langle \psi(\vec{R}, t) \rangle \langle \psi(\vec{R} + \vec{r}, t) \rangle \right], \quad (1.54)$$

where V is the volume, and $\langle \dots \rangle$ denotes an ensemble averaging over initial conditions and thermal fluctuations.

The structure factor $S(\vec{k}, t)$ is of great experimental importance as scattering experiments with probes of the appropriate wavelength, e.g., light, X-rays, etc., can measure this quantity directly. The corresponding definition of the structure factor is

$$S(\vec{k}, t) = \int d\vec{r} e^{i\vec{k}\cdot\vec{r}} C(\vec{r}, t). \quad (1.55)$$

The snapshots of the evolution dynamics at different times [see Figures. 1.2 and 1.4] suggest that the domain morphology is statistically self-similar in time, except for a scale factor. Therefore, the correlation function and structure factor exhibit a dynamical-scaling property [25]:

$$C(r, t) \equiv f\left(\frac{r}{L(t)}\right), \quad \text{and} \quad (1.56)$$

$$S(k, t) \equiv L(t)^d g(kL(t)). \quad (1.57)$$

The scaling functions $f(x)$ and $g(p)$ characterize the morphology of the ordering system.

1.4.4 Growth Exponents

In many phase ordering systems, the asymptotic domain length scale exhibits a power law behavior $L(t) \sim t^\theta$, where θ is referred to as the growth exponent. The value of this exponent depends on the nature of the order parameter, conservation laws, relevance of hydrodynamic effects, presence of quenched or annealed impurities in the system, etc. For example, in the case of the ordering ferromagnet, the scalar order

parameter is not conserved and we get $\theta = 1/2$. This growth law is referred to as the Allen-Cahn law [24]. On the other hand, for phase-separating binary mixtures, which are described by a scalar conserved order parameter, the growth exponent is $\theta = 1/3$ (in the absence of any hydrodynamic effects). This growth law is referred to in the literature as the Lifshitz-Slyozov (LS) law [26].

The characteristic length scale can be defined in a variety of ways, all of which are analogous. For example, it can be defined from the structure factor as $L(t) \sim \langle k \rangle^{-1}$, where $\langle k \rangle$ is the first moment of the spherically-averaged structure factor, i.e.,

$$\langle k \rangle = \frac{\int_0^{k_m} dk k S(k, t)}{\int_0^{k_m} dk S(k, t)}. \quad (1.58)$$

The zero-crossing of the correlation function, or some characteristic decay length, can also be a measure of calculating the length scale. This quantity can also be measured from higher moments of $S(k, t)$. However, all these definitions are equivalent in the dynamical-scaling regime.

1.4.5 Ohta-Jasnow-Kawasaki Theory

In this subsection, we will extend Allen-Cahn's equation of interface motion by incorporating multiple defects or interfaces. In this context, an approximate theory has been developed by Ohta et al. (OJK) [27].

In the late stages, domain growth is dominated by motion of domain boundaries. The order parameter rapidly changes sign at domain boundaries. OJK had introduced a nonlinear transformation $\psi = \psi(m)$, where $m(\vec{r}, t)$ is a smoothly varying function through the interface. A natural choice for this auxiliary field $m(\vec{r}, t)$ is the normal distance from the interface, such that $m(\vec{r}, t) = 0$ at the interface. Let us now develop

the equation of motion for $m(\vec{r}, t)$.

The Allen-Cahn equation of interface motion is $v(\vec{a}) = -\vec{\nabla} \cdot \hat{n}$, where \hat{n} is the unit vector normal to the interface. We have the definition

$$\hat{n} = \frac{\vec{\nabla} m}{|\vec{\nabla} m|}. \quad (1.59)$$

Therefore,

$$v = -\vec{\nabla} \cdot \hat{n} = -\frac{\nabla^2 m}{|\vec{\nabla} m|} + \frac{n_i n_j \nabla_i \nabla_j m}{|\vec{\nabla} m|}, \quad (1.60)$$

where repeated indices are summed over. Further,

$$\frac{dm}{dt} = \frac{\partial m}{\partial t} + \vec{\nabla} m \cdot \vec{v} = 0. \quad (1.61)$$

Hence we get,

$$v = -\frac{1}{|\vec{\nabla} m|} \frac{\partial m}{\partial t}. \quad (1.62)$$

Comparing Eq. (1.60) and Eq. (1.62), we obtain a dynamical equation for m :

$$\frac{\partial}{\partial t} m(\vec{r}, t) = \nabla^2 m - n_i n_j \nabla_i \nabla_j m. \quad (1.63)$$

An analytical solution of Eq. (1.63) is not possible, hence OJK replaced the term $n_i n_j$ by its spherical average:

$$n_i n_j \simeq \frac{\delta_{ij}}{d}. \quad (1.64)$$

Under this approximation, the equation for the field m becomes

$$\frac{\partial}{\partial t} m(\vec{r}, t) = \left(\frac{d-1}{d} \right) \nabla^2 m. \quad (1.65)$$

The above equation is merely the linear diffusion equation.

Next we calculate the correlation function of the ψ -field. The initial condition for the m -field is taken to be Gaussian-distributed with δ -function correlation:

$$\langle m(\vec{r}, 0) m(\vec{r}', 0) \rangle = A \delta(\vec{r} - \vec{r}'). \quad (1.66)$$

The appropriate distribution of m is Gaussian, hence

$$P[m(\vec{r}, 0)] = \frac{1}{\sqrt{2\pi\sigma(0)^2}} \exp\left[-\frac{m(\vec{r}, 0)^2}{2\sigma(0)^2}\right], \quad \sigma(0)^2 = \langle m(\vec{r}, 0)^2 \rangle. \quad (1.67)$$

The diffusion dynamics preserves the Gaussian nature of the system, hence

$$P[m(\vec{r}, t)] = \frac{1}{\sqrt{2\pi\sigma(t)^2}} \exp\left[-\frac{m(\vec{r}, t)^2}{2\sigma(t)^2}\right], \quad \sigma(t)^2 = \langle m(\vec{r}, t)^2 \rangle. \quad (1.68)$$

We now calculate the general space-time correlation function:

$$\begin{aligned} C(\vec{r}_1, t_1; \vec{r}_2, t_2) &= \langle \psi(\vec{r}_1, t_1) \psi(\vec{r}_2, t_2) \rangle \\ &= \langle \text{sgn}[m(\vec{r}_1, t_1)] \text{sgn}[m(\vec{r}_2, t_2)] \rangle. \end{aligned} \quad (1.69)$$

To obtain this quantity, we need the normalized bivariate Gaussian distribution for $m(\vec{r}_1, t_1)$ [28]:

$$P(x, y) = \frac{1}{2\pi\sigma(t_1)\sigma(t_2)\sqrt{1-\gamma^2}} \exp\left[-\frac{1}{2(1-\gamma^2)} \left(\frac{x^2}{\sigma(t_1)^2} + \frac{y^2}{\sigma(t_2)^2} - \frac{2\gamma xy}{\sigma(t_1)\sigma(t_2)} \right)\right], \quad (1.70)$$

where

$$\begin{aligned} \sigma(t_1)^2 &= \langle x^2 \rangle = \langle m(\vec{r}_1, t_1)^2 \rangle, \\ \sigma(t_2)^2 &= \langle y^2 \rangle = \langle m(\vec{r}_2, t_2)^2 \rangle, \end{aligned}$$

$$\gamma = \frac{\langle xy \rangle}{\sqrt{\langle x^2 \rangle \langle y^2 \rangle}} = \frac{\langle m(\vec{r}_1, t_1) m(\vec{r}_2, t_2) \rangle}{\sqrt{\langle m(\vec{r}_1, t_1) \rangle \langle m(\vec{r}_2, t_2) \rangle}}. \quad (1.71)$$

Hence the correlation function becomes

$$C(\vec{r}_1, t_1; \vec{r}_2, t_2) = \frac{1}{2\pi\sigma(t_1)\sigma(t_2)\sqrt{1-\gamma^2}} \int_{-\infty}^{+\infty} dx \int_{-\infty}^{+\infty} dy \frac{x}{\sqrt{x^2}} \frac{y}{\sqrt{y^2}} \times \exp \left[-\frac{1}{2(1-\gamma^2)} \left(\frac{x^2}{\sigma(t_1)^2} + \frac{y^2}{\sigma(t_2)^2} - \frac{2\gamma xy}{\sigma(t_1)\sigma(t_2)} \right) \right], \quad (1.72)$$

where we have used $\text{sgn}(z) = z/\sqrt{z^2}$. We rescale variables as $x' = x/\sigma(t_1)$ and $y' = y/\sigma(t_2)$ and drop the primes. Hence we get

$$C(\vec{r}_1, t_1; \vec{r}_2, t_2) = \frac{1}{2\pi\sqrt{1-\gamma^2}} \int_{-\infty}^{+\infty} dx \int_{-\infty}^{+\infty} dy \frac{x}{\sqrt{x^2}} \frac{y}{\sqrt{y^2}} \exp(-\alpha x^2 - \beta y^2 + \beta xy), \quad (1.73)$$

where

$$\alpha = \frac{1}{2(1-\gamma^2)}, \quad \beta = \frac{\gamma}{(1-\gamma^2)}. \quad (1.74)$$

After some further algebra, the final result obtained is [7]

$$C(\vec{r}_1, t_1; \vec{r}_2, t_2) = \frac{2}{\pi} \sin^{-1}(\gamma), \quad (1.75)$$

where γ is defined in Eq. (1.71).

Finally, we will obtain the quantity γ , which will complete our description of OJK theory. According to Eq. (1.65), we can write

$$m(\vec{r}, t) = e^{Dt\nabla^2} m(\vec{r}, 0), \quad D = \frac{d-1}{d}. \quad (1.76)$$

In momentum space, Eq. (1.76) can be written as

$$m(\vec{k}, t) = e^{-Dt k^2} m(\vec{k}, 0). \quad (1.77)$$

Therefore, the general correlation function of the m -field can be written as

$$\begin{aligned} \langle m(\vec{r}_1, t_1) m(\vec{r}_2, t_2) \rangle &= \int \frac{d\vec{k}_1}{(2\pi)^d} e^{-i\vec{k}_1 \cdot \vec{r}_1} \int \frac{d\vec{k}_2}{(2\pi)^d} e^{-i\vec{k}_2 \cdot \vec{r}_2} \langle m(\vec{k}_1, t_1) m(\vec{k}_2, t_2) \rangle \\ &= A \int \frac{d\vec{k}_1}{(2\pi)^d} e^{-i\vec{k}_1 \cdot (\vec{r}_1 - \vec{r}_2)} e^{-D(t_1 + t_2) k_1^2} \\ &= \frac{A}{[4\pi D(t_1 + t_2)]^{d/2}} \exp\left[-\frac{r^2}{4D(t_1 + t_2)}\right]. \end{aligned} \quad (1.78)$$

The correlation in momentum space can be calculated as

$$\begin{aligned} \langle m(\vec{k}_1, t_1) m(\vec{k}_2, t_2) \rangle &= e^{-Dt_1 k_1^2} e^{-Dt_2 k_2^2} \langle m(\vec{k}_1, 0) m(\vec{k}_2, 0) \rangle \\ &= A\delta(\vec{k}_1 + \vec{k}_2) e^{-D(t_1 k_1^2 + t_2 k_2^2)}, \end{aligned} \quad (1.79)$$

where

$$\langle m(\vec{k}_1, 0) m(\vec{k}_2, 0) \rangle = A\delta(\vec{k}_1 + \vec{k}_2). \quad (1.80)$$

This reflects the uncorrelated initial spin configuration of the dynamical system. Finally, we can write

$$\begin{aligned} \gamma &= \frac{\langle m(\vec{r}_1, t_1) m(\vec{r}_2, t_2) \rangle}{\sqrt{\langle m(\vec{r}_1, t_1) \rangle \langle m(\vec{r}_2, t_2) \rangle}} \\ &= \left(\frac{2\sqrt{t_1 t_2}}{t_1 + t_2}\right)^{d/2} \exp\left[-\frac{r^2}{4D(t_1 + t_2)}\right]. \end{aligned} \quad (1.81)$$

Equations (1.75) and (1.81) constitute the OJK result for the correlation function.

We first consider the equal-time correlation function, i.e.,

$$C(\vec{r}, t) = \frac{2}{\pi} \sin^{-1} \left[\exp \left(-\frac{r^2}{8Dt} \right) \right]. \quad (1.82)$$

It is clear that the OJK result has a scaling form as in Eq. (1.82) and consequently the length scale $L(t) \sim (8Dt)^{1/2}$. This result has also been obtained earlier from the Allen-Cahn equation. Further, the OJK result has been found to agree with many experimental and simulation results. A scaling plot for correlation functions at different times is shown in Fig. 1.6(a). The OJK function has also been plotted in

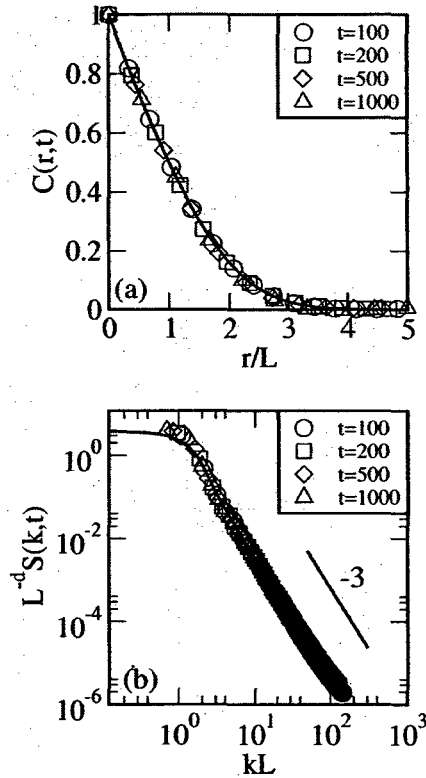


Figure 1.6: (a) Scaled correlation functions for an ordering ferromagnet at different times 100, 200, 500, 1000 is shown. The solid line is the OJK function, scaled in the same manner as the data. (b) Log-log plot of scaled structure factor at different times. The solid line is the Fourier transform of the OJK function. The tail with slope -3 is consistent with Porod's law, $S(k, t) \sim k^{-(d+1)}$ for $d = 2$.

the same graph, and is seen to be in excellent argument with the numerical data. The numerical results have been obtained from a simulation of the dimensionless TDGL equation in $d = 2$, without thermal noise. The Euler-discretization mesh sizes were $\Delta t = 0.1$ and $\Delta x = 1.0$. The lattice size was 2048^2 , and periodic boundary conditions were applied in both directions.

In Fig. 1.6(b), we plot the scaled structure factors at different times, together with the Fourier transform of the OJK function. Again, the OJK function is in good agreement with the numerical data. In Fig. 1.7, we plot the characteristic length scale (calculated from the correlation function) as a function of time. The growth is power-law with $L(t) \sim t^{1/2}$, consistent with the Allen-Cahn growth law.

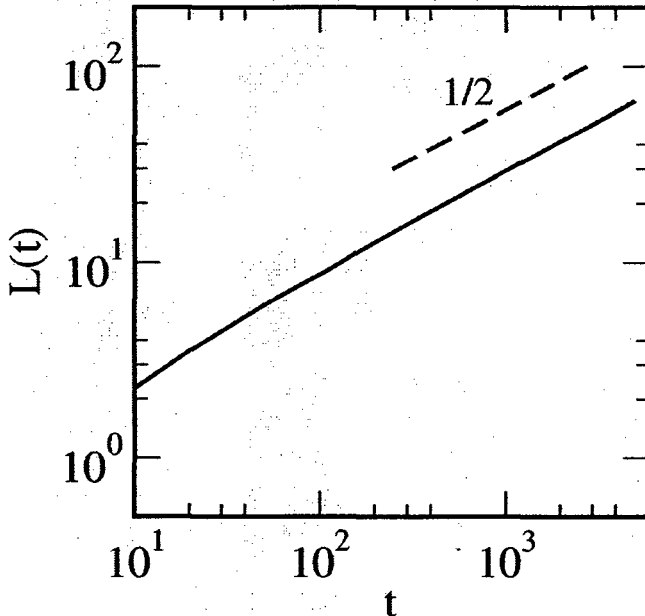


Figure 1.7: Domain growth for an ordering ferromagnet. The length scale $L(t)$ is defined as the distance over which the correlation function [cf. Fig.1.6] decays to half its maximum value. The data for $L(t)$ vs. t is plotted on a log – log scale. The dashed line denotes the Allen-Cahn growth law, $L(t) \sim t^{1/2}$.

1.5 Domain Growth in Systems with Conserved Kinetics

It has already been stressed in Sec. 1.1.2 that the evolution dynamics of a binary mixture obeys conserved kinetics, i.e., numbers of the two species of particles remain constant over time. If we neglect the effects of hydrodynamics, phase separation is driven by evaporation and condensation. The appropriate order parameter in this case is $\psi(\vec{r}, t) = n^A(\vec{r}, t) - n^B(\vec{r}, t)$, where n^α is the local density of species α . The evolution dynamics is described by the continuity equation:

$$\frac{\partial}{\partial t} \psi(\vec{r}, t) = -\vec{\nabla} \cdot \vec{J}(\vec{r}, t), \quad (1.83)$$

where $\vec{J}(\vec{r}, t)$ is the current, which is obtained as

$$\vec{J}(\vec{r}, t) = -D\vec{\nabla}\mu(\vec{r}, t). \quad (1.84)$$

Here, D is the diffusion coefficient and $\mu(\vec{r}, t)$ is the chemical potential. Finally, $\mu(\vec{r}, t)$ is determined as the functional derivative of the free energy of the system:

$$\mu(\vec{r}, t) = \frac{\delta F[\psi]}{\delta \psi}. \quad (1.85)$$

For binary mixtures F refers to the Helmholtz potential. Combining Eqs. (1.83) - (1.85), we obtain the CH equation:

$$\frac{\partial}{\partial t} \psi(\vec{r}, t) = D\nabla^2 \left(\frac{\delta F[\psi]}{\delta \psi} \right). \quad (1.86)$$

In Sec. 1.3.2, we have derived Eq. (1.35) from the Kawasaki-Ising model. Here,

this equation has been introduced on phenomenological grounds. The necessary conserved noise term can be introduced as

$$\frac{\partial}{\partial t}\psi(\vec{r}, t) = \vec{\nabla} \cdot \left\{ D\nabla \left(\frac{\delta F[\psi]}{\delta \psi} \right) + \vec{\theta}(\vec{r}, t) \right\}. \quad (1.87)$$

The Gaussian noise term satisfies the fluctuation-dissipation relation:

$$\overline{\theta_i(\vec{r}, t)} = 0, \quad (1.88)$$

$$\overline{\theta_i(\vec{r}, t) \theta_j(\vec{r}', t')} = 2Dk_B T \delta_{ij} \delta(\vec{r} - \vec{r}') \delta(t - t'). \quad (1.89)$$

This equation is also known as *Model B* in the literature [29].

For the ψ^4 -potential, the explicit form of the CH equation is

$$\frac{\partial}{\partial t}\psi(\vec{r}, t) = \vec{\nabla} \cdot \left\{ D\vec{\nabla} [-a(T_c - T)\psi + b\psi^3 - K\nabla^2\psi] + \vec{\theta}(\vec{r}, t) \right\}. \quad (1.90)$$

As in the case of the TDGL equation in Sec. 1.4.1, the CH equation can be reduced to a dimensionless form:

$$\frac{\partial}{\partial t}\psi(\vec{r}, t) = \vec{\nabla} \cdot \left[\vec{\nabla} (-\psi + \psi^3 - \nabla^2\psi) + \vec{\theta}(\vec{r}, t) \right]. \quad (1.91)$$

In this case, the rescaled variables are

$$\begin{aligned}
\psi' &= \frac{\psi}{\psi_0}, & \psi_0 &= \sqrt{\frac{a(T_c - T)}{b}}, \\
t' &= \frac{Da^2 (T_c - T)^2}{K} t, \\
\vec{r}' &= \sqrt{\frac{a(T_c - T)}{K}} \vec{r}, & \xi &= \sqrt{\frac{2K}{a(T_c - T)}}, \\
\theta' &= \frac{\sqrt{bK}}{Da^2 (T_c - T)^2} \vec{\theta}.
\end{aligned} \tag{1.92}$$

The rescaled noise obeys the fluctuation-dissipation relation:

$$\begin{aligned}
\overline{\theta_i(\vec{r}, t)} &= 0, \\
\overline{\theta_i(\vec{r}, t) \theta_j(\vec{r}', t')} &= 2\epsilon \delta_{ij} \delta(\vec{r} - \vec{r}') \delta(t - t'), \\
\epsilon &= \frac{k_B T b (a(T_c - T))^{(d-4)/2}}{K^{d/2}}.
\end{aligned} \tag{1.93}$$

The evolution of the CH equation (1.91) from a disordered initial condition is analogous to that in Fig. 1.4 (from the Kawasaki-Ising model). The snapshots in Fig. 1.4 clearly demonstrate self-similar pattern formation at late times. The system is characterized by a unique length scale, $L(t) \sim t^{1/3}$ in $d \geq 2$ (see Fig. 1.8).

The growth exponent $\theta = 1/3$ can be understood in a qualitative way as follows. The domains in the system coalesce and grow, thus minimizing the domain walls or surface area which costs energy. The energy cost of having a domain wall is characterized by surface tension σ . The surface energy of a d -dimensional system thus typically scales as σL^{d-1} , whereas volume scales as L^d . Thus the energy density $u \sim \sigma/L$, and the cost of domain walls per unit volume decreases as L increases. Accordingly, the gradient of the energy density scales as $du/dt \sim \sigma/L^2$. If we assume

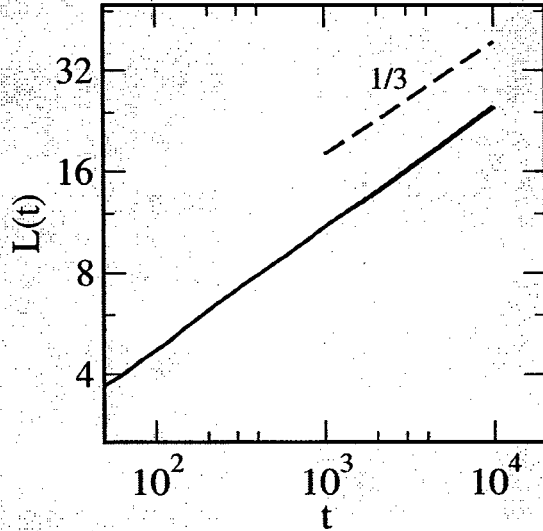


Figure 1.8: Time dependence of length-scale, $L(t)$ vs. t , in a log-log plot. The length scale $L(t)$ is defined as the distance over which the correlation function [cf. Fig. 1.9] decays to half its maximum value. The simulation details are provided in the caption of Fig. 1.9. The dashed line denotes the Lifshitz-Slyozov law of domain growth in binary mixture.

that the movement of domain walls in the asymptotic state is only diffusive, then their velocity is proportional to the energy gradient:

$$\frac{dL}{dt} = C \frac{\sigma}{L^2}, \quad (1.94)$$

where C is some constant. The solution of Eq. (1.94) yields $L \sim t^{1/3}$. In Fig. 1.8, we have plotted the length scale of domain growth in a log-log plot. The existence of a characteristic length scale confirms that the system exhibits dynamical scaling.

In Fig. 1.9, we show numerical results for the scaled correlation functions [see Fig. 1.9(a)] and structure factors [see Fig. 1.9(b)] in the segregating binary mixture. The presence of interfacial defects results in a Porod tail for the scaled structure factor, $S(k, t) \sim k^{-(d+1)}$ as $k \rightarrow \infty$.

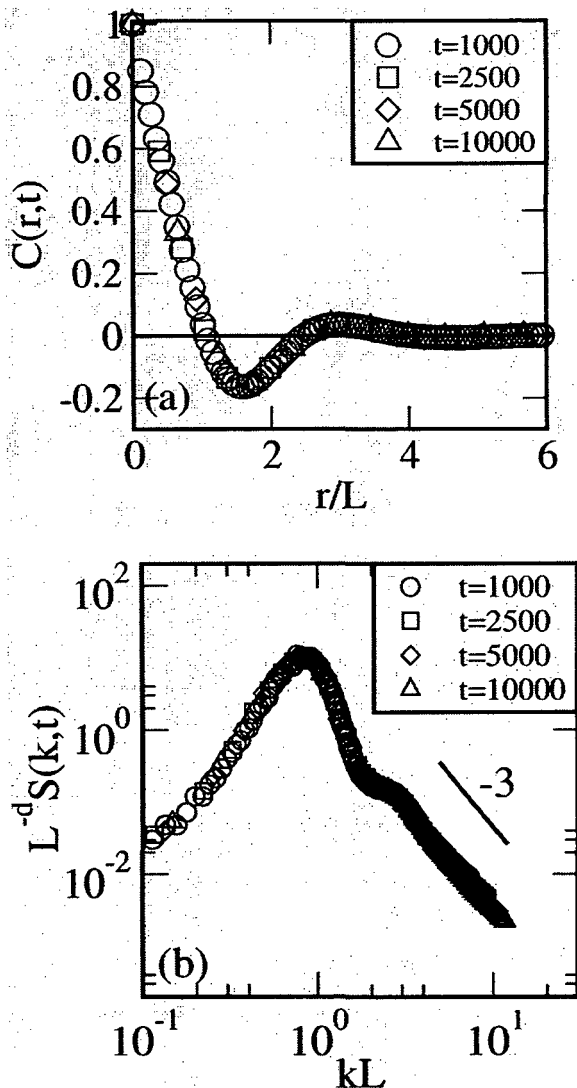


Figure 1.9: (a) Scaled correlation function [$C(r,t)$ vs. r/L] for the evolution of the phase-separating binary mixture. The simulation has been carried using the dimensionless CH equation without thermal noise. The Euler-discretization mesh sizes were $\Delta t = 0.02$ and $\Delta x = 1.0$. The lattice size was 1024^2 , and periodic boundary conditions were applied in both directions. The data was obtained at different times 1000, 2500, 5000, 10000. (b) Scaled structure factor [$L^{-d}S(k,t)$ vs. kL] from the numerical data in (a). The solid line denotes the Porod's tail with slope -3 , $S(k,t) \sim k^{-(d+1)}$ as $k \rightarrow \infty$.

In this case, the conservation constraint on the dynamics imposes an additional condition on the correlation function [7]:

$$\int d\vec{r} C(\vec{r}, t) = 0, \quad \text{or} \quad S(0, t) = 0. \quad (1.95)$$

Because of Eq. (1.95), the correlation function for a phase-separating mixture shows an oscillatory behavior. Furthermore, the conservation law also fixes the $p \rightarrow 0$ behavior of the scaled structure factor as $f(p) \sim p^4$ [30, 31].

1.6 Overview of Chapters 2-4: Our Studies of Kinetics of Phase Transitions

A brief overview of our studies of the kinetics of phase transitions in Chapters 2-4 of this thesis is given in this section. In Chapter 2, we discuss the kinetics of phase separation using the conserved-order-parameter (COP) Ising model with Kawasaki spin-exchange dynamics. Our goal is to generate an arbitrary predefined structure factor by the time-variation of external parameters, e.g., temperature. This is a form of self-organized structure formation. We focus on a specific case where we cycle the temperature above and below T_c to create a structure factor that shows multiple peaks, instead of the usual single peak.

In Chapter 3, we study the domain growth process of a ferromagnet. It obeys the Allen-Cahn growth law [24], $L(t) \sim (t/\tau)^\theta$, where the growth exponent $\theta = 1/2$ and τ is the time-scale. At relatively high values of T ($T \lesssim T_c$), we invoke the macroscopic concept of curvature of domain boundaries to understand the growth law and the behavior of $\tau(T)$. However, at low temperatures ($T \rightarrow 0$), the emerging domains are very pure, i.e., bulk fluctuations within the domains are negligible, hence

a random-walk argument can explain the Allen-Cahn growth law and the behavior of $\tau(T)$. We generalize the random-walk arguments (valid for $T \rightarrow 0$) to understand domain growth at higher T -values by introducing interacting random walkers. This generalization provides a microscopic basis for the concept of curvature-driven dynamics.

In Chapter 4, we have undertaken studies of the autocorrelation function $C(t, s)$ and response function $R(t, s)$ in ferromagnets with quenched disorder, viz., the random-bond Ising model (RBIM) with Glauber kinetics. The dynamical exponent $z = 1/\theta$ associated with the domain growth law is independent of the dimensionality but depends on the disorder amplitude [32]. It has been shown that the dynamical exponent a associated with the zero-field-susceptibility strongly depends on the dimensionality. In the absence of disorder, this dependence can be written as [33]

$$a = \frac{m}{z} \left(\frac{d - d_L}{d^* - d_L} \right), \quad (1.96)$$

where d is the dimension of the system, d^* is the upper critical dimensionality, d_L is the lower critical dimensionality, and $m = 1$ or $m = 2$ for cases with scalar or vector order parameter. For the $2-d$ Ising model without disorder, we have $az = 0.5$. Our numerical results show that this relation is also valid for systems with quenched disorder. This suggests a universality in the relation between the two dynamical exponents a and z .

Bibliography

- [1] N. D. Goldenfeld, *Lectures on Phase Transitions and the Renormalization Group*, Addison-Wesley, Reading (1992).
- [2] A. Pelissetto and E. Vicari, *Phys. Rep.* **6**, 549 (2002).
- [3] M. C. Cross and P. C. Hohenberg, *Rev. Mod. Phys.* **65**, 851 (1993).
- [4] A. S. Mikhailov and G. Ertl, *Science* **272**, 1596 (1996).
- [5] E. Ma, M. Atzmon et al. (eds.), *Phase Transformations and Systems Driven Far from Equilibrium*, Materials Research Society Symposium Proceedings **481** (1998).
- [6] D. Forster, *Hydrodynamic Fluctuations, Broken Symmetry, and Correlation Functions*, *Frontiers in Physics*, Westview Press (1995).
- [7] S. Puri and V. K. Wadhawan (eds.), *Kinetics of Phase Transitions*, CRC Press, Boca Raton, Florida (2009).
- [8] A. J. Bray, *Adv. Phys.* **43**, 357 (1994).
- [9] K. Binder and P. Fratzl, in *Materials Science and Technology Vol. 5*, G. Kostorz (ed.), Wiley-VCH, Weinheim (2001).

- [10] A. Onuki, *Phase Transition Dynamics*, Cambridge University Press, Cambridge (2002).
- [11] S. Dattagupta, and S. Puri, *Dissipative Phenomena in Condensed Matter Physics*, Springer-Verlag, Heidelberg (2004).
- [12] R. J. Glauber, *J. Math. Phys.* **4**, 294 (1963).
- [13] N. G. Van Kampen, *Stochastic Processes in Physics and Chemistry*, North-Holland, Amsterdam (1981).
- [14] K. Binder and D.W. Heermann, *Monte Carlo Simulation in Statistical Physics*, Springer Series in Solid-State Sciences Vol. 80, Springer-Verlag, Heidelberg (2002).
- [15] K. Kawasaki, in *Phase Transitions and Critical Phenomena*, Vol. 2, C. Domb and M. S. Green (eds.), Academic Press, London, pp. 443 (1972).
- [16] K. Kawasaki, *Phys. Rev.* **145**, 224 (1966).
- [17] K. Tafa, S. Puri and D. Kumar *Phys.Rev. E* **64**, 56139 (2001).
- [18] S. Puri and D. Kumar, *Phys. Rev. Lett.* **93**, 025701 (2004).
- [19] M. Suzuki and R. Kubo, *J. Phys. Soc. Jpn.* **24**, 51 (1968).
- [20] K. Binder, *Z. Phys.* **267**, 313 (1974).
- [21] J. W. Cahn and J. E. Hilliard, *J. Chem. Phys.* **31**, 688 (1959).
- [22] H. E. Stanley, *Introduction to Phase Transitions and Critical Phenomena*, Oxford University Press, Oxford (1971).

- [23] P. M. Chaikin and T. C. Lubensky, *Principles of Condensed Matter Physics*, Cambridge University Press (2003).
- [24] S. M. Allen and J. W. Cahn, *Acta Metall.* **27**, 1085 (1979).
- [25] K. Binder and D. Stauffer, *Phys. Rev. Lett.* **33**, 1006 (1974).
- [26] I. M. Lifshitz and V. V. Slyozov, *J. Phys. Chem. Solids* **19**, 35 (1961).
- [27] T. Ohta, D. Jasnow and K. Kawasaki, *Phys. Rev. Lett.* **49**, 1223 (1982).
- [28] W. Feller, *An Introduction to Probability Theory and its Applications*, Wiley (1970).
- [29] P.C. Hohenberg and B.I. Halperin, *Rev. Mod. Phys.* **49**, 435 (1977).
- [30] C. Yeung, *Phys. Rev. Lett.* **61**, 1135 (1988).
- [31] H. Furukawa, *Phys. Rev. B* **40**, 2341 (1989).
- [32] R. Paul, S. Puri and H. Rieger, *Europhys. Lett.* **71**, 061109 (2005).
- [33] F. Corberi, E. Lippiello and M. Zannetti, *Phys. Rev. E* **68**, 046131 (2003).

Chapter 2

Control of Structure Formation in Phase-Separating Systems

2.1 Introduction

In Sec. 1.3, we considered a binary mixture (AB), which is homogeneous (or disordered) at high temperatures and phase-separated (or ordered) at low temperatures. If the homogeneous mixture is rapidly quenched below the critical temperature T_c [see Fig. 1.3], it becomes thermodynamically unstable. Then, the mixture undergoes phase separation via the formation and growth of domains of A-rich and B-rich phases as shown in Fig. 1.4. Much research interest has focused on this far-from-equilibrium evolution [1]. There now exists a good understanding of segregation dynamics for bulk binary mixtures (see Sec. 1.5). In cases where phase separation is driven by diffusion, these coarsening processes may be modeled using kinetic Ising models with locally conserved magnetization, e.g., the spin-exchange Kawasaki-Ising model [2]. The possible spin values ($S_i = \pm 1$) represent the two species of particles that are demixing. The coarse-grained order parameter (magnetization) of such models is described by

the Cahn-Hilliard-Cook (CHC) equation or Model-B [3]. In the dilute limit, where droplets of the minority phase grow in a homogeneous background, Lifshitz and Slyozov (LS) have shown that the average domain size increases as $L(t) \sim t^\phi$, where t is the time after the quench and $\phi = 1/3$ [4]. The LS theory has been qualitatively generalized by Huse [5] to the case where there are approximately equal fractions of the two phases.

Apart from the domain growth laws, experimentalists are also interested in quantitative features of the phase-separating morphologies. An important experimental quantity is the *time-dependent structure factor* $S(\vec{k}, t)$ (\vec{k} being the wave vector) or its inverse Fourier transform, the *correlation function* $C(\vec{r}, t)$ (see Sec. 1.4.3). Our understanding of the structure factor for a phase-separating system is relatively limited. The structure factor exhibits dynamical scaling, $S(\vec{k}, t) = L^d f(kL)$, where d is the dimensionality. It has a single peak at the inverse of the characteristic length scale, $k_m \sim L(t)^{-1}$. With the passage of time, $k_m \rightarrow 0$ as $k_m \sim t^{-\phi}$. We also know the behavior of $S(\vec{k}, t)$ in the limits $k \rightarrow 0$ [i.e., $S(\vec{k}, t) \sim k^4$] [6, 7] and $k \rightarrow \infty$ [i.e., $S(\vec{k}, t) \sim k^{-(d+1)}$]. The latter result is known as Porod's law, and is a result of scattering from sharp interfaces [8]. However, there is still no theory which describes the complete functional form of $S(\vec{k}, t)$.

In this chapter, we study the phase-separation dynamics of a binary mixture with a specific interest in the shape of the structure factor. In particular, we study the effect of a time-dependent temperature on the functional form of the structure factor. The question which motivates our study is whether it is possible to create a domain morphology with a predefined structure factor by temporal variation of external parameters. This issue is of great technological importance, especially in the context of tailoring micro-structures and nano-structures. The present study is a first step in this direction.

In the above context, we study phase separation via computer simulations of (a) the conserved (Kawasaki) Ising model; and (b) the CHC model. In contrast to earlier studies of this problem, we change external parameters (e.g., temperature) during the simulation to influence the shape of the structure factor. We consider a simple protocol for variation of the temperature, viz., the temperature is cycled between high and low values. Depending on the frequency and amplitude of the cycling, we obtain structure factors with multiple peaks, instead of the usual single peak.

This chapter is organized as follows. In Sec. 2.2, we present comprehensive Monte Carlo (MC) results for the Kawasaki-Ising model subjected to a cyclical variation of the temperature [9]. We also present analytical arguments to understand the evolution of the structure factor and correlation function during the heating part of the cycle. In Sec. 2.3, we present analogous results for the CHC model, which is the coarse-grained counterpart of the Kawasaki-Ising model. Finally, Sec. 2.4 concludes this chapter with a summary and discussion.

2.2 Phase Separation in the Kawasaki-Ising Model with Time-Dependent Temperature

A binary (AB) mixture is usually described by the Ising model, with Hamiltonian [cf. Eq. (1.2)]

$$H = -J \sum_{\langle ij \rangle} S_i S_j, \quad S_i = \pm 1. \quad (2.1)$$

Here, S_i denotes the spin variable at site i . We consider two-state spins – $S_i = +1$ denotes an A-atom and $S_i = -1$ denotes a B-atom. If the exchange interaction $J > 0$, the system segregates into A-rich and B-rich regions below the miscibility gap. In

Eq. (2.1), the subscript $\langle ij \rangle$ denotes a summation over nearest-neighbor pairs i and j . The total magnetization $M = \sum_{i=1}^N S_i$ ($= N_A - N_B$, where A and B are total numbers of A and B, respectively) is a conserved quantity. We associate stochastic dynamics with the Ising model by placing it in contact with a heat bath. The appropriate dynamics for the phase-separation problem is spin-exchange kinetics or Kawasaki kinetics (see Sec. 1.3.1). It is straightforward to implement an MC simulation of the Kawasaki-Ising model. In a single step of MC dynamics, we choose at random a pair of adjacent spins on the lattice. The change in energy δH that would occur if the spins were exchanged is computed. The step is then accepted or rejected with Metropolis acceptance probability [10]:

$$P = \begin{cases} \exp(-\beta\delta H), & \text{if } \delta H \geq 0, \\ 1, & \text{if } \delta H < 0. \end{cases} \quad (2.2)$$

Here, $\beta = (k_B T)^{-1}$ denotes the inverse temperature. In the simulations reported here, the temperature has a time-dependent form $T(t)$. This process is repeated for many steps. One Monte Carlo step (MCS) is completed when this algorithm is performed N times (where N is the total number of spins), regardless of whether the move is accepted or rejected.

All our simulations have been performed on a 2-dimensional Kawasaki-Ising model, defined on a square lattice of size L^2 ($L = 512$) with periodic boundary conditions. The simulation starts with a randomly-mixed state with equal numbers of up and down spins ($\rho = 0.5$ is the density of up or down spins, which corresponds to a mean magnetization $m = 0$). At time $t = 0$, the system is quenched to a temperature $T = 1.5$, measured in units of J ($T_c \simeq 2.269$ for a 2- d Ising model on a square lattice). After the system has evolved for time t_1 , we heat the system to $T = \infty$ (first heating),

and allow it to evolve till time t_2 . Therefore, the duration of the first heating period is $t_2 - t_1$. The system is then quenched again to $T = 1.5$ (second quench till time t_3), and then heated again (second heating till time t_4), etc. The precise temperature protocol followed in different simulations will be specified at the appropriate place.

2.2.1 First Quench

For purposes of reference, in Fig. 2.1 we show the evolution of the system after a quench to $T = 1.5$ at $t = 0$. The frames in this figure correspond to $t = 5 \times 10^4$, 2×10^5 , 6×10^5 and 10^6 MCS. Regions with $S_i = +1$ (A-rich) and $S_i = -1$ (B-rich)

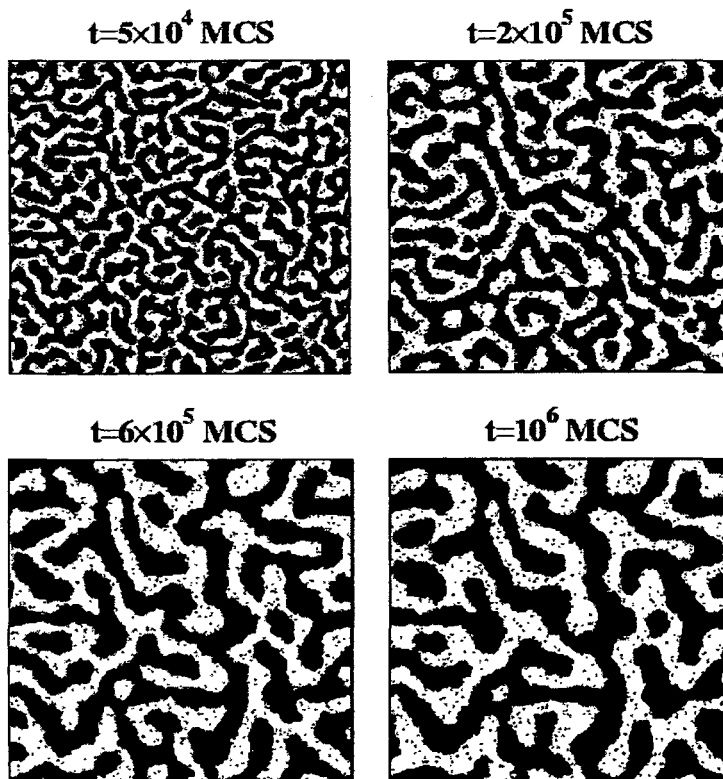


Figure 2.1: Evolution snapshots obtained from a simulation of the Kawasaki-Ising model. The system was quenched from $T = \infty$ to $T = 1.5$ at time $t = 0$. The up spins denote A-atoms and are marked in black, whereas the down spins (B-atoms) are unmarked. The snapshots correspond to different times, measured in Monte Carlo steps or MCS.

are marked in black and white, respectively. The structure of the evolving system is characterized by the correlation function [see Sec. 1.4.3]:

$$\begin{aligned} C(\vec{r}_i, \vec{r}_j; t) &\equiv \langle S_i S_j \rangle - \langle s_i \rangle \langle s_j \rangle \\ &= \langle s_i s_j \rangle - m^2. \end{aligned} \tag{2.3}$$

Here, the angular brackets denote an averaging over the initial ensemble and different noise realizations. As the system is translationally invariant, the correlation function depends only on $\vec{r} = \vec{r}_j - \vec{r}_i$:

$$\begin{aligned} C(\vec{r}_i, \vec{r}_j; t) &= C(\vec{r}_i, \vec{r}_i + \vec{r}; t) \\ &= C(\vec{r}, t). \end{aligned} \tag{2.4}$$

Actually, most experiments study the structure factor, which is the Fourier transform of the correlation function:

$$S(\vec{k}, t) = \sum_{\vec{r}} e^{i\vec{k}\cdot\vec{r}} C(\vec{r}, t). \tag{2.5}$$

Since the system is isotropic, we can improve statistics by spherically averaging the correlation function and the structure factor – the corresponding quantities are denoted as $C(r, t)$ and $S(k, t)$, respectively. The numerical results presented here are obtained as averages over 10 independent runs on systems of size 512^2 . In Fig. 2.2, we show the correlation function [$C(r, t)$ vs. r] and the structure factor [$S(k, t)$ vs. k] for three different times. Notice that we do not present here the usual scaling plot, where data sets at different times collapse onto a master function (cf. Fig. 1.9).

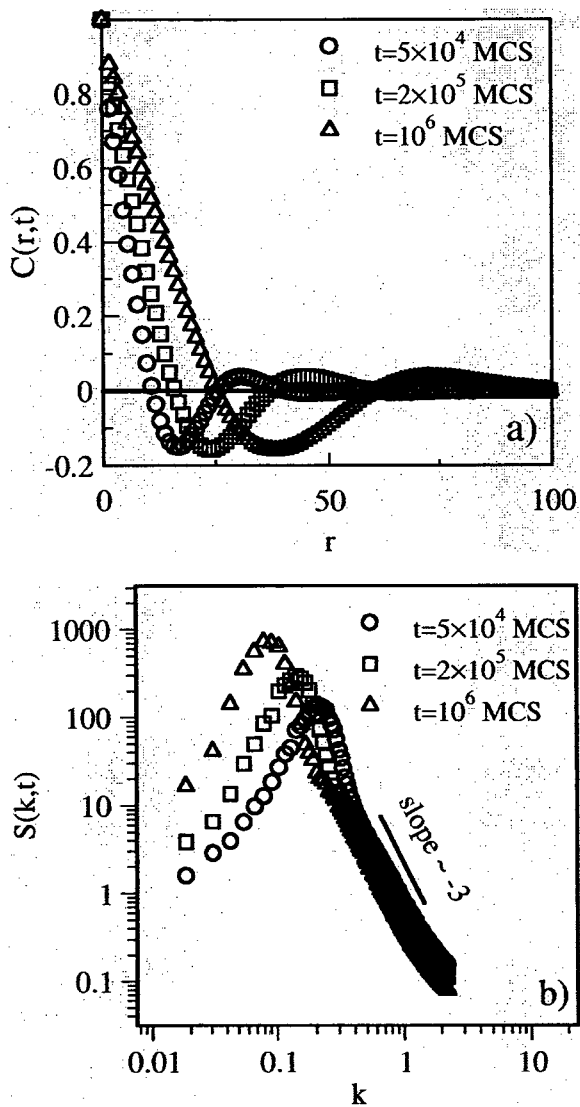


Figure 2.2: (a) Correlation functions $[C(r,t) \text{ vs. } r]$ at three different times after the first quench shown in Fig. 2.1. (b) Structure factor data $[S(k,t) \text{ vs. } k]$ for the same times as in (a). The line of slope -3 denotes the Porod law in $d = 2$, $S(k,t) \sim k^{-3}$ as $k \rightarrow \infty$.

Figure 2.2 will serve as a reference point for later results, obtained for a variety of heating-cooling cycles. The structure factor in Fig. 2.2(b) contains information about the presence of sharp interfaces (defects) in the phase ordering system. As $k \rightarrow \infty$, the tail of the structure factor decays to zero as $S(k,t) \sim k^{-(d+1)}$, which is referred

to as *Porod's law*. The Porod tail only persists up to values of k corresponding to the typical width of the wall, $k < \xi^{-1}$.

Finally, let us examine the time-dependence of the characteristic domain size $L(t)$. There are many equivalent definitions for measuring the domain size. For example, $L(t)$ can be defined as the point where the correlation function in Fig. 2.2(a) first crosses zero. Alternatively, we can define the length scale as the inverse of the location of the structure-factor peak [$L(t) \sim k_m^{-1}$], or the inverse of the first moment of the structure factor [$L(t) \sim \langle k \rangle^{-1}$]. All these definitions are equivalent in the scaling regime. In this chapter, we use the definition $L \sim k_m^{-1}$. In Fig. 2.3, we show the time-dependence of the length scale on a log-log plot. We see that the domain growth depicted in Fig. 2.1 is consistent with the LS growth law, $L(t) \sim t^{1/3}$.

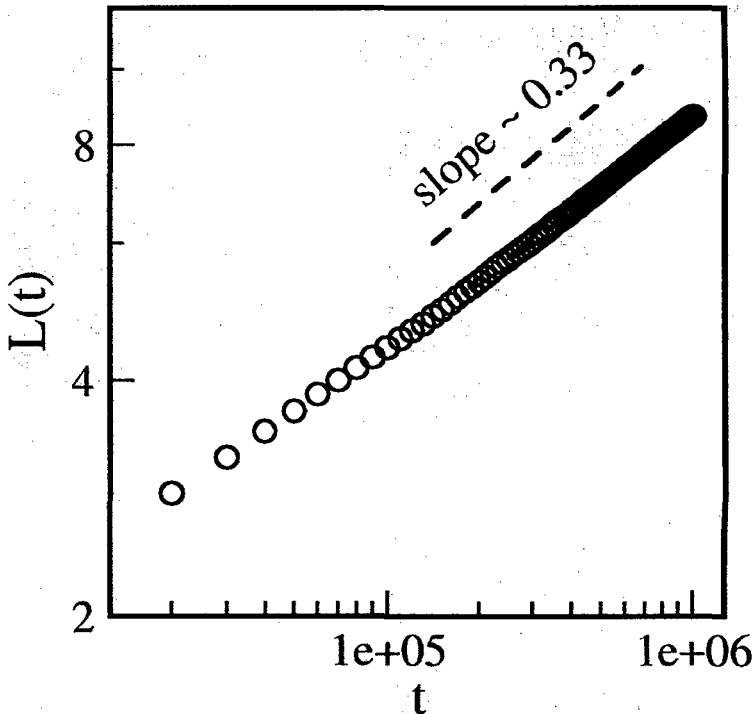


Figure 2.3: Time-dependence of domain size [$L(t)$ vs. t] for the evolution shown in Fig. 2.1. The line of slope $1/3$ denotes the Lifshitz-Slyozov (LS) growth law, $L(t) \sim t^{1/3}$. Similar to Fig. 1.8, obtained from CHC model [see Eq. (1.91)]

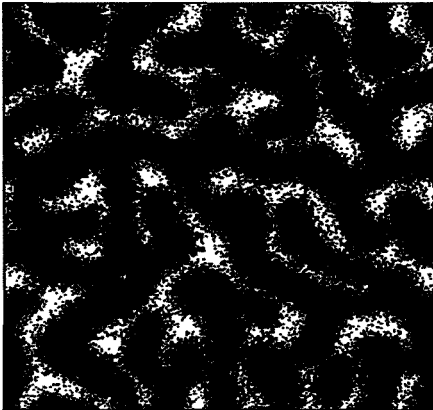
2.2.2 First Heating

After, the system shown in Fig. 2.1 has evolved for time $t_1 = 10^6$ MCS, we suddenly heat the system to $T = \infty$ ($\beta = 0$). The preferred equilibrium structure is now the homogeneous state, and the domain structure will start melting. At $T = \infty$, the acceptance probability P in Eq. (2.2) is always unity, regardless of whether the proposed move increases or decreases the system energy. Thus, all proposed spin exchanges will be accepted – on average, each spin pair is exchanged once during 1 MCS. This means that every particle will make two steps in one of four randomly determined directions, either along the x -axis or the y -axis. Therefore, within a few MCS, the domain walls get fuzzier and domains becomes less distinctive. Inside a domain, the concentration of particles with opposite spin increases.

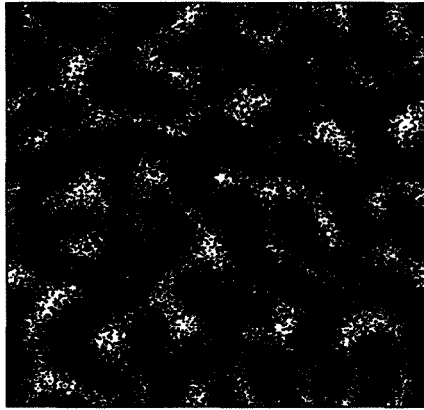
We start the first heating with the final configuration (at $t_1 = 10^6$ MCS) in Fig. 2.1. We evolve the system for 700 MCS at temperature $T = \infty$. The snapshots of the resultant disordering dynamics are shown in Fig. 2.4.

In Fig. 2.5, we show the evolution of the structure factor during the heating process. We see that the structure factor retains a peak at small values of k after heating for 700 MCS. The peak amplitude becomes lower as heating proceeds. The large values of k correspond to small-scale structure, which is seen to become disordered as the corresponding $S(k, t)$ is flat. A homogeneous system of spins with density $\rho = 0.5$ (i.e., initial state for first quench) has $S(\vec{k}, 0) = 1$ in our units – the corresponding data is denoted by a solid line in Fig. 2.5. The corresponding correlation function is $C(\vec{r}, 0) = \delta_{\vec{r}, 0}$. The time-dependence of the length scale during the first heating is shown in Fig. 2.6.

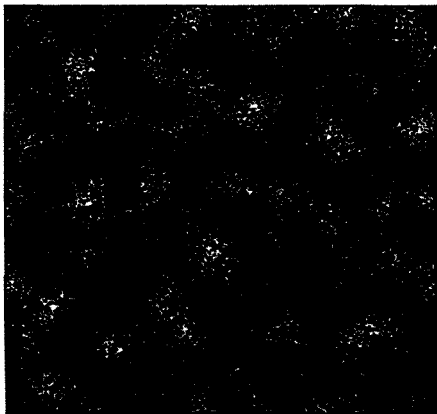
$t=t_1+70$ MCS



$t=t_1+140$ MCS



$t=t_1+280$ MCS



$t=t_1+700$ MCS



Figure 2.4: Evolution snapshots of the Kawasaki-Ising model during the first heating period. The system was heated to $T = \infty$ at time $t = t_1 = 10^6$ MCS, corresponding to the final snapshot in Fig. 2.1 From top left, the frames show the system after $t = t_1 + 70$, $t_1 + 140$, $t_1 + 280$ and $t_1 + 700$ MCS.

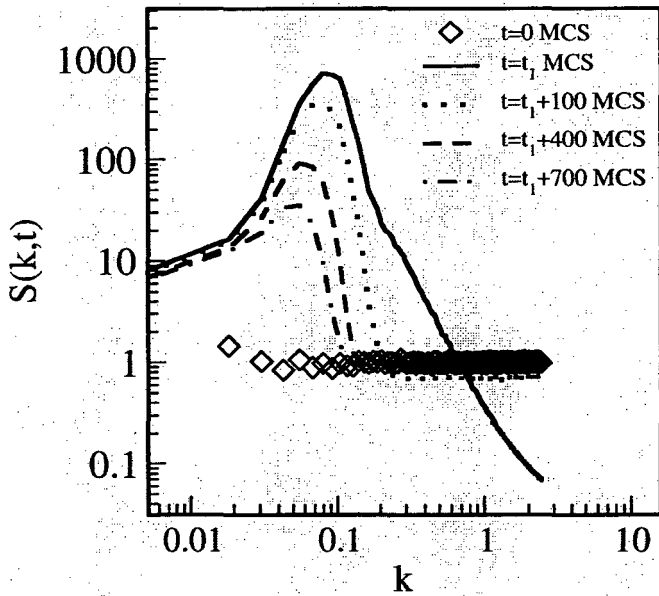


Figure 2.5: Structure factor for three different times during first heating: $t = t_1 + 100, t_1 + 400, t_1 + 700$ MCS. For comparison, we have also plotted the structure factor of the homogeneous initial state of the first quench ($t = 0$), and the structure factor at the end of the first quench, $t_1 = 10^6$ MCS.

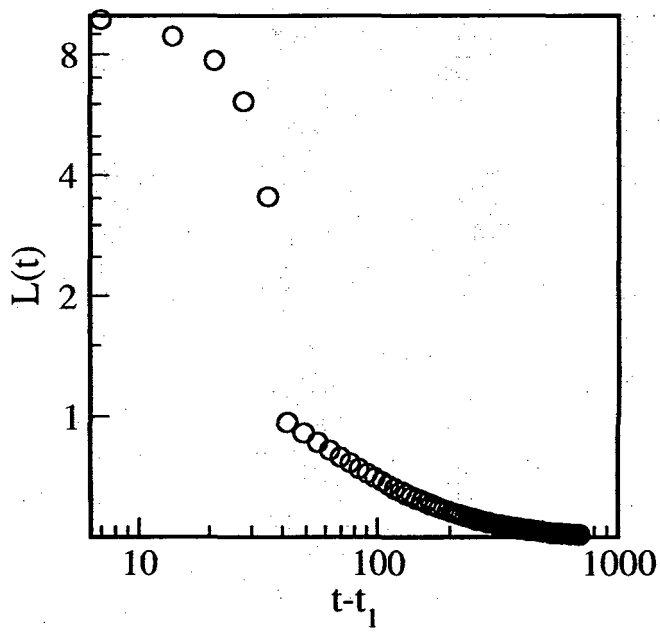


Figure 2.6: Time-dependence of domain size $[L(t) \text{ vs. } t]$ during first heating at temperature $T = \infty$. The duration of the first heating period is 700 MCS.

We would like to know how the heating process influences the structure factor of the system. In other words, if $S(\vec{k}, t_1)$ is the structure factor when heating starts, is it possible to predict $S(\vec{k}, t)$ for $t > t_1$? Recall that the particles are performing random walks in $d = 2$. After t MCS of heating, the average displacement of a particle is $\sqrt{2t}$. The corresponding probability distribution for a particle to be displaced (x, y) from its initial position is

$$g_\sigma(x, y) = g_\sigma(x) g_\sigma(y) = \frac{1}{\sqrt{2\pi\sigma^2}} e^{-x^2/(2\sigma^2)} \cdot \frac{1}{\sqrt{2\pi\sigma^2}} e^{-y^2/(2\sigma^2)}, \quad (2.6)$$

where $\sigma = \sqrt{t}$. The correlation function changes over time by convolution with the Gaussian distribution. The predicted correlation function after $(t-t_1)$ MCS of heating is

$$\begin{aligned} C(x, y, t) &= C(x, y, t_1) * g_{\tilde{\sigma}}(x) * g_{\tilde{\sigma}}(y) \\ &= \frac{1}{2\pi\tilde{\sigma}^2} \int_{-\infty}^{\infty} dx' \int_{-\infty}^{\infty} dy' C(x', y', t_1) \exp\left[-\frac{(x-x')^2 + (y-y')^2}{2\tilde{\sigma}^2}\right], \end{aligned} \quad (2.7)$$

where $\tilde{\sigma}^2 = 2(t-t_1)$. The above expression applies only for $r = \sqrt{x^2 + y^2} > 0$. In polar coordinates,

$$\begin{aligned} C(r, t) &= \frac{e^{-r^2/(2\tilde{\sigma}^2)}}{2\pi\tilde{\sigma}^2} \int_0^{\infty} dr' r' C(r', t_1) e^{-r'^2/(2\tilde{\sigma}^2)} \int_0^{2\pi} d\theta' \exp\left(\frac{rr' \cos \theta'}{\tilde{\sigma}^2}\right) \\ &= \frac{e^{-r^2/(2\tilde{\sigma}^2)}}{\tilde{\sigma}^2} \int_0^{\infty} dr' r' C(r', t_1) e^{-r'^2/(2\tilde{\sigma}^2)} I_0\left(\frac{rr'}{\tilde{\sigma}^2}\right), \quad r > 0, \end{aligned} \quad (2.8)$$

where $I_0(z)$ is the zeroth-order modified Bessel function.

For $r = 0$, we always have $C(r = 0, t) = 1$. This is clear from the definition in Eq. (2.3) as $\langle S_i^2 \rangle = 1$ and $m = 0$ for a critical quench. In Fig. 2.7, we show the correlation function at three different times in the heating period. The solid lines

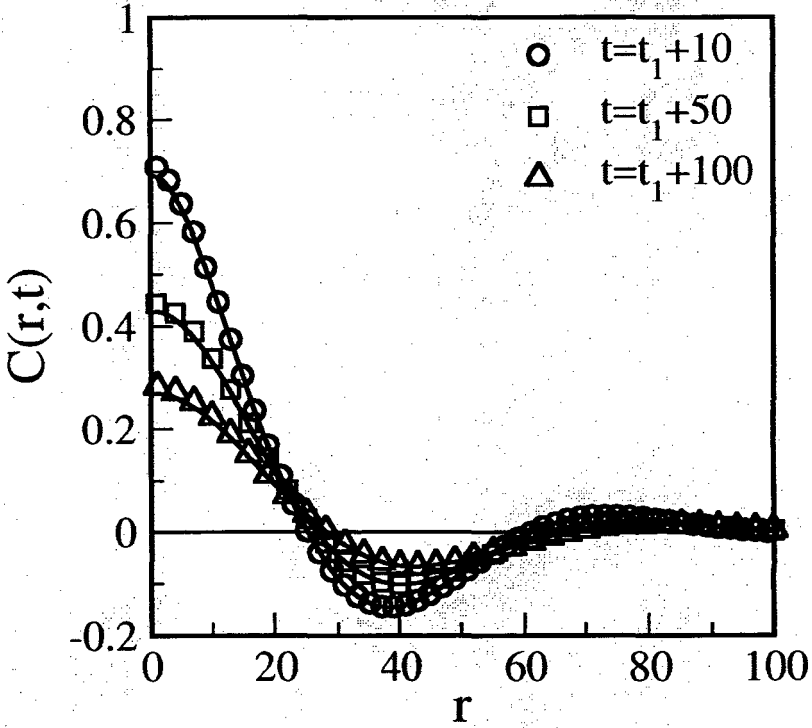


Figure 2.7: Correlation functions at three different times during first heating. The solid lines denote the expression for $C(r, t)$ in Eq. (2.8).

denote the expression in Eq. (2.8), where $C(r, t_1)$ is obtained numerically. There is an excellent agreement between the simulation data and Eq. (2.8).

Next, we consider the structure factor, which is the Fourier transform of the correlation function. On the discrete lattice, we have [analogous to Eq. (2.7)]

$$C(\vec{r}, t) = \frac{1}{2\pi\tilde{\sigma}^2} \sum_{\vec{r}'} C(\vec{r}', t_1) \exp\left[-\frac{(\vec{r} - \vec{r}')^2}{2\tilde{\sigma}^2}\right] + [1 - a(t)] \delta_{\vec{r}, 0}, \quad (2.9)$$

where we have explicitly included the case $\vec{r} = 0$.

Clearly, we have

$$a(t) = \frac{1}{2\pi\sigma^2} \sum_{\vec{r}'} C(\vec{r}', t_1) e^{-\vec{r}'^2/(2\tilde{\sigma}^2)}. \quad (2.10)$$

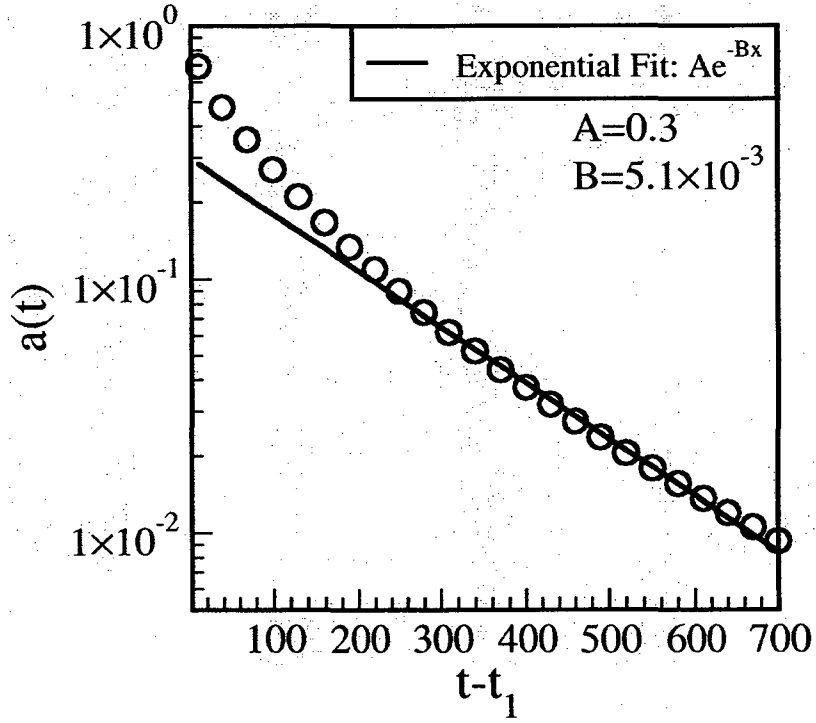


Figure 2.8: Decay of $a(t)$ with time. The solid line denotes an exponential fit with parameters $A = 0.3$ and $B = 0.005$.

The variation of $a(t)$ with t is shown in Fig. 2.8. The corresponding expression for $S(\vec{k}, t)$ is

$$\begin{aligned}
 S(\vec{k}, t) &= \sum_{\vec{r}} e^{i\vec{k}\cdot\vec{r}} C(\vec{r}, t) \\
 &= \frac{1}{2\pi\tilde{\sigma}^2} \sum_{\vec{r}} e^{i\vec{k}\cdot\vec{r}} \sum_{\vec{r}'} C(\vec{r}', t_1) \exp\left[-\frac{(\vec{r}-\vec{r}')^2}{2\tilde{\sigma}^2}\right] + 1 - a(t) \\
 &\simeq S(\vec{k}, t_1) e^{-k^2\tilde{\sigma}^2/2} + 1 - a(t). \tag{2.11}
 \end{aligned}$$

In Fig. 2.9, we plot $S(k, t)$ vs. k for three times in the first heating period. The solid lines, denote the expression in Eq. (2.11) - they are seen to be in excellent agreement with the numerical data. Notice that the Porod tail immediately disappears as we

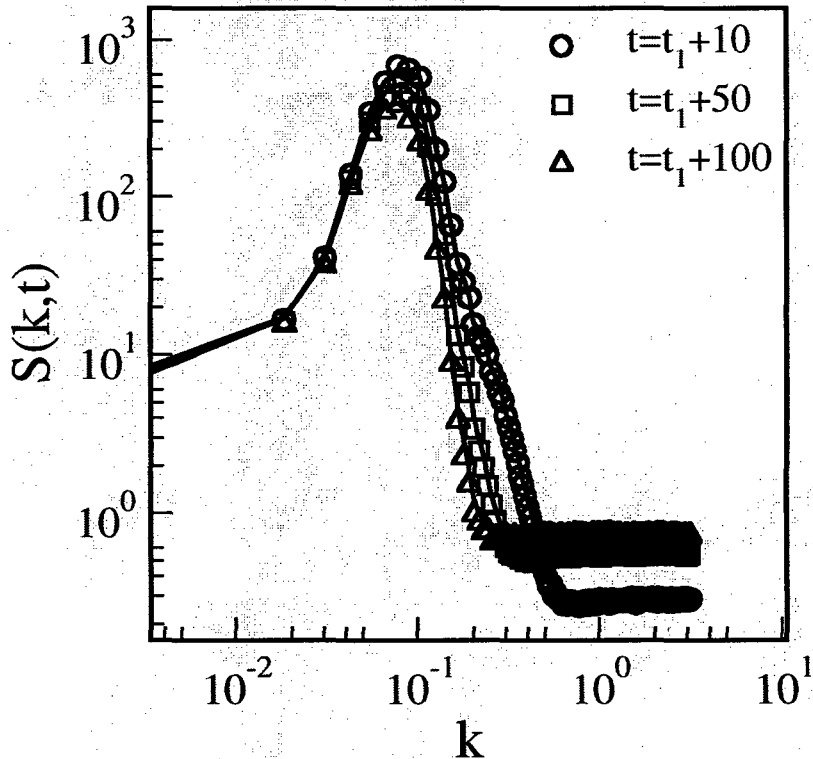


Figure 2.9: Structure factors at three different times during first heating. The solid lines denote the expression in Eq. (2.11).

start heating. This is because the interfaces become fuzzy as particles at the interfaces start performing random walks - the flat portion of the structure factor has the value $S(k, t) \simeq 1 - a(t)$, which corresponds to the difference between $C(\vec{r} = 0, t) = 1$ and $\lim_{r \rightarrow 0} C(r, t) = a(t)$ in Fig. 2.7. As $t \rightarrow \infty$, $a(t) \rightarrow 0$, and $S(k, t) \simeq 1$, which corresponds to the initial homogeneous state in Fig. 2.5.

2.2.3 Second Quench

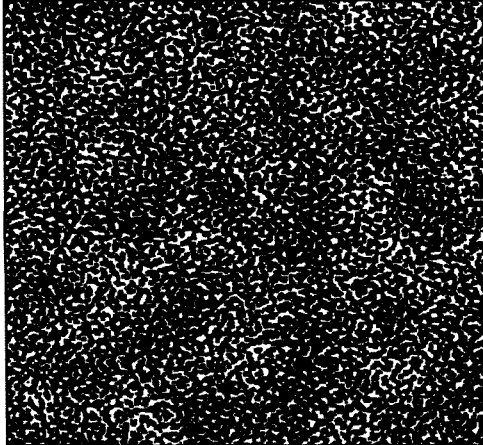
In a single quench experiment, the small-distance scale corresponds to the large- k part of the structure factor. This is the region where domain formation begins, with a peak emerging at large k and moving to smaller values of k as time progresses. As we have seen earlier, the large- k region after heating (see Fig. 2.5) resembles the

homogeneous initial condition of a single quench experiment. The heating process breaks up domain structure, starting from the smallest length scales, and progressing to the larger length scales. We expect that we can grow a second peak by continuing the evolution of the heated system in the previous subsection at a lower temperature. Therefore, we undertake a second quench at time t_2 . Again, the system is cooled to the temperature $T = 1.5$.

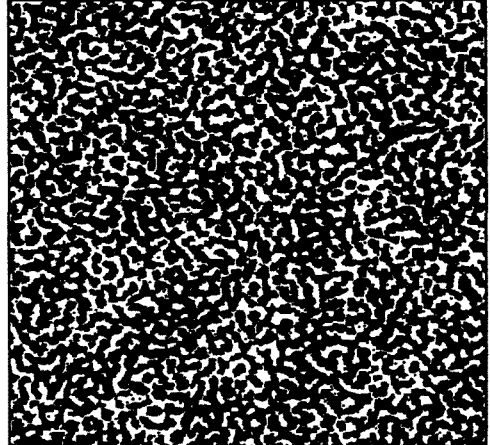
Recall that we started our simulation with a homogeneous system with $\rho = 0.5$. This system was evolved at $T = 1.5$ for $t_1 = 10^6$ MCS. Subsequently, it was heated for 700 MCS ($t_2 = t_1 + 700$) at $T \rightarrow \infty$. Now, the temperature has been quenched again to $T = 1.5$. The snapshots of domain growth for this second quench are shown in Fig. 2.10. The snapshot at $t = t_2 + 400$ MCS clearly shows the existence of structure on two length-scales. As we will see shortly, this two-scale morphology is characterized by a structure factor with two peaks.

The structure factor of a homogeneous system with equal number of up and down spins ($\rho = 0.5$, and mean magnetization $m = 0$) is $S(\vec{k}, 0) \simeq 1$. It is clear from Fig. 2.9 that it takes some amount of heating before the large- k part of structure factor reaches the value 1. We perform the second quench before $S(\vec{k}, t)$ reaches the value 1 due to heating. The evolution of the corresponding two-peak structure factor is shown in Fig. 2.11. Notice that one of the peaks at k_1 (corresponding to large-scale structure) is almost static, whereas the other peak at k_2 (corresponding to small-scale structure) moves with time. The time-dependence of the relevant length scale, defined as $L_1 = k_1^{-1}$ and $L_2 = k_2^{-1}$, is shown in Fig. 2.12.

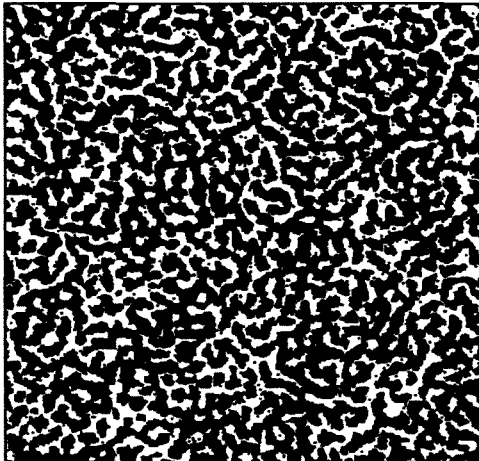
$t=t_2+400$ MCS



$t=t_2+4000$ MCS



$t=t_2+10000$ MCS



$t=t_2+20000$ MCS

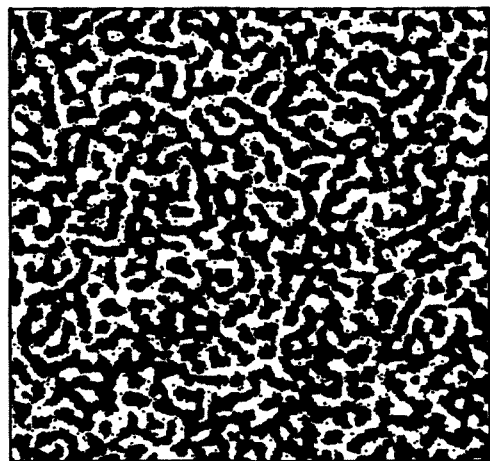


Figure 2.10: Evolution snapshots obtained from the Kawasaki-Ising model during the second quench. The frames show the configuration of the system at $t_2 + 400$, $t_2 + 4000$, $t_2 + 10000$ and $t_3 = t_2 + 20000$ MCS.

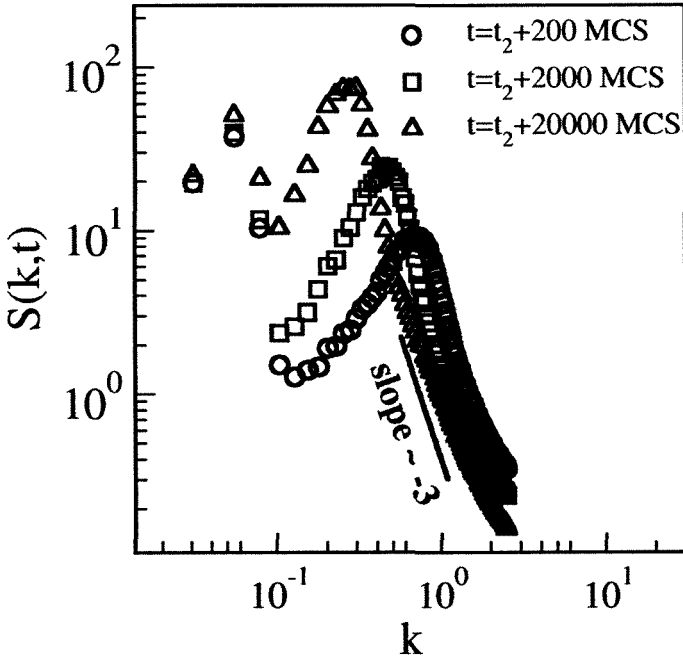


Figure 2.11: Structure factors at three different times during the second quench.

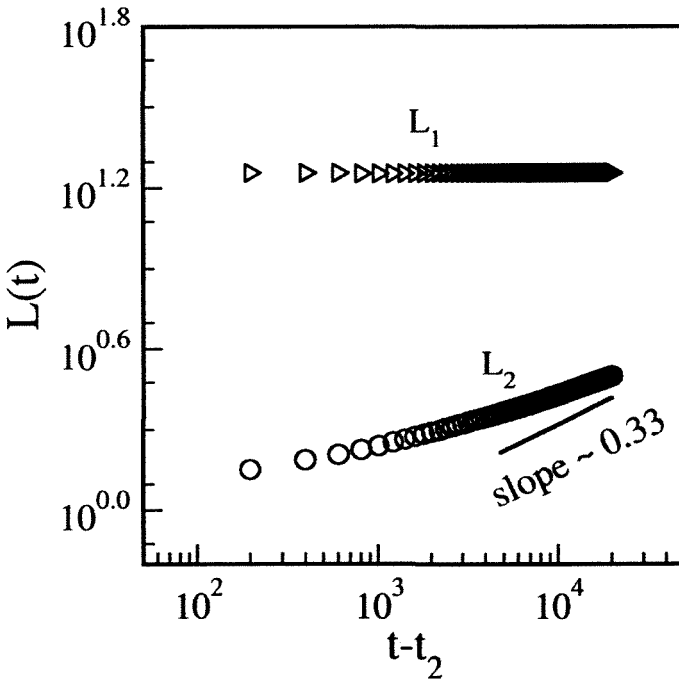


Figure 2.12: Time-dependence of domain size, $L(t)$ vs t , during the second quench. We show the length scales corresponding to the inverse of the first and second peaks of the structure factor.

The flat region of the structure factor during first-heating, which is a constant value < 1 characterizes a homogeneous system with mean magnetization different from 0. Recall from Eq. (2.11) that the flat portion of the structure factor

$$S(\vec{k}, t) \simeq 1 - a(t),$$

where $a(t) \rightarrow 0$ as the heating continues. Therefore, the effective magnetization of the corresponding homogeneous system is

$$m_{\text{eff}}(t) = \sqrt{a(t)},$$

and the corresponding density is

$$\rho_{\text{eff}} = \frac{1 + \sqrt{a(t)}}{2}. \quad (2.12)$$

We can obtain a better understanding of the growth of the second peak during the second quench. The heating period in first-heating was 700 MCS. At the end of this time period, we estimate the flat portion of the structure factor as $S(\vec{k}, t) \simeq 0.98$ from Fig. 2.5. This corresponds to $m_{\text{eff}} \simeq 0.14$. For purposes of comparison, we undertake a conventional first-quench simulation of phase separation at $T = 1.5$. The initial condition consisted of a homogeneous mixture with $m_{\text{eff}} \simeq 0.14$. In Fig. 2.13, we compare the two-peak structure factor from one second-quench simulation with the usual one-peak structure factor from one off-critical ($m_{\text{eff}} \simeq 0.14$) simulation. Other than the first peak, the structure factors are in excellent agreement.

The above results clarify the general scenario. The first quench leads to conventional phase-separation dynamics. When the system is heated, the domains melt at small length-scale, but an imprint of the larger domain length-scale survives. The sec-

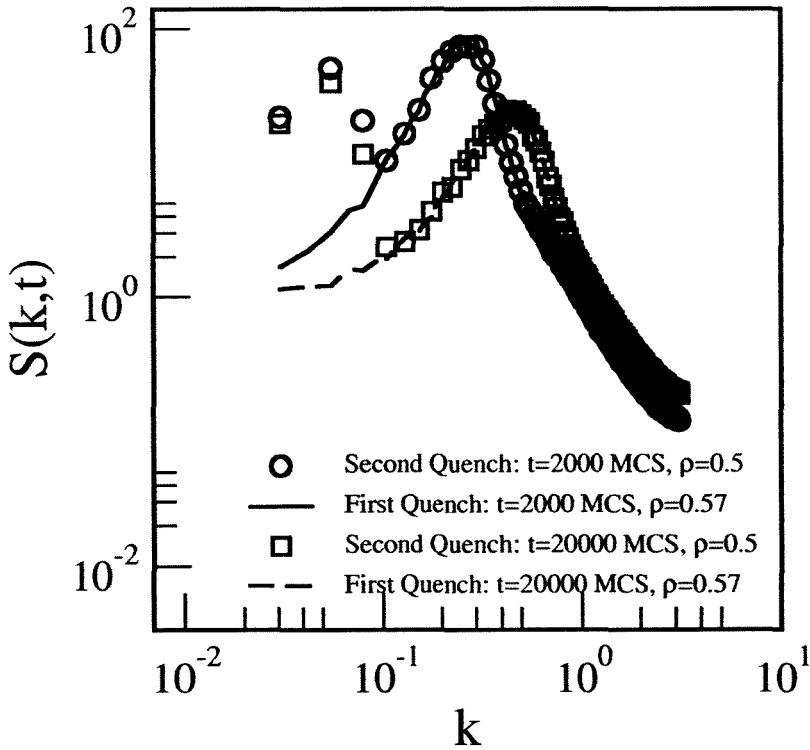


Figure 2.13: Structure factors at times $t_2 + 2000$ MCS and $t_2 + 20000$ MCS during the second quench. For comparison, the structure factors for a first-quench simulation are shown at times $t = 2000$ MCS and $t = 20000$ MCS. For the latter simulation, the parameters were $T = 1.5$ and $\rho = 0.57$.

ond quench leads to the re-emergence of domains from the homogeneous state. This is characterized by the usual LS growth law, $L_2(t) \sim (t - t_2)^{1/3}$. This coexists with the larger length scale L_1 , which is approximately static. If the second quench lasts sufficiently long, L_2 becomes comparable to L_1 - subsequently, the system segregates in the usual manner.

2.2.4 Further Heating and Quenching

Now that the scenario is clear, we can generalize it to the case of multiple heating and quenching. For example, we have performed a second-heating simulation at $T = \infty$, by starting with the system at $t_3 = t_2 + 20000$ MCS. We heat the system upto $t_3 + 25$

MCS and the evolution snapshots are shown in Fig. 2.14(a). Similar to first-heating [cf. Fig. 2.6], we also show the structure factor at three different times in Fig. 2.14(b) and time-dependence of the length scale during the second heating in Fig. 2.14(c).

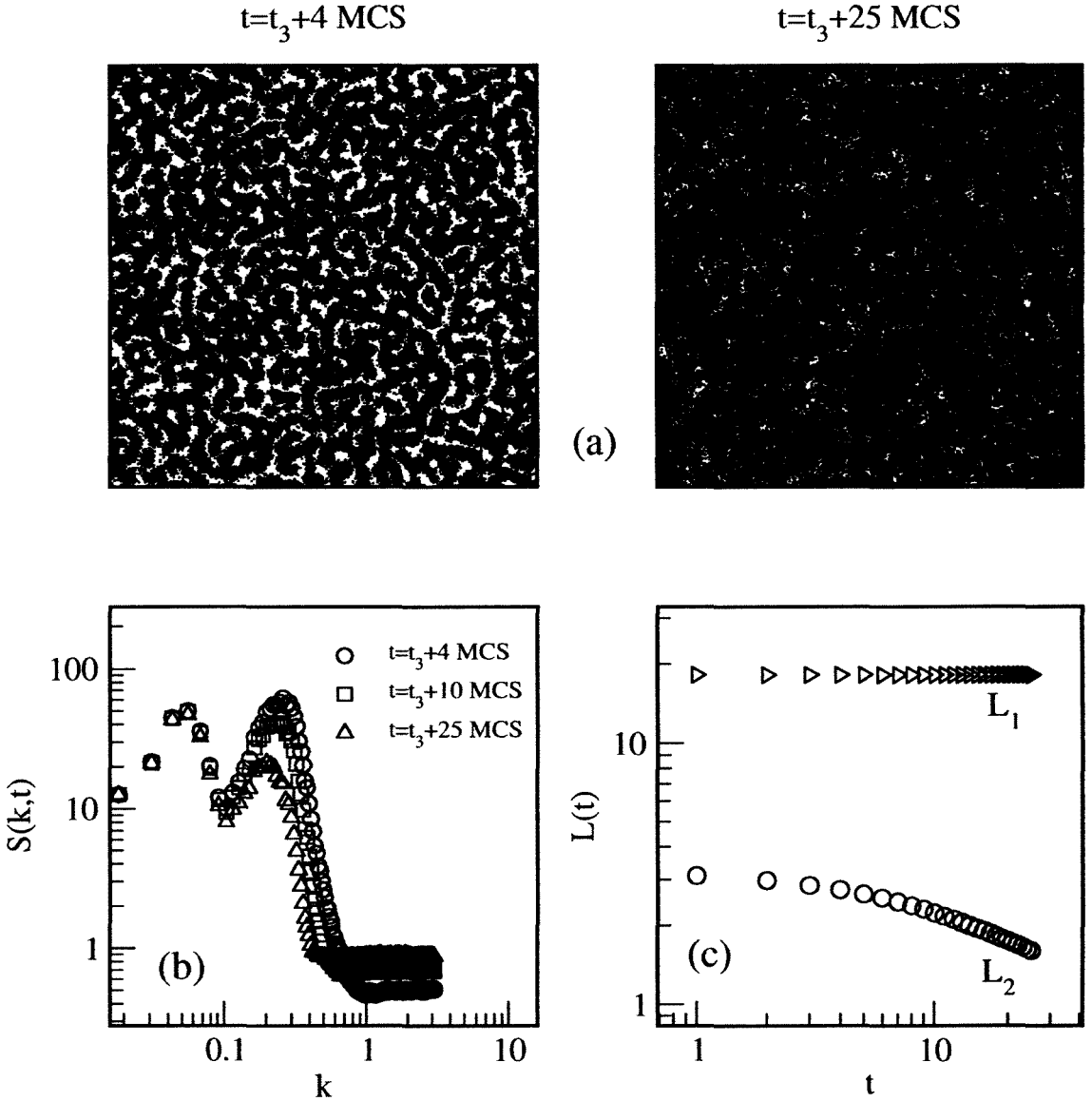


Figure 2.14: (a) Evolution snapshots at $t_3 + 4$ and $t_3 + 25$ MCS during the second heating. (b) Structure factors at three times during the second heating. (c) Time-dependence of domain size during second heating.

The third quench is performed at $t_4 = t_3 + 25$ MCS. The resultant evolution morphology in Fig. 2.15(a) has three length scales.

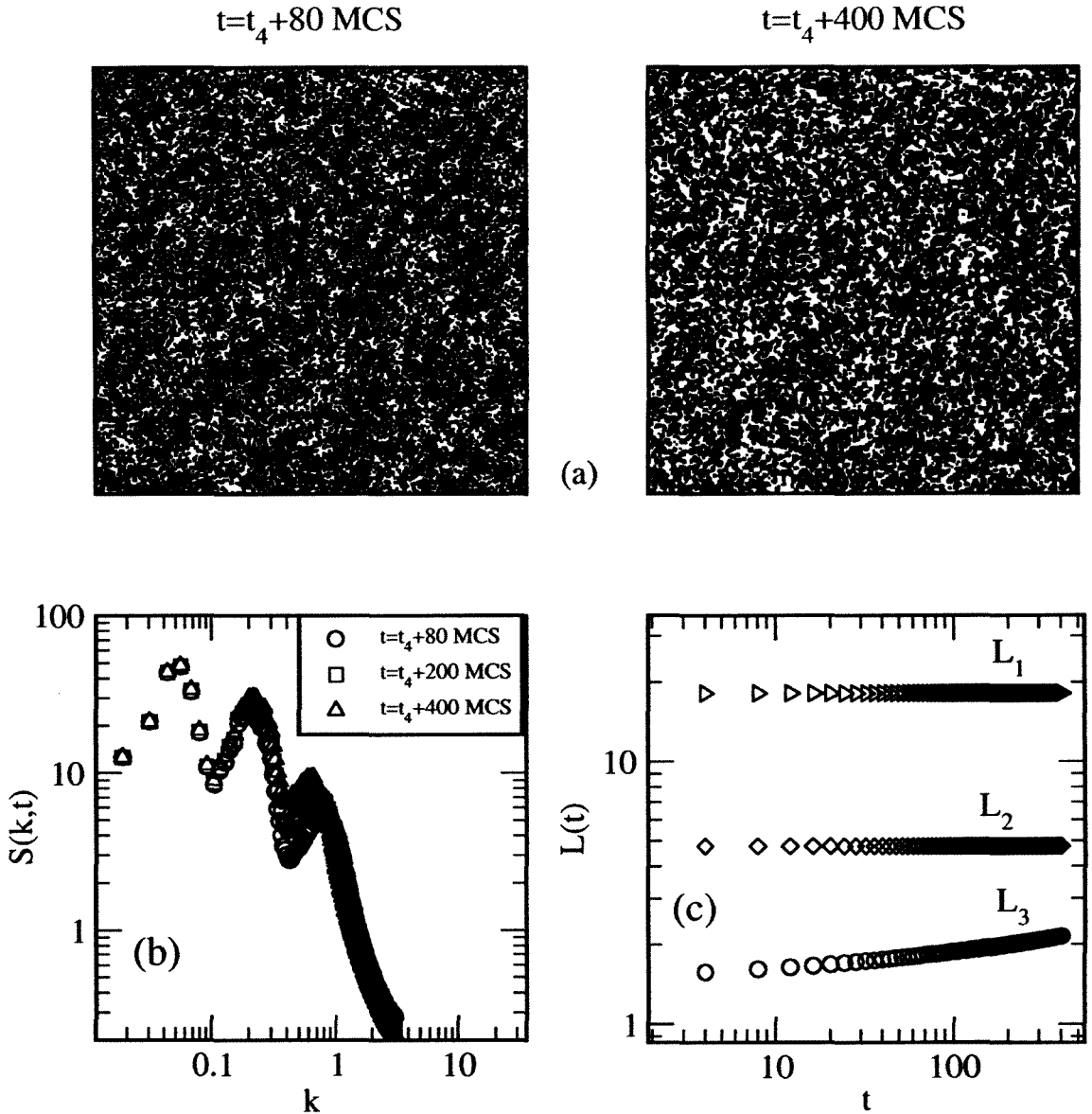


Figure 2.15: (a) Evolution snapshots at $t_4 + 80$ and $t_4 + 400$ MCS during the third quench. The third quench starts at t_4 MCS. (b) Structure factors at three times during the third quench. (c) Time-dependence of domain sizes during third quench.

In Fig. 2.15(b), we see that two of these are static and the third one is increases

with time. The time-dependence of these length scales is shown in Fig. 2.15(c). In general, n quenches give rise to a morphology with n length scales. However, we must be careful that the heating period is not so long that it washes out part or all of the structure existing at the end of the previous quench.

2.3 Cahn-Hilliard-Cook Model for Phase Separation

In the previous section, we have described a method to generate a multi-scale structure factor from the Kawasaki-Ising model. Let us now approach this problem via the CHC model, which is the appropriate coarse-grained model for phase-separation. In this model, the system is described by an order parameter $\psi(\vec{r}, t) = \rho_A(\vec{r}, t) - \rho_B(\vec{r}, t)$, where ρ_A and ρ_B denote the local densities of species A and B. The CHC equation for phase separation is obtained as follows (cf. Sec. 1.5):

$$\begin{aligned} \frac{\partial}{\partial t} \psi(\vec{r}, t) &= -\vec{\nabla} \cdot \vec{J}(\vec{r}, t) \\ &= \vec{\nabla} \cdot \left[D \vec{\nabla} \mu(\vec{r}, t) + \theta(\vec{r}, t) \right] \\ &= \vec{\nabla} \cdot \left[D \vec{\nabla} \left(\frac{\delta F}{\delta \psi} \right) + \vec{\theta}(\vec{r}, t) \right]. \end{aligned} \quad (2.13)$$

In Eq. (2.13), the quantities \vec{J} , D and μ denote the current, diffusion coefficient, and chemical potential difference between A and B, respectively. The Gaussian white noise term $\vec{\theta}(\vec{r}, t)$ has zero average and obeys the fluctuation-dissipation relation:

$$\begin{aligned} \langle \vec{\theta}(\vec{r}, t) \rangle &= 0, \\ \langle \vec{\theta}_i(\vec{r}', t') \vec{\theta}_j(\vec{r}'', t'') \rangle &= 2Dk_B T \delta_{ij} \delta(\vec{r}' - \vec{r}'') \delta(t' - t''). \end{aligned} \quad (2.14)$$

The chemical potential is obtained as a functional derivative of the Helmholtz free energy, which is usually taken to have the ψ^4 -form:

$$F \simeq \int d\vec{r} \left[-\frac{1}{2}a(T_c - T)\psi^2 + \frac{b}{4}\psi^4 + \frac{K}{2}(\vec{\nabla}\psi)^2 \right]. \quad (2.15)$$

Here, a , b and K (all greater than 0) are the parameters of the Ginzburg-Landau free energy. Replacing Eq. (2.15) in Eq. (2.13), the CHC equation has the following form:

$$\frac{\partial}{\partial t}\psi(\vec{r}, t) = \vec{\nabla} \cdot \left\{ D\vec{\nabla} [-a(T_c - T)\psi + b\psi^3 - K\nabla^2\psi] + \vec{\theta}(\vec{r}, t) \right\}. \quad (2.16)$$

We will use the dimensionless version of the CHC equation, which is obtained by a suitable rescaling of space, time and order parameter [see Eq. (1.92)]:

$$\frac{\partial}{\partial t}\psi(\vec{r}, t) = \vec{\nabla} \cdot \left\{ \vec{\nabla} [\pm\psi + \psi^3 - K\nabla^2\psi] + \vec{\theta}(\vec{r}, t) \right\}, \quad (2.17)$$

where

$$\begin{aligned} \langle \vec{\theta}(\vec{r}, t) \rangle &= 0, \\ \langle \vec{\theta}_i(\vec{r}', t') \vec{\theta}_j(\vec{r}'', t'') \rangle &= 2\epsilon\delta_{ij}\delta(\vec{r}' - \vec{r}'')\delta(t' - t''). \end{aligned} \quad (2.18)$$

In Eq. (2.17), the $+$ sign corresponds to $T > T_c$ and the $-$ sign corresponds to $T < T_c$. For $T > T_c$, which corresponds to the heating period, the nonlinear term is not relevant.

We implemented an Euler-discretized version of Eq. (2.17) with an isotropic Laplacian on a square lattice of size $L \times L$ ($L = 512$). Periodic boundary conditions were imposed in both directions. The discretization mesh sizes in space and time were

$\Delta x = 1.0$ and $\Delta t = 0.02$, respectively. The initial condition consisted of small fluctuations about $\psi_0 = 0$, i.e., a critical quench. Finally, the thermal noise of strength ϵ is mimicked by uniformly-distributed random numbers between $[-A, A]$. The appropriate noise amplitude in our Langevin simulation is

$$A = \sqrt{\frac{3\epsilon}{(\Delta x)^d \Delta t}}. \quad (2.19)$$

The results reported here correspond to $\epsilon = 0.00042$, i.e., $A = 0.25$ for $\Delta x = 1.0$ and $\Delta t = 0.02$. In Fig. 2.16, we show evolution snapshots for the CHC system subjected to alternating cycles of cooling and heating.

The evolution of a two-scale structure is evident in the snapshot at $t = t_2 + 800$, corresponding to the end of the second quench. As in the Kawasaki-Ising model, the cooling-heating cycles produce multiple length scales (see snapshots in Fig. (2.17) for the third quench), and the corresponding correlation functions and structure factors no longer show dynamical scaling (see Fig. 2.18).

We obtain the predicted form of the structure factor as

$$S(\vec{k}, t) = S(\vec{k}, 0) e^{-2k^2 t} + \epsilon (1 - e^{-2k^2 t}). \quad (2.20)$$

The solid lines in Fig. 2.18 belongs to Eq. (2.20), have good agreement with their corresponding numerical data. In Fig. 2.19 we have shown the length scales at various stages of the cooling-heating cycle.

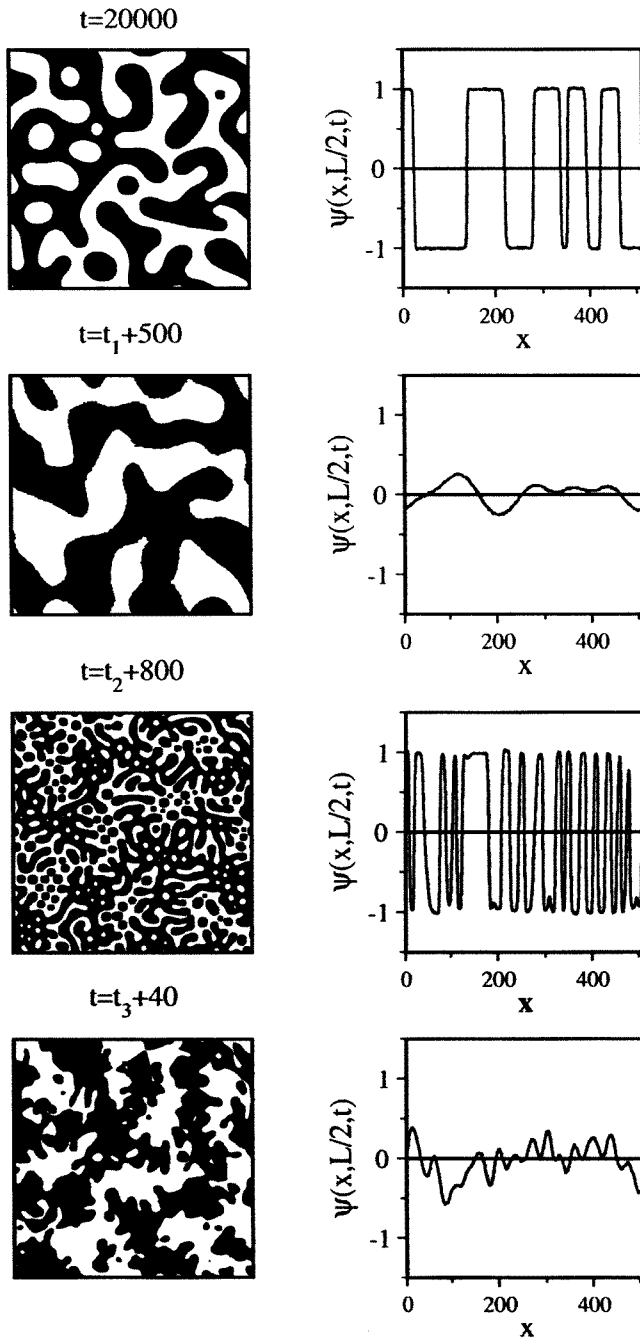
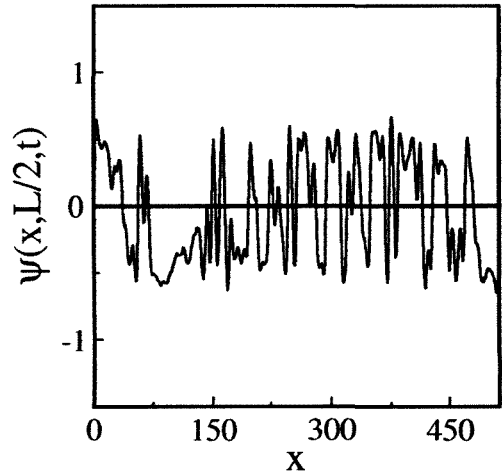
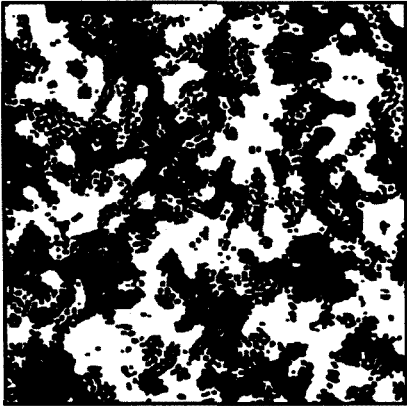


Figure 2.16: Evolution snapshots for the CHC system subjected to alternating cycles of cooling and heating. Regions with $\psi > 0$ (A-rich) and $\psi < 0$ (B-rich) are marked in black and white, respectively. To the left of each snapshot, we have shown the variation of the order parameter along a cross-section at $y = L/2$, where L is the system size.

$t=t_4+20$



$t=t_4+100$

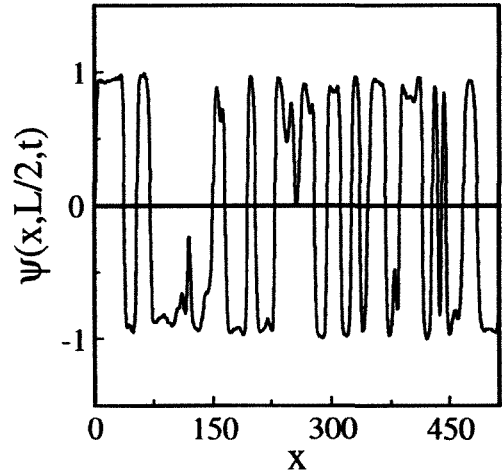
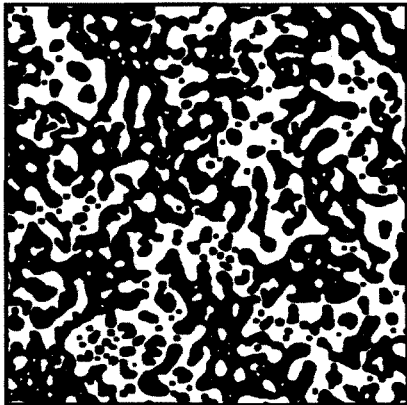


Figure 2.17: Evolution snapshots for the CHC system during the third quench.

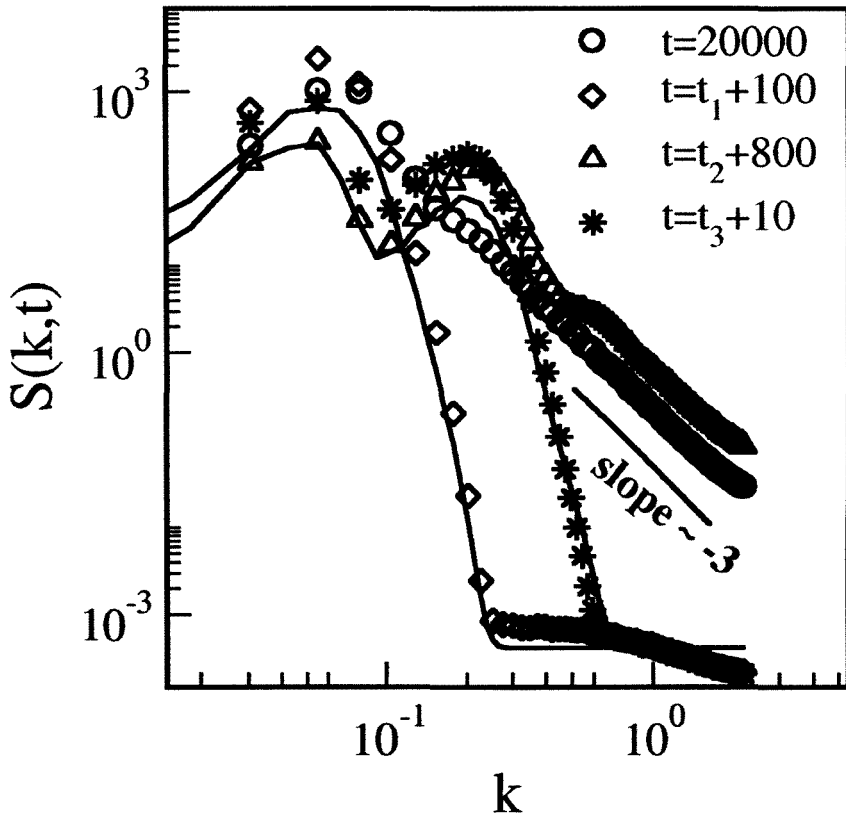


Figure 2.18: Structure factors at different stages of heating and cooling cycles. The symbols denote numerical data, and the solid lines denote the analytical fit to the structure factor [Eq. (2.20)] during heating.

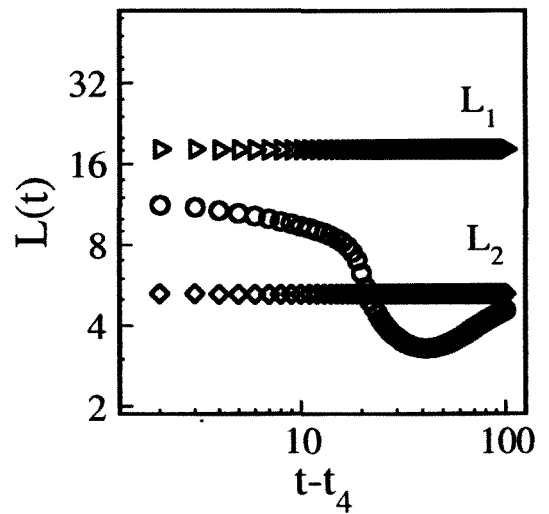
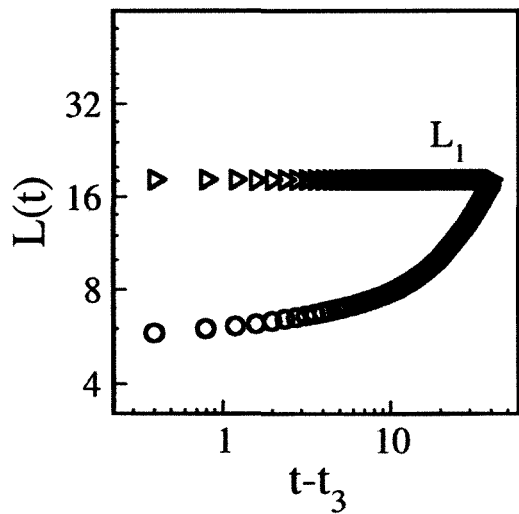
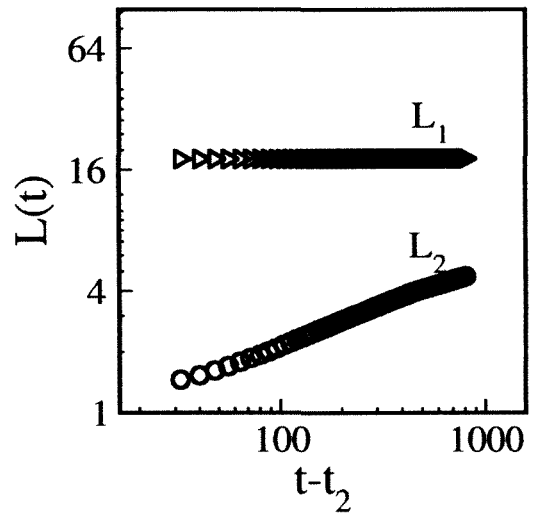
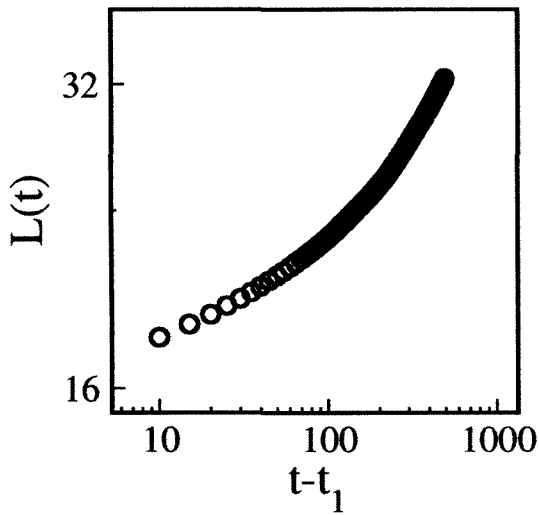


Figure 2.19: Time-dependence of domain sizes during various heating and cooling cycles.

2.4 Summary and Discussion

Let us conclude this chapter with a summary and discussion of our results. We have focused on the effect of time-dependent temperature protocols on the pattern dynamics of phase-separating systems. In general, we consider whether systems with arbitrary pre-defined structure factors can be created by an appropriate temperature protocol. This would be of great interest in various technological applications. In this chapter, we study the effect of alternate cycles of cooling (i.e., evolution of the system at $T < T_c$) and heating (i.e., evolution of the system at $T = \infty$). The system segregates during the cooling phase, and melts (undergoes disordering) during the heating phase. These cycles enable us to create systems with multiple length scales. The corresponding structure factors have multiple peaks, in contrast to the usual single-peak structure factors one sees in phase-separating systems.

We have gained a good understanding of the morphological evolution during these cooling and heating cycles. During heating, the structure factor can be obtained by convolution of the structure factor at the start of the cycle with an appropriate Gaussian function. Further, during a cooling cycle, the system is characterized by multiple length scales. Only one of these is time-dependent and it satisfies the Lifshitz-Slyozov growth law. We have also studied various other features of the morphologies which arise in this context.

Bibliography

- [1] S. Puri and V. K. Wadhawan (eds.), *Kinetics of Phase Transitions*, CRC Press, Boca Raton, Florida (2009).
- [2] K. Kawasaki, Phys. Rev. **145**, 224 (1966).
- [3] P. C. Hohenberg and B. I. Halperin, Rev. Mod. Phys. **49**, 435 (1977).
- [4] I. M. Lifshitz and V. V. Slyozov, J. Phys. Chem. Solids **19**, 35 (1961).
- [5] D. A. Huse, Phys. Rev. B **34**, 7845 (1986).
- [6] C. Yeung, Phys. Rev. Lett. **61**, 1135 (1988).
- [7] H. Furukawa, Phys. Rev. B **40**, 2341 (1989).
- [8] G. Porod, in *Small-Angle X-Ray Scattering*, O. Glatter and O. Kratky (eds.), Academic Press, New York (1982).
- [9] H. M. Vermeulen, Utrecht University, M.S. Thesis (2006).
- [10] M. E. J. Newman and G. T. Barkema, *Monte Carlo Methods in Statistical Physics*, Oxford University Press, Oxford (1999).

Chapter 3

Temperature-Dependence of Domain-Growth Kinetics

3.1 Introduction

In Sec. 1.1.2, we considered a ferromagnet at high temperatures $T > T_c$ (where T_c is the critical temperature) and zero magnetic field ($h = 0$). This system is in a disordered state with a random distribution of spins in the “up” or “down” states ($P_\uparrow = P_\downarrow = 1/2$). The disordered state becomes thermodynamically unstable when the system is rapidly quenched below the critical temperature ($T < T_c$), and convoluted domains of the ordered phases form in the early-time regime. These domains then grow with time so as to minimize the surface energy – the growth process is shown in Fig. 1.2. Typically, the coarsening of domains is characterized by a unique time-dependent length scale $L(t)$, where t is the time after the quench. For a ferromagnet without disorder, the growth process obeys the Allen-Cahn growth law, $L(t) \sim (t/\tau)^{1/2}$, where τ is the time-scale (see Sec. 1.4.2).

In this chapter, we focus on the dependence of τ on the quench temperature T .

As T is lowered, the surface tension σ between the up and down phases increases. Therefore, we expect faster growth at lower values of T . In this context, we present results from Monte Carlo (MC) simulations of the Ising model with Glauber spin-flip kinetics, introduced in Sec. 1.2.1. These results correspond to a range of values of T from $T \lesssim T_c$ to $T \ll T_c$. At relatively high values of T ($T \lesssim T_c$), we invoke the macroscopic concept of curvature of domain boundaries to understand the growth law and the behavior of $\tau(T)$. However, at low temperatures ($T \rightarrow 0$), the emerging domains are very pure, i.e., bulk fluctuations within the domains are negligible. Hence, a random-walk argument can explain the Allen-Cahn growth law and the behavior of $\tau(T)$. We also present some arguments which bridge the gap between these two levels of description.

This chapter is organized as follows. In Sec. 3.2, we present comprehensive MC results for domain growth at different temperatures. In Sec. 3.3, we discuss the relationship between the time-scale $\tau(T)$ and the surface tension $\sigma(T)$. In Sec. 3.4, we conclude this chapter with a summary and discussion.

3.2 Domain Growth at Different Quench Temperatures

We performed comprehensive MC simulations of the 2d-Ising model with spin-flip Glauber kinetics. A square lattice of size $L^2 = N$, with periodic boundary conditions in both directions, was used in the simulation. We denote the spin configuration for the lattice as $\{S_i\}$, where i corresponds to the lattice site. The initial condition for each run consists of a random mixture of up and down spins ($S_i = \pm 1$), corresponding to the paramagnetic state prior to the quench. At time $t = 0$, the system is quenched

to a temperature $T < T_c$. We consider the case with no magnetic field, i.e., $h = 0$.

The Ising Hamiltonian [cf. Eq. (1.2)] is

$$H = -J \sum_{\langle ij \rangle} S_i S_j, \quad (3.1)$$

where J is the strength of the exchange interaction, and $\langle ij \rangle$ denotes a sum over nearest-neighbor pairs. The appropriate microscopic kinetics for the evolution of a ferromagnet is Glauber spin-flip kinetics (see Sec. 1.2.1). We randomly choose a spin S_i and flip it to $-S_i$. The corresponding change of energy (which is same as the enthalpy for $h = 0$) is obtained as follows:

$$\begin{aligned} \delta H &= H_{\text{final}} - H_{\text{initial}} \\ &= 2JS_i \sum_{L_i} S_{L_i}, \end{aligned} \quad (3.2)$$

where L_i denotes the neighbors of i . The spin-flip is accepted with probability P [see Eq. (1.8)]:

$$P = \begin{cases} 1, & \text{if } \delta H < 0, \\ \exp(-\beta\delta H), & \text{if } \delta H > 0, \end{cases} \quad (3.3)$$

where $\beta = (k_B T)^{-1}$. Thus, spin flips which lower the energy are always accepted, and those which raise the energy are accepted with a Boltzmann factor. In Sec. 1.2.1, we had stressed that any transition probability which satisfies the *detailed-balance condition* will drive the system to the correct equilibrium state. The probability in Eq. (3.3) is frequently used in the MC literature [1, 2]. The elementary spin-flip move is repeated N times, which is equivalent to 1 Monte Carlo step (MCS).

In Fig. 1.2, we had shown the evolution snapshots for the Glauber-Ising model at $T = 0.5$. In Fig. 3.1, we show evolution snapshots for the Glauber-Ising model at different temperatures but at a fixed time ($t = 3000$ MCS). The up and down spins are marked black and white, respectively.

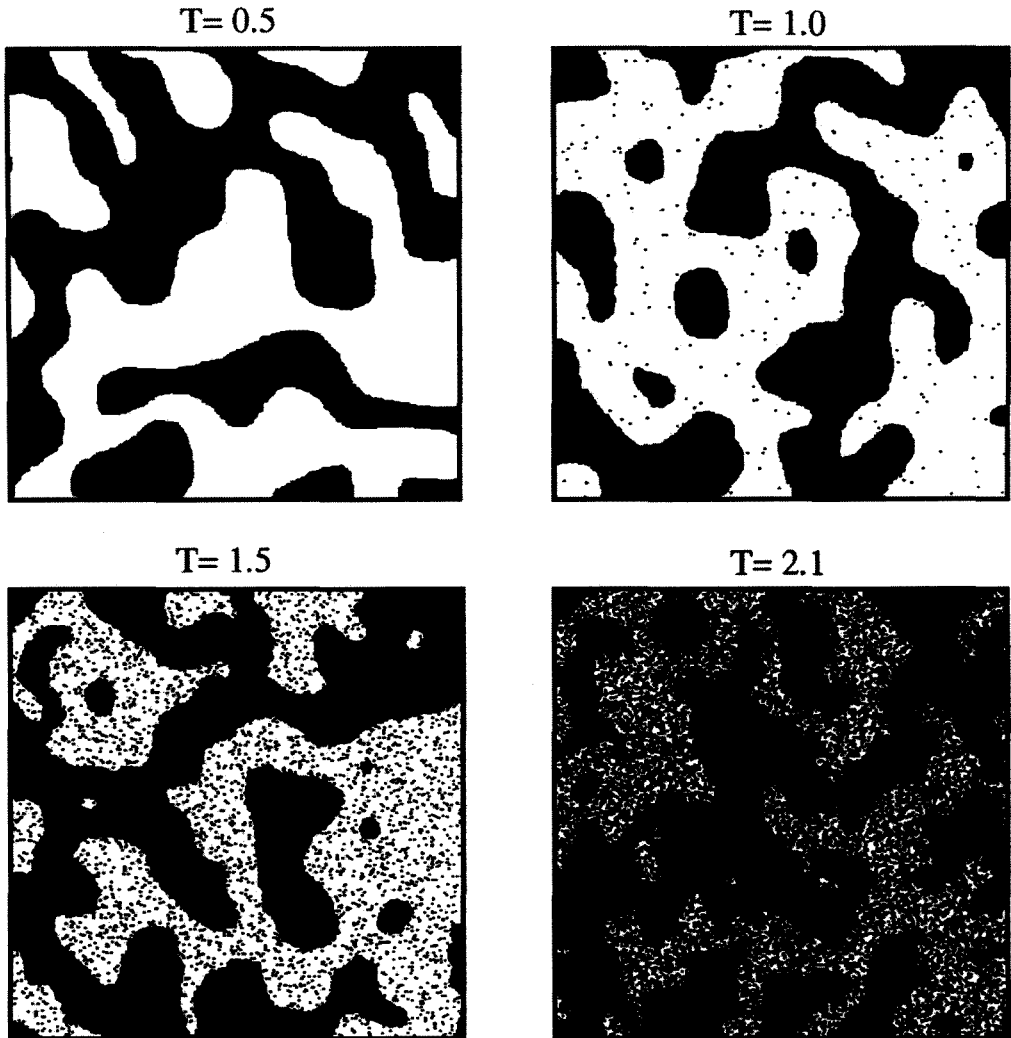


Figure 3.1: Evolution snapshots for the Glauber-Ising model at a fixed time ($t = 3000$ MCS), but different temperatures as indicated. The simulation has been done on a 4096^2 lattice with periodic boundary conditions. The up and down spins are marked black and white, respectively.

Note that $T_c \simeq 2.269$ (in units of J) for a $2-d$ Ising system. It is clear from Fig. 3.1 that systems at lower temperatures have purer domains and sharper interfaces than those at higher temperatures. Just below the critical temperature, the interfaces become very fuzzy due to the large fluctuations present in the system.

It can also be seen from Fig. 3.1 that the fastest growth of domains occurs at low temperatures. To quantify this, we calculate the spatial correlation function [cf. Eq. (1.54)]:

$$C(\vec{r}, t) = \frac{1}{N} \int d\vec{R} \left[\langle \psi(\vec{R}, t) \psi(\vec{R} + \vec{r}, t) \rangle - \langle \psi(\vec{R}, t) \rangle \langle \psi(\vec{R} + \vec{r}, t) \rangle \right], \quad (3.4)$$

and its Fourier transform, the structure factor $S(\vec{k}, t)$. In Fig. 1.6, we had demonstrated the dynamical scaling of these quantities for an ordering ferromagnet. Therefore, we do not show the scaling plots again here. Rather, we focus on the time-dependence of the domain size. The characteristic length scale of the domains can be defined in a variety of ways, e.g., the distance over which the spherically-averaged $C(r, t)$ decays to half its value at the origin:

$$C(L, t) = \frac{1}{2} C(0, t). \quad (3.5)$$

The length scale $L(t)$ obtained [using Eq. (3.5)] is shown for various temperatures in Fig. 3.2. These results were obtained from 4096^2 systems, as an average over 6 independent runs. This plot confirms the impression from Fig. 3.1, that the growth is faster for smaller T . In Fig. 3.3(a), we plot the data of Fig. 3.2(a) on a scaling plot. The data set for $T = 0.5$ has been taken as the reference data, and we rescaled the time-axis for other values of T by $\tau(T)$. This time-scale is determined by collapsing the maximum value of the length scale [$L(t = 5000)$] onto the reference data at

$T = 0.5$. The resultant data collapse demonstrates that the length scale only depends on the temperature through the time-scale $\tau(T)$. In Fig. 3.3(b), we plot the data from Fig. 3.3(a) on a log-log scale – all data sets are seen to obey the Allen-Cahn growth law asymptotically in time.

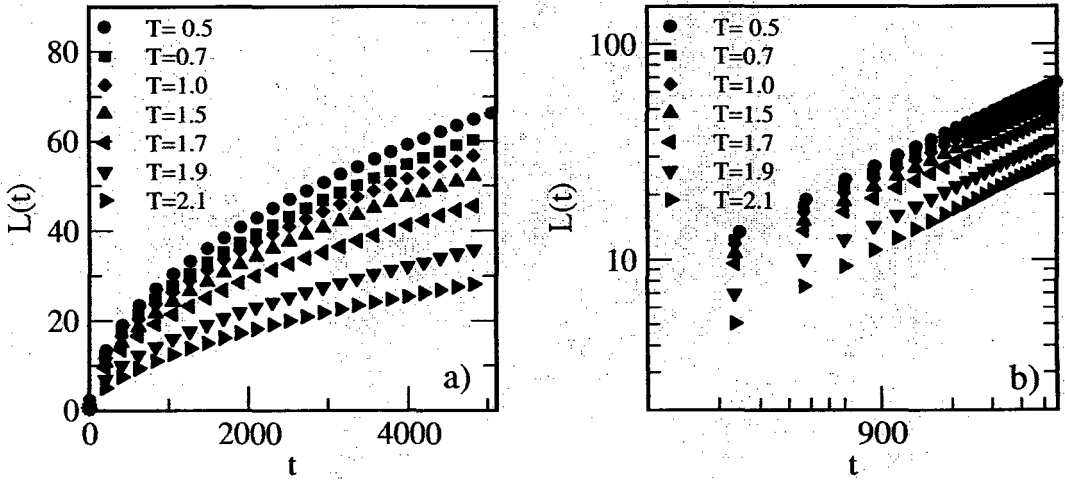


Figure 3.2: (a) Plot of $L(t)$ vs. t in the Glauber-Ising system at various temperatures. (b) Log-log plot of the data in (a).

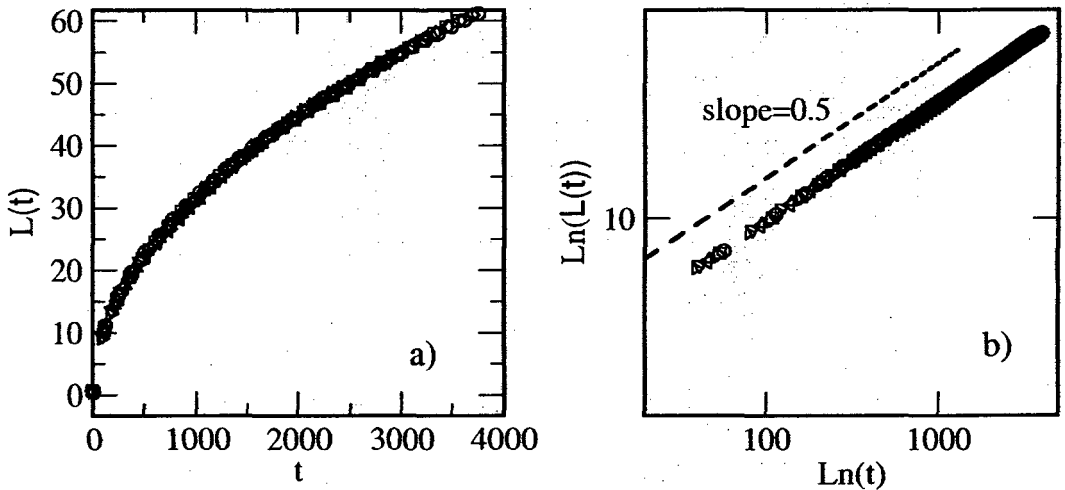


Figure 3.3: (a) Scaling plot of data sets in Fig. 3.2(a). The data for $T = 0.5$ has been chosen as the reference set. The time-scale $\tau(T)$ is determined by collapsing the length at the maximum time $L(4000, T)$ onto the reference set. (b) Log-log plot of scaled data sets in (a).

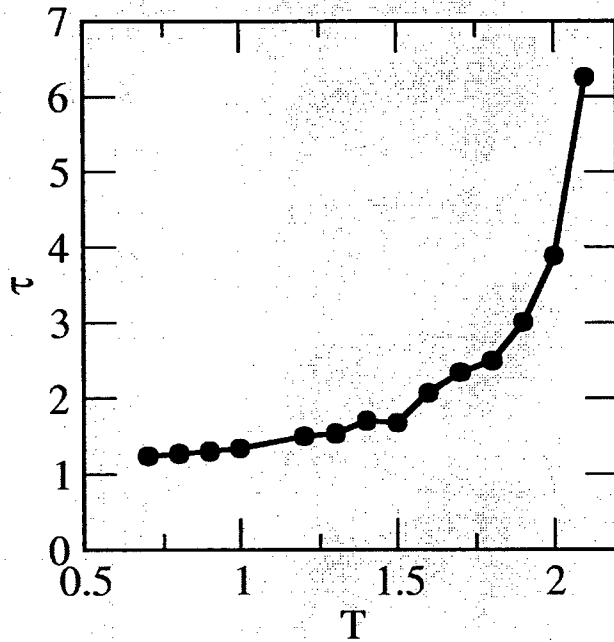


Figure 3.4: Plot of τ vs. T . Recall that $T_c \simeq 2.269$ for the 2- d Ising model.

As discussed earlier, we are interested in the T -dependence of τ . In Fig. 3.4, we plot τ vs. T for a range of quench temperatures $T \in [0, T_c]$. We see that τ is approximately constant for low values of T . This quantity starts to increase at $T \simeq 1$, and diverges as $T \rightarrow T_c^-$.

3.3 Time-Scales and Surface Energy

In this section, we would like to relate the time-scale $\tau(T)$ to the surface energy $\sigma(T)$. It is apparent from Fig. 3.4 that $\tau(T)$ is constant at low temperatures and diverges at high temperatures. The surface tension $\sigma(T)$ originates due to the presence of domain walls or kinks which cost extra energy, and the system evolves in a direction which minimizes the curvature of domains. However, at low temperatures, the domains are very pure and the corresponding kinks are sharp. This ensures near-constant values of $\sigma(T) \simeq J$ at low temperatures. At higher temperatures, fluctuations build up

in the domains, and the interfaces become more ragged and diffused. This reduces the surface tension, which approaches 0 as $T \rightarrow T_c^-$. As domain growth is driven by surface tension, it is reasonable to assume that $\tau \sim \sigma^{-1}$. We will demonstrate this shortly. However, we would like to stress that this simple relation connects a far-from-equilibrium time-scale (τ) with an equilibrium property (σ).

3.3.1 Domain Growth at Low Temperatures

The phase ordering system evolves towards a final equilibrium state by going through a number of intermediate configurations. Thus, the evolution of the system from one configuration to another can be thought of as paths in state space, and the probability of a particular path is associated with the statistical weight of the configuration state (importance sampling). Then the conditions of ergodicity and detailed balance are sufficient to ensure that the equilibrium distribution of states sampled by the dynamics is the correct Boltzmann distribution. Thus, at low temperatures, moves with lowest-energy barriers are accepted. However, at high temperatures, moves which raise the energy should also be accounted for with the right Boltzmann factor. Therefore, the evolution dynamics is equivalent to a diffusion process in a high-dimensional configuration space with a complex energy landscape.

We consider a $2-d$ Ising system with no external field. The system is quenched from a homogeneous initial state to below the critical temperature $T < T_c$. The system starts ordering locally, and soon develops a number of up and down domains competing with each other to grow. As time goes on, the number of domains decreases due to growth in size of the domains. Let us consider shrinking of a single square domain of side L [3, 4] (see Fig. 3.5). When the temperature is low, $\beta J \gg 1$, the only allowed spin flips are those that do not increase the total energy. The energy

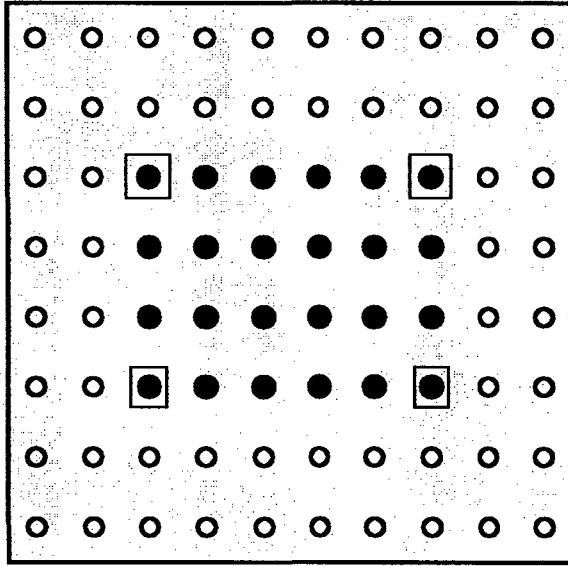


Figure 3.5: Schematic of an interface between up spins (white circles) and down spins (black circles). At sufficiently low temperatures, only the corner spin can flip. One such move is equivalent to moving the kink left or right. Also note that flipping the marked circles at the corners will cost zero energy, only such flips are allowed at low temperatures.

cost to flip a spin inside a domain is $8J$. On the boundary, the cost is $4J$, while the energy cost at the corner is 0. Thus, annealing of the domains can begin from the two corners of the square, and it continues along the edge of the square. This sequence of flips corresponds to a random walk of the corner along the edge, each step of which has no extra energy cost. The relevant first-passage probability of covering a distance L in t steps is given by [5]

$$P(L, t) = 1 - \frac{2}{2L - 1} \sum_{k=0}^{L-1} \frac{\cos^2 \phi_k}{\sin \phi_k} \{1 - [q + 2p \cos(2\phi_k)]^t\}, \quad (3.6)$$

where $\phi_k = \pi(2k + 1)/4L - 2$. The first-passage time is obtained by setting $P(L, t)$ to a fixed value. This yields the Allen-Cahn behavior $t \sim L^2$ [4].

The above mentioned random-walk argument provides an alternate interpretation of curvature-driven growth at low temperatures. We note that, since there is no

energy cost in the process (corner performing random walk on an edge), this model can also describe coarsening at $T = 0$.

3.3.2 Domain Growth at High Temperatures

However, at high temperatures ($T \gtrsim 1$), fluctuations destroy flat interfaces, and the above picture does not apply directly. An important work which classifies domain growth laws in nonconserved system is due to Lai, Mazenko and Valls (LMV) [6]. LMV proposed four classes of systems, determined by the length-scale-dependence of the energy barrier to coarsening. The growth of domains driven by curvature motion can be written as a generalization of the Allen-Cahn equation in Sec. 1.4.2:

$$\frac{dL}{dt} = \frac{a(L, T)}{L}, \quad (3.7)$$

where the function $a(L, t)$ is the diffusion coefficient, which (in general) depends on the length scale and temperature. The LMV classification can be stated in terms of the behavior of $a(L, t)$.

(a) In *Class 1* systems, $a(L, t)$ is independent of L and remains nonzero as $T \rightarrow 0$.

The relaxation mechanism follows the path with no energy barrier, and the nature of relaxation does not depend on the coarsening length scale. The Ising model discussed above belongs to this class. For Class 1 systems, the behavior of the length scale is $L(t) \sim t^{1/2}$.

(b) In *Class 2* systems, the minimum energy barriers are independent of L , but the elementary diffusion process encounters an energy barrier E_B , such that $a(L, t) = a_0 \exp(-E_B/T)$. We again recover the $t^{1/2}$ -growth law but with a time scale $\tau = \tau_0 \exp(E_B/T)$. This implies that the length scale will be constant at

early times $t \ll \tau$, and at later stages the growth will be $L(t) \sim (t/\tau)^{1/2}$.

- (c) In *Class 3* systems, the activation energy E_B grows linearly with L . For instance, a system with quenched impurities can trap the domain walls with a fixed energy per unit length. In this case, we have the short-time growth law $L(t) \sim t^{1/2}$, which crosses over to a logarithmic growth law at late times, $L(t) \sim T\epsilon^{-1} \ln(t/\tau)$. Here, $\tau = L_c T / (a_0 \epsilon)$, ϵ being the disorder amplitude and L_c is the crossover length scale.
- (d) In *Class 4* systems, the energy barriers grow as $E_B \sim L^m$, where $m \neq 1$. Again, the short-time growth law is $L(t) \sim t^{1/2}$, and it crosses over to a logarithmic growth law, $L(t) \sim (T\epsilon^{-1})^{1/m} [\ln(t/\tau)]^{1/m}$. Here, $\tau = L_c^{2-m} T / (m a_0 \epsilon)$, with L_c being the crossover length scale.

In Chapter 4, we will discuss domain growth in systems with quenched disorder [7, 8, 9]. In this context, we encounter both Class 3 and Class 4 systems. Our simple system in this chapter, the Glauber-Ising model, belongs to *Class 1* with $a(L, t) = \sigma(T)$. Thus, at higher T , we expect $\tau \sim \sigma^{-1}$. We have already obtained τ as a function of T (see Fig. 3.4). Let us next obtain $\sigma(T)$ from our MC simulations. We consider a square lattice with dimension $L_x \gg L_y$, and set up an initial spin configuration as

$$S(x, y, t = 0) = \begin{cases} +1 & \text{for } y > L_y/2, \\ -1 & \text{for } y < L_y/2. \end{cases} \quad (3.8)$$

Further, we set periodic boundary conditions in the x -direction, and flat boundary conditions [$S(x, 0, t) = S(x, 1, t)$ and $S(x, L_y + 1, t) = S(x, L_y, t)$] in the y -direction. This system was allowed to evolve at temperature T till it settled into an equilibrium

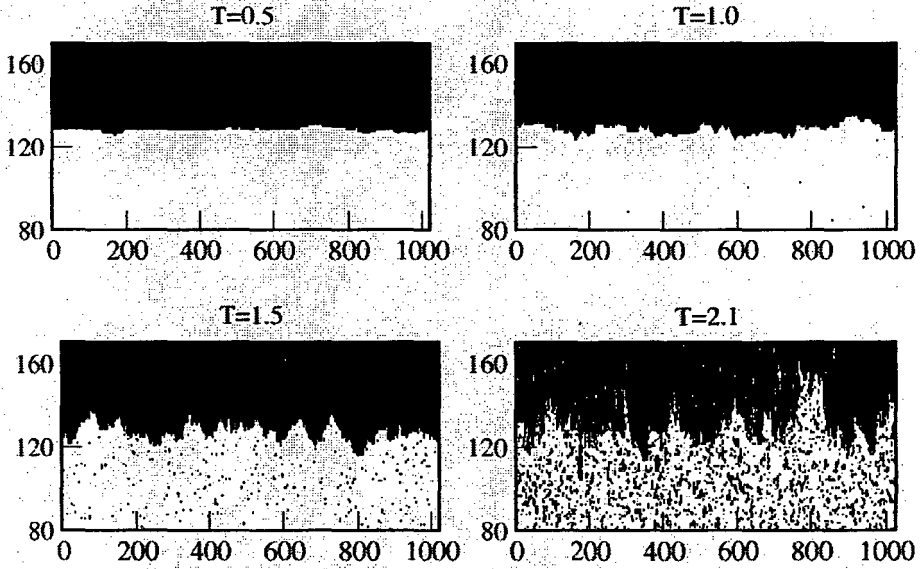


Figure 3.6: Equilibrium kink configuration (interface) between up and down domains at various temperatures. The interface becomes more ragged, and domains become more impure, at higher temperatures.

kink configuration, as shown in Fig. 3.6. Notice that the interface is almost flat at low temperatures, and becomes more ragged at high temperatures. The scale of raggedness is the correlation length $\xi(T)$, which diverges as $T \rightarrow T_c^-$. The precise shape of the kink profile [$\psi(y)$ vs. y] was obtained by averaging $S(x, y)$ (for a system size $L_x = 4096$, $L_y = 256$) along the x -direction for 100 independent runs. The kink profiles at different values of T are shown in Fig. 3.7. We expect the kink profile to have the functional form [see Eq.(1.48)]:

$$\psi(y) = m_0(T) f\left(\frac{y}{\xi(T)}\right), \quad (3.9)$$

where $m_0(T)$ and $\xi(T)$ are the equilibrium magnetization and correlation length, respectively. We define the correlation length as the distance over which the kink profile goes from $\psi = -m_0/2$ to $\psi = +m_0/2$.

In Fig. 3.8(a), we plot $\xi(T)$ vs. T [see Table 3.1]. The correlation length diverges as $T \rightarrow T_c^-$. In Fig. 3.8(b), we plot ξ vs. $(T_c - T)$ on a log-log scale. We expect a power-law divergence of the correlation length, $\xi \sim (T_c - T)^\nu$ as $T \rightarrow T_c^-$. The Onsager solution [10] for the 2- d Ising model yields $\nu = 1$, which is shown as a solid line in Fig. 3.8(b).

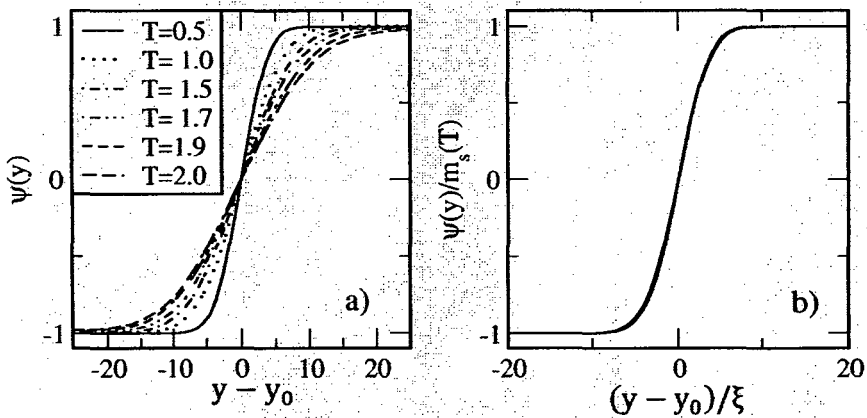


Figure 3.7: (a) Plot of kink profiles at different temperatures. The kink center (where $\psi = 0$) is denoted as y_0 . At low temperatures, the interface is sharp and, with increase of temperatures it becomes more gradual. (b) Scaling plot of the data in (a), $\psi(y)/m_0$ vs. $(y - y_0)/\xi$.

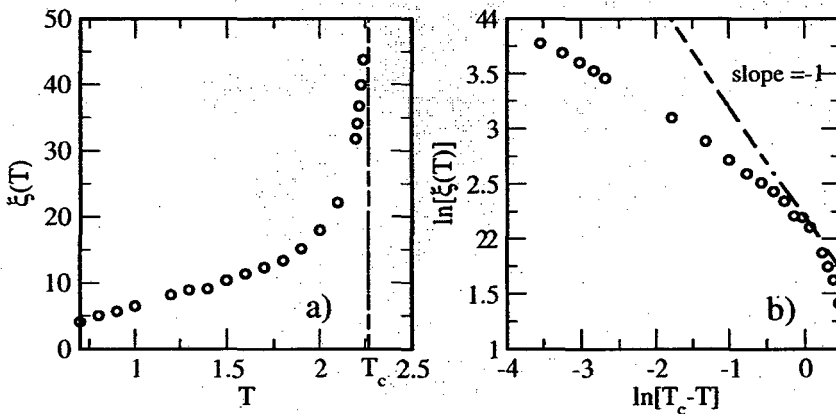


Figure 3.8: (a) Plot of correlation length (ξ) vs. temperature (T). The correlation length is defined as the length between the points at which $\psi = -m_0/2$ and $\psi = +m_0/2$. (b) Log-log plot of ξ vs. $T_c - T$.

Table 3.1: Correlation length and saturation magnetization at different values of T .

Temperature (T)	Position of kink (y_0)	Correlation length $\xi(T)$	$m_0(T)$
0.7	128.65426	4.10420	0.999976
0.8	128.60151	5.05950	0.999909
0.9	128.49491	5.71410	0.999694
1.0	128.40762	6.47847	0.999216
1.2	128.33987	8.16590	0.996889
1.3	128.31241	8.94610	0.994544
1.4	128.35477	9.08790	0.991163
1.5	128.01894	10.38180	0.986115
1.6	128.56332	11.38015	0.979301
1.7	128.03657	12.29777	0.969809
1.8	128.40540	13.38167	0.956519
1.9	128.64081	15.14047	0.937541
2.0	128.89470	17.90983	0.910363
2.1	128.32745	22.14836	0.867483
2.2	256.20255	31.76820	0.781815
2.21	256.29514	34.0830	0.769654
2.22	256.80670	36.69290	0.752233
2.23	256.16160	39.93000	0.733770
2.24	256.35671	43.74880	0.703299

In Fig. 3.9, we plot the saturation magnetization $m_0(T)$ vs. T [see Table 3.1].

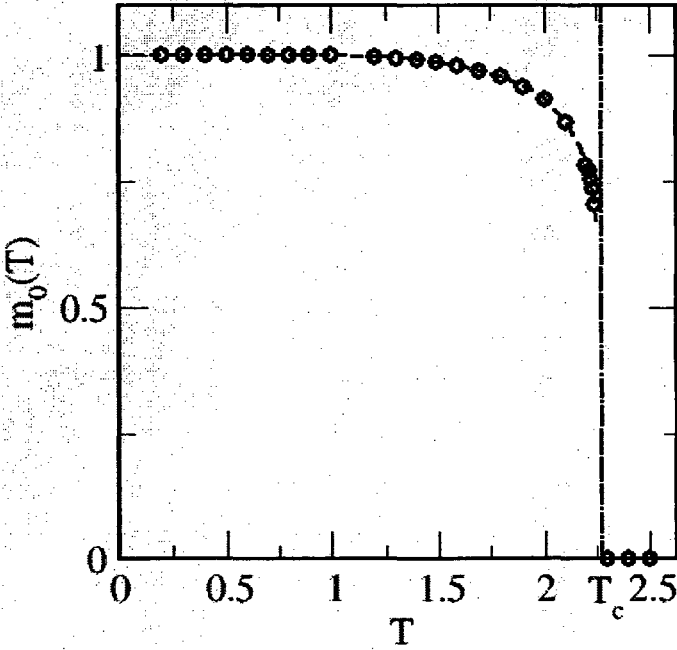


Figure 3.9: Plot of saturation magnetization m_0 vs. temperature T .

The Onsager solution for this quantity is

$$m_0(T) = \begin{cases} [1 - \sinh^{-4}(2/T)]^{1/8} & \text{for } T \leq T_c, \\ 0 & \text{for } T > T_c. \end{cases} \quad (3.10)$$

The Onsager solution is denoted as a solid line in Fig. 3.9. The limiting behavior of $m_0(T)$ in various limits is as follows:

$$\begin{aligned} m_0(T) &\simeq 1 - 2 \exp(-8/T) && \text{for } T \rightarrow 0, \\ &\simeq 1.2224 \left(1 - \frac{T}{T_c}\right)^{1/8} && \text{for } T \rightarrow T_c^-. \end{aligned} \quad (3.11)$$

In the following subsection, we will estimate the surface tension using these values of m_0 and ξ .

3.3.3 Estimating the Surface Tension

To estimate the surface tension, consider the deterministic version of the TDGL equation (1.39):

$$\frac{\partial}{\partial t}\psi(\vec{r}, t) = -\Gamma \frac{\delta G[\psi]}{\delta \psi}, \quad (3.12)$$

where

$$G[\psi] = \int d\vec{r} \left[g(\psi) + \frac{K}{2} (\vec{\nabla}\psi)^2 \right]. \quad (3.13)$$

Let us consider the case with $h = 0$. Equation (3.12) has a static kink solution [cf. Eq. (3.9)]:

$$\psi_s(z) = m_0 f\left(\frac{z}{\xi}\right), \quad (3.14)$$

where $f(x)$ is a sigmoidal function with $f(\pm\infty) = \pm 1$. The kink solution satisfies the Lagrange equation:

$$-g'(\psi) + K \frac{d^2\psi}{dz^2} = 0. \quad (3.15)$$

The free energy associated with the kink solution is

$$G_s = \int_{-\infty}^{+\infty} dz \left[g(\psi_s) + \frac{K}{2} \left(\frac{d\psi_s}{dz} \right)^2 \right]. \quad (3.16)$$

The corresponding free energy associated with the homogeneous (bulk) solution $\pm m_0$ is

$$G_0 = \int_{-\infty}^{+\infty} dz g(m_0). \quad (3.17)$$

The difference in free energy due to the kink solution is

$$\Delta G = G_s - G_0 = \int_{-\infty}^{+\infty} dz \left[g(\psi_s) - g(m_0) + \frac{K}{2} \left(\frac{d\psi_s}{dz} \right)^2 \right]. \quad (3.18)$$

If we multiply Eq. (3.15) by $d\psi/dz$, we obtain

$$\frac{d}{dz} \left[-g(\psi) + \frac{K}{2} \left(\frac{d\psi}{dz} \right)^2 \right] = 0, \quad (3.19)$$

This can be integrated to obtain

$$\frac{K}{2} \left(\frac{d\psi}{dz} \right)^2 = g(\psi) - g(m_0). \quad (3.20)$$

Replacing this in Eq. (3.18), we obtain

$$\begin{aligned} \Delta G &= K \int_{-\infty}^{+\infty} dz \left(\frac{d\psi_s}{dz} \right)^2 \\ &= \frac{K m_0^2}{\xi} \int_{-\infty}^{+\infty} dx f'(x)^2. \end{aligned} \quad (3.21)$$

This yields an expression for the surface tension:

$$\sigma \sim \frac{m_0^2}{\xi}. \quad (3.22)$$

The data for surface tension [calculated using Eq. (3.22) and the values in Table 3.1]

Table 3.2: Data for surface tension and time-scale of domain growth.

Temperature (T)	$\tau(T)$	$\sigma = \frac{m_0^2}{\xi}$	Product ($\tau\sigma$)
0.7	1.2345	0.2436	0.3007
0.8	1.2687	0.1976	0.2507
0.9	1.2990	0.1749	0.2272
1.0	1.3393	0.1541	0.2064
1.2	1.4971	0.1217	0.1822
1.3	1.5337	0.1106	0.1696
1.4	1.7014	0.1081	0.1839
1.5	1.7710	0.0937	0.1668
1.6	2.0662	0.0843	0.1741
1.7	2.3400	0.0765	0.1790
1.8	2.4936	0.0684	0.1705
1.9	3.0092	0.0581	0.1747
2.0	3.8817	0.0463	0.1796
2.1	6.2533	0.0340	0.2125

is presented in Table 3.2. We also give values for the growth time-scale $\tau(T)$.

In Fig. 3.10(a) we plot $\sigma(T)$ vs. T – as expected, the surface tension approaches zero as $T \rightarrow T_c^-$. In Fig. 3.10(b), we plot $\sigma(T)$ vs. $(T_c - T)$ on a log-log plot. Finally, in Fig. 3.11 we plot $\sigma\tau$ vs. T (see Table 3.2). For $T \geq 1$, the plot is approximately flat, demonstrating that $\tau \sim \sigma^{-1}$. However, for $T \leq 1$, we see that $\tau \sim \text{constant}$ whereas σ increases with decreasing T . In this limit, domain growth is described better by the random-walk picture in Sec. 3.3.1.

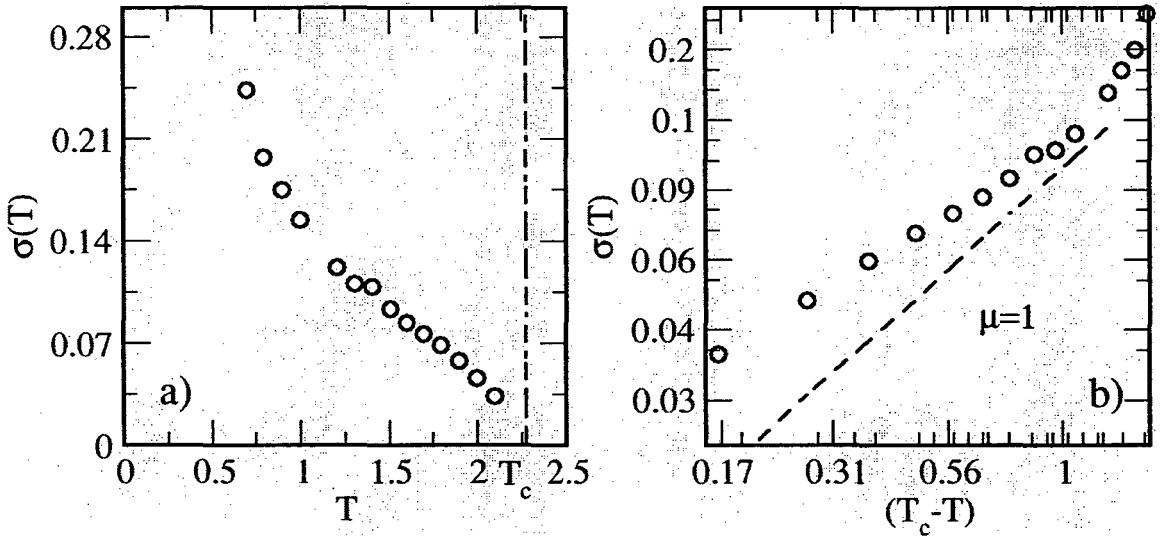


Figure 3.10: (a) Plot of surface tension σ vs. T for $T < T_c$. The vertical line is drawn at $T = T_c \simeq 2.269$. (b) Plot of σ vs. $(T_c - T)$ on a log-log scale. The line with slope 1 denotes the theoretical prediction, $\sigma \sim (T_c - T)^\mu$ as $T \rightarrow T_c^-$ with $\mu = 1$.

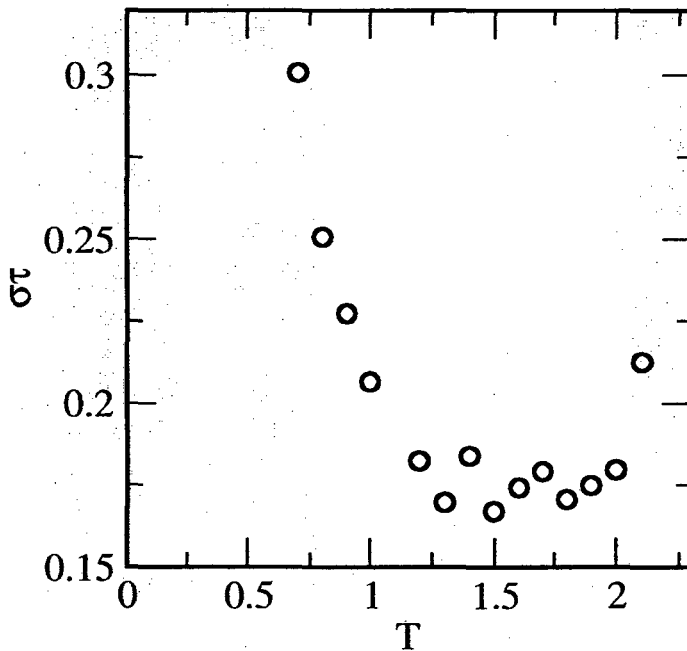


Figure 3.11: Plot of $\sigma\tau$ vs. T .

3.4 Summary and Discussion

Let us conclude this chapter with a brief summary and discussion of our results. We have undertaken a comprehensive MC simulation of $2-d$ Ising systems with non-conserved dynamics. When quenched below the critical temperature T_c , the system evolves to its new equilibrium state via the emergence and growth of domains.

In this chapter, we have studied domain growth in the Glauber-Ising model at different temperatures (see Sec. 3.3.1 and Sec. 3.3.2). The Allen-Cahn growth law $L(t) \sim (t/\tau)^{1/2}$ is obeyed at all temperatures – however, the time-scale τ is strongly dependent upon the quench temperature. This growth law can be explained via a curvature-reduction mechanism at high temperatures. However, at low temperatures, we invoke a picture where domain growth is driven by the random walk of domain corners along flat interfaces. This picture is not valid at large T -values as impurities in pure domains appear in the form of spin fluctuations, as shown in Fig. 3.12.

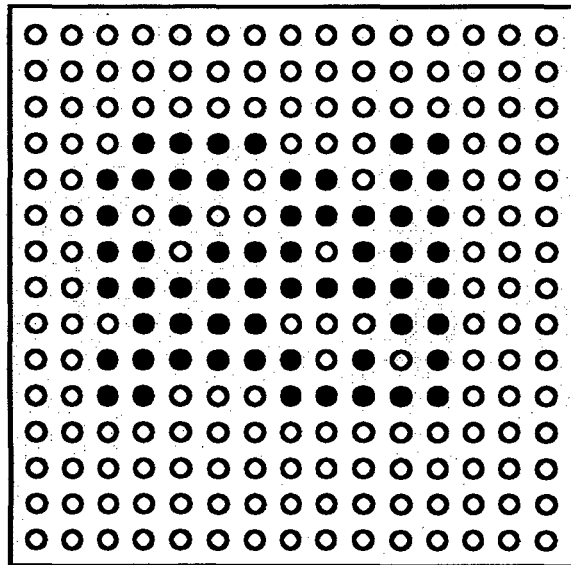


Figure 3.12: A typical domain snapshot at an intermediate quench temperature. The up spins and down spins are denoted as white and black, respectively. The pure domains develop impurities in the form of spin fluctuations.

Our goal is to develop a random-walk scenario of domain growth, which is valid at all temperatures. This would provide a microscopic basis for the definition of curvature, and bridge the gap between the usual *random-walk picture* (valid at low T) and the *curvature-reduction picture* (valid at high T). The appropriate random-walk description at high T involves interacting random walkers which move on domain edges. Their dynamics is modeled as the interaction of kinks and anti-kinks. When two kinks or anti-kinks collide, we have interacting random walkers with reflection. Alternatively, the collision of a kink and anti-kink can be interpreted as an absorption process. We are presently developing this model, and detailed results will be presented shortly.

Bibliography

- [1] K. Binder and D. W. Heermann, *Monte Carlo Simulation in Statistical Physics*, Springer Series in Solid-State Sciences Vol. 80, Springer-Verlag, Heidelberg (2002).
- [2] M. E. J. Newman and G. T. Barkema, *Monte Carlo Methods in Statistical Physics* Oxford University Press, Oxford (1999).
- [3] J. D. Shore and J. P. Sethna, Phys. Rev. B **43**, 3782 (1991); Phys. Rev. B **46**, 11376 (1992).
- [4] K. Tafa, S. Puri and D. Kumar, Phys.Rev. E **63**, 046115 (2001).
- [5] W. Feller, *Introduction to Probability Theory and its Applications*, Wiley, New York (1968).
- [6] Z. W. Lai, G. F. Mazenko and O. T. Valls, Phys. Rev. B **37**, 9481 (1988).
- [7] D. A. Huse and C. L. Henley, Phys. Rev. Lett. **54**, 2708 (1985).
- [8] S. Puri, D. Chowdhury and N. Parekh, J. Phys. A **24**, L1087 (1991); S. Puri and N. Parekh **25**, 4127 (1992).
- [9] R. Paul, S. Puri and H. Rieger, Europhys. Lett. **68**, 881 (2004); Phys. Rev. E **71**, 061109 (2005).

- [10] R. K. Pathria, *Statistical Mechanics* 2nd Edition, Butterworth-Heinemann (1996).

Chapter 4

Aging in Ferromagnets with Quenched Disorder

4.1 Introduction

The evolution of a multi-phase system, which is quenched to the ordered phase is characterized by the emergence and growth of domains. The domain scale grows with time as $L(t) \sim t^{1/2}$ for the case with Glauber (or nonconserved) dynamics, and as $L(t) \sim t^{1/3}$ for the case with Kawasaki (or conserved) dynamics (see Chapter 1). A key concept in this regard is that many time-dependent properties of coarsening systems can be understood in terms of a simple scaling picture [1]. In the previous chapters, we have focused on the morphologies and growth laws which characterize phase ordering systems. These features have been traditionally well-studied in the literature. Recently, motivated by spin glass theory, many studies have also been devoted to understanding slow relaxation and aging phenomena in domain growth problems [1, 2]. In this chapter, we focus on aging phenomena in the ordering dynamics of ferromagnets with quenched disorder.

Consider a paramagnet \rightarrow ferromagnet transition, as was discussed in Chapter 1. The phase diagram of a magnet in the temperature (T) and magnetic field (h) plane is shown in Fig. 1.1. At high temperatures ($T > T_c$) and zero magnetic field ($h = 0$), the spins are randomly oriented, and the resulting magnetization is zero. Below the critical temperature ($T < T_c$), the system prefers to be in a spontaneously magnetized state, even if there is no magnetic field. In domain growth problems, we study the evolution of a system, which is rapidly quenched from $T > T_c$ to $T < T_c$.

For simplicity, consider a system which is initially at infinite temperature ($T_I = \infty$), with correlation length $\xi_I = 0$. There are three possible classes of quenches:

- (a) Quenches to $T > T_c$ with correlation length $0 < \xi < \infty$;
- (b) Quenches to $T = T_c$ with $\xi = \infty$ (for an infinite system);
- (c) Quenches to $T < T_c$ with $\xi = \infty$ (for an infinite system).

Thus, the correlation length grows from $\xi_I = 0$ to a final value $\xi > 0$. For quenches to $T > T_c$, there is a finite equilibration time. On the other hand, for quenches to $T < T_c$, the system is always nonequilibrium as $\xi(t) \sim t^{1/z}$, z being the dynamical exponent. This fact is responsible for slow relaxation and aging in quenches to or below T_c . Aging usually means that older systems relax slower and younger ones faster [3]. Aging is generally described by two-time observables, such as the *order-parameter autocorrelation function* $C(t, t_w)$ and the *auto-response function* $R(t, t_w)$. (These quantities will be defined at the appropriate place.) The shortest time after the quench ($t_w \geq 0$) and the longest time ($t \geq t_w$) are conventionally called the *waiting time* and the *observation time*, respectively. Thus, the value of t_w sets the age of the system.

This chapter is organized as follows. In Sec. 4.2, we discuss domain growth in systems with quenched disorder. In Sec. 4.3, we present detailed numerical results for ordering dynamics in disordered systems. We will present results for the relevant

morphological features and the aging properties. Finally, we conclude this chapter with a summary and discussion in Sec. 4.4.

4.2 Domain Growth in Disordered Systems

Consider the two-state Ising model with quenched bond disorder, i.e., the *random-bond Ising model* (RBIM). The associated Hamiltonian is given by

$$H = - \sum_{\langle ij \rangle} J_{ij} S_i S_j, \quad S_i = \pm 1, \quad (4.1)$$

where the exchange couplings J_{ij} are quenched random variables. Here, we will study the case where the bonds are always ferromagnetic, $J_{ij} > 0$. They are uniformly distributed in the interval $[1 - \epsilon, 1 + \epsilon]$, where $0 \leq \epsilon \leq 1$. This model shows a second-order phase transition at a critical temperature $T_c(\epsilon) > 0$. Note that the critical temperature $T_c(\epsilon) \simeq T_c(0) \simeq 2.269$ and it does not depend strongly upon the disorder amplitude.

We associate Glauber spin-flip dynamics with the RBIM, starting from a homogeneous initial configuration. For $T < T_c(\epsilon)$, ordered domains form and the system evolves with a characteristic length scale $L(t)$. In Fig. 4.1, we show evolution pictures for the 2- d Glauber-RBIM after a quench from $T = \infty$ to $T = 1.0$. The snapshots correspond to different disorder amplitudes – $\epsilon = 0$ (pure case) and $\epsilon = 1$ (case with maximum disorder). It is clear from the snapshots in Fig. 4.1 that the evolution is slower for higher amplitudes of disorder. This will be quantified via the corresponding domain growth laws, and the scaling form of the correlation function and structure factor.

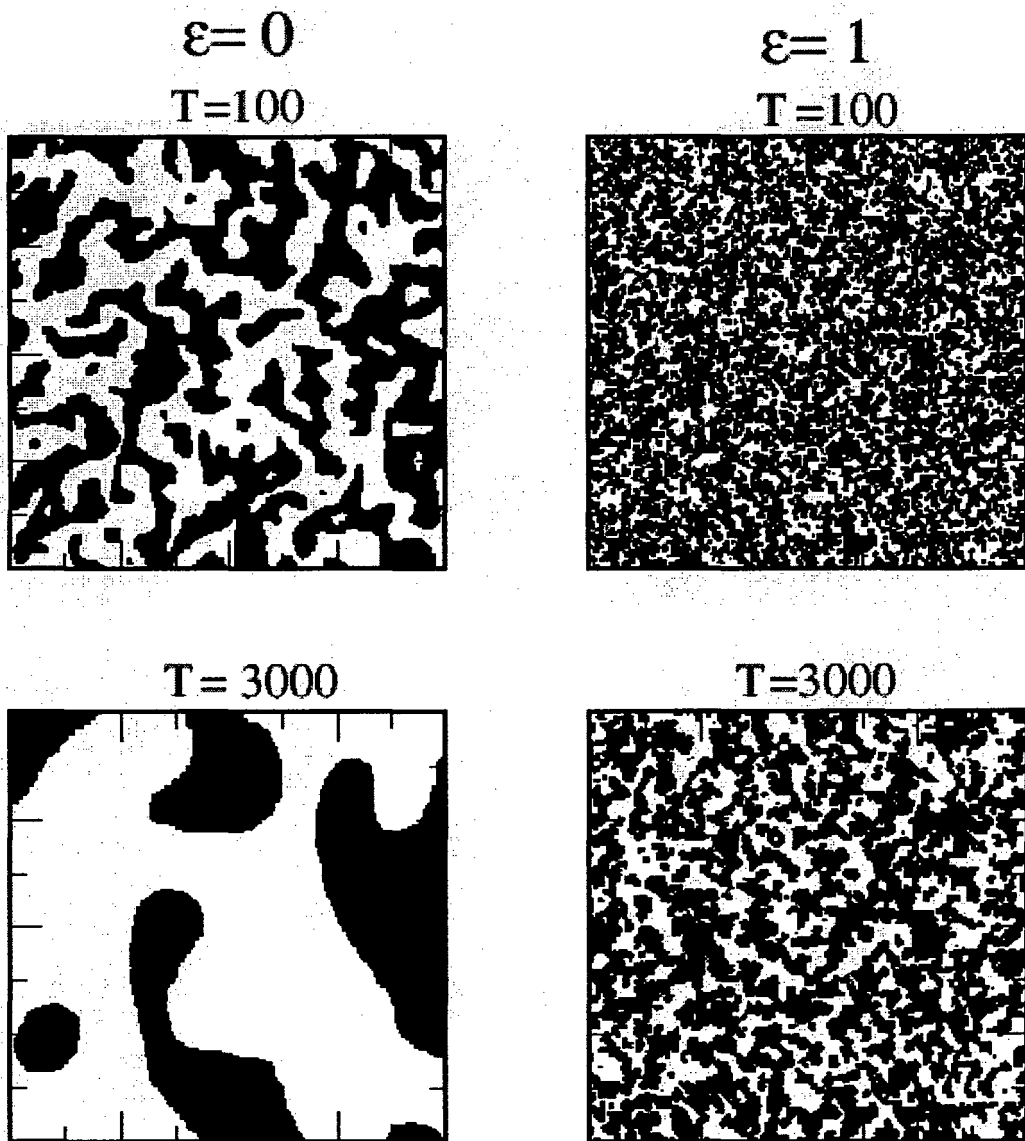


Figure 4.1: Evolution snapshots of a spin-1/2 ferromagnet with quenched disorder, evolving from a random initial configuration. These snapshots are obtained from a Monte Carlo (MC) simulation of the RBIM with spin-flip Glauber kinetics (see Sec. 1.2). The system size is 4096^2 , and periodic boundary conditions are applied in both directions. The quench temperature is $T = 0.5$. Time is measured in units of Monte Carlo steps (MCS). The black regions denote up spins and white regions denote down spins. The snapshots on the left correspond to $\epsilon = 0$ (pure case), and the snapshots on the right correspond to $\epsilon = 1$ (case with maximum disorder).

There is a good understanding of the growth laws for pure and isotropic systems with nonconserved order parameter – we have seen that the ordering system obeys the Allen-Cahn growth law, $L(t) \sim t^{1/2}$ (see Sec. 1.4.2). However, the presence of disorder in the system traps the domain boundaries, resulting in slower domain growth. In Sec. 3.3.2, we had discussed the Lai-Mazenko-Valls (LMV) [4] classification of domain growth laws in nonconserved systems. Recall that the growth of domains driven by a curvature-reduction mechanism can be written as [cf. Eq. (3.7)]

$$\frac{dL}{dt} = \frac{a(L, T)}{L}. \quad (4.2)$$

Here, $a(L, T)$ is a diffusion constant and it depends upon the domain length scale $L(t)$ and the quench temperature. In pure systems, the diffusion constant is independent of the length scale, i.e., $a(L, T) = a_0$, and the corresponding growth law can be written as $L(t) \sim (a_0 t)^{1/2}$.

Let us next consider systems with quenched disorder ($J_{ij} > 0$). It is known that length scales are small at early times, and the growth of domains is not affected by disorder, i.e., the growth law is the same as that for the pure case at early times. However, at late times, the domains are trapped by disorder sites which create a barrier $E_B(L)$ to domain growth. Thus, in the late-stage dynamics, thermal activation over the disorder barriers plays a crucial role during domain growth. The diffusion constant $a(L, T)$ is related to the energy barrier E_B as

$$a(L, T) \simeq a_0 \exp(-\beta E_B), \quad (4.3)$$

where $\beta = T^{-1}$ ($k_B = 1$). Equation (4.3) can now be used to understand domain growth laws with disorder, when the form of $E_B(L)$ is known. Huse and Henley (HH)

argued that the coarsening domains are trapped by energy barriers $E_B(L) \simeq \epsilon L^\psi$, where ϵ is the disorder amplitude and the exponent $\psi = 1/4$ [5]. As a consequence, the late-time behavior of $L(t)$ is

$$L(t) \simeq \left[\frac{T}{\epsilon} \ln \left(\frac{t}{t_0} \right) \right]^{1/\psi}, \quad (4.4)$$

$$t_0 \simeq \frac{1}{a_0 \psi} \left(\frac{T}{\epsilon} \right)^{2/\psi}. \quad (4.5)$$

As the early-time dynamics is described by the Allen-Cahn growth law, we can reformulate the early-time and late-time behaviors as

$$R(t) = R_0(T, \epsilon) h \left(\frac{t}{t_0} \right), \quad (4.6)$$

where

$$R_0(T, \epsilon) = \left(\frac{T}{\epsilon} \right)^{1/\psi}, \quad (4.7)$$

and

$$h(x) = \begin{cases} \left(\frac{2}{\psi} x \right)^{1/2} & \text{if } x \ll 1, \\ (\ln x)^{1/\psi} & \text{if } x \gg 1. \end{cases} \quad (4.8)$$

In spite of several numerical simulations [6, 7, 8] and experiments [9, 10, 11], the HH growth law has not been satisfactory proved. In recent work, Paul et al. [14] used Monte Carlo (MC) simulations to argue for an algebraic dependence of $L(t)$ in the asymptotic time limit. Our MC results are also consistent with power-law domain growth with exponents which depend upon the disorder amplitude and temperature. These exponents can be understood in the framework of a logarithmic (rather than

power-law) L -dependence of the energy barriers E_B . In the context of the *dilute Ising model* (DIM), Henley [15] and Rammal and Benoit [16] have argued that the fractal nature of domain boundaries results in a logarithmic L -dependence of the energy barriers. Thus, the scaling form of the energy barriers is

$$E_B(L) \simeq \epsilon \ln(1 + L). \quad (4.9)$$

Equation (4.2) can then be written as [using Eq. (4.9)]

$$\frac{dL}{dt} = \frac{a_0}{L} (1 + L)^{\epsilon/T}. \quad (4.10)$$

The solution of Eq. (4.10) is

$$L(t) = \begin{cases} (2a_0t)^{1/2}, & t \ll t_0, \\ [(2 + \frac{\epsilon}{T}) a_0t]^\theta, & t \gg t_0, \end{cases} \quad (4.11)$$

where θ is the asymptotic growth exponent:

$$\theta(\epsilon, T) = \frac{1}{2 + \epsilon/T}. \quad (4.12)$$

Thus, the growth exponent θ depends explicitly on T and ϵ .

4.3 Numerical Results

4.3.1 Dynamical Scaling and Growth Laws

The details of the simulations are as follows. Our simulations were done on a RBIM with $N = 4096^2$ spins, using the standard Glauber spin-flip algorithm (see Sec. 1.2.1).

The initial configurations were homogeneous mixtures of up and down spins, corresponding to the disordered state at $T = \infty$. The system is quenched to the final temperature $T = 0.5$. We average over at least 6 runs with different initial states and different realizations of noise. In this subsection, we mainly focus on disorder amplitudes $\epsilon = 0$ (pure case) and $\epsilon = 1$ (maximally disordered case).

The domain growth for $\epsilon = 0, 1$ is shown in Fig. 4.1. In Fig. 4.2, we demonstrate the dynamical scaling of the correlation function and structure factor. In Fig. 4.2(a), we superpose data for the scaled correlation function [$C(r, t)$ vs. r/L] for the pure case ($\epsilon = 0$). Figure 4.2(b) shows the corresponding data for $\epsilon = 1$. In both cases, the data sets at different times collapse onto a master function. Figures 4.2(c) and (d) are the scaling plots for the structure factor [$L^{-d}S(k, t)$ vs. kL]. Notice that the maximally disordered case ($\epsilon = 1$) still exhibits Porod's law, $S(k, t) \sim k^{-(d+1)}$ as $k \rightarrow \infty$. Thus, even in the presence of disorder, the interfaces remain sharp and do not acquire a fractal shape.

In Fig. 4.3(a), we plot the scaled correlation function at the same time, but for different disorder amplitudes. The scaling functions collapse onto a master function, indicating that they are independent of the disorder amplitude. We refer to this as *super-universality* of the correlation function [12, 13]. Figure 4.3(b) shows the corresponding super-universality of the scaled structure factor.

In Fig. 4.4, we show the time-dependence of the length-scale, $L(t)$ vs. t . For the pure case ($\epsilon = 0$), the data is consistent with the Allen-Cahn growth law, $L(t) \sim t^{1/2}$. For the disordered case ($\epsilon = 1$), the data is consistent with power-law growth but with a reduced exponent $\theta \simeq 0.195$. For all disorder amplitudes, we find power-law growth but with an exponent which depends on ϵ and T as in Eq. (4.12). This is consistent with the results of Paul et al. [14].

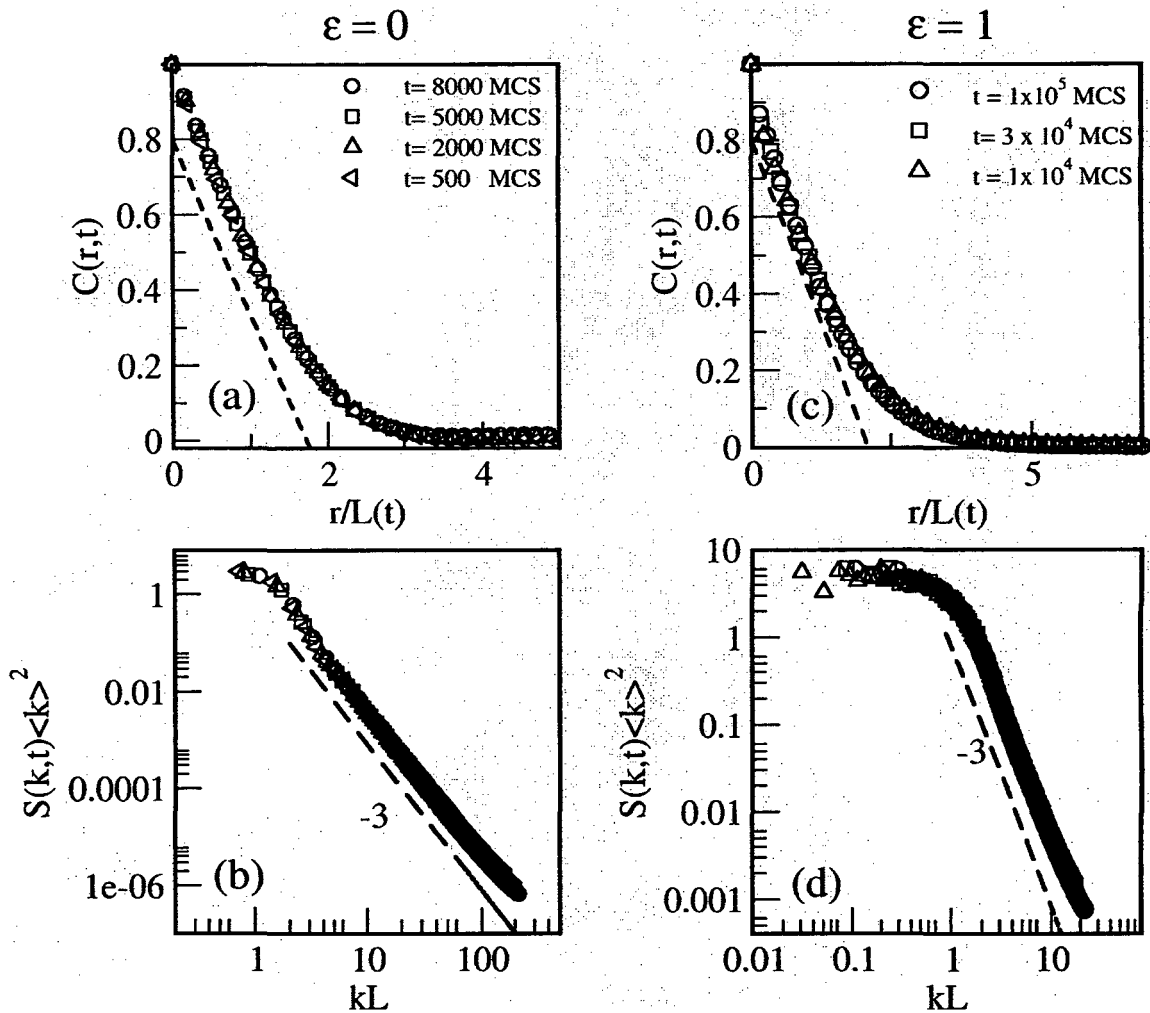


Figure 4.2: (a) Scaled correlation function [$C(r,t)$ vs. r/L] for the evolution of the Glauber-RBIM at $T = 0.5$. This plot is for the pure case, $\epsilon = 0$. (b) Analogous to (a), but for the maximally disordered case, $\epsilon = 1$. (c) Scaled structure factor [$L^{-d}S(k,t)$ vs. kL] for $\epsilon = 0$. The solid line denotes the Porod tail in $d = 2$ with slope -3 , $S(k,t) \sim k^{-(d+1)}$ as $k \rightarrow \infty$. (d) Analogous to (c) but for $\epsilon = 1$.

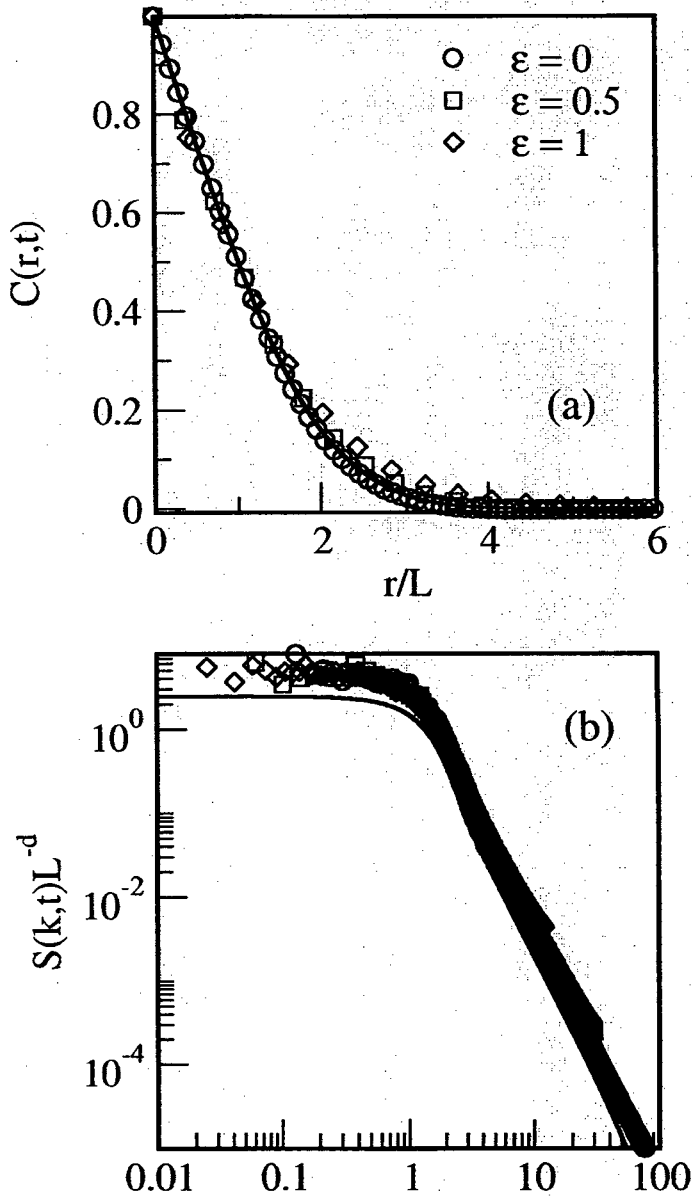


Figure 4.3: Superscaling of correlation function and structure factor. (a) We plot equal time correlation function for $\epsilon = 0, 0.5$ at time $t = 3000$. The data for $\epsilon = 1$ is at time $t = 10^6$ MCS. The growth law for $\epsilon = 1$ is much slower than growth law for $\epsilon = 0, 0.25$ [see Fig. 4.4], hence a late time data is used to ensure the scaling. The solid line is OJK function. (b) Similar plot of structure factor for $\epsilon = 0, 0.5, 1$. The fourier transform of OJK function is also plotted.

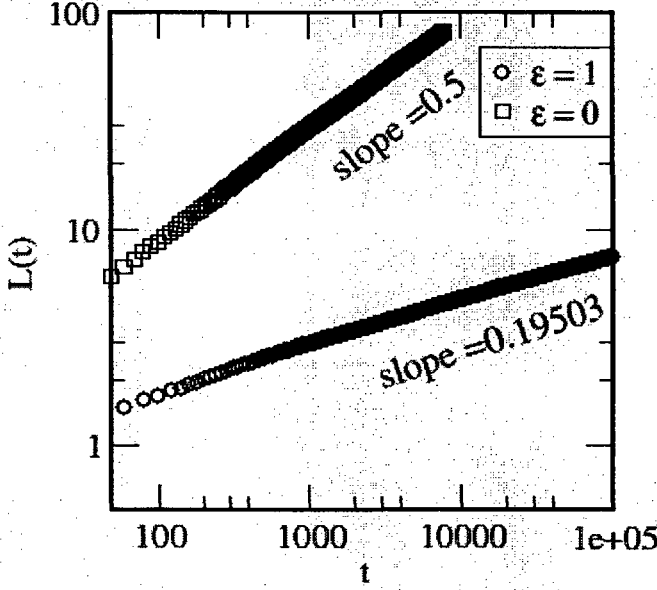


Figure 4.4: Domain growth laws in 2- d RBIM with Glauber kinetics at quench temperature $T = 0.5$. All statistical data is obtained on 4096^2 systems, as an average over 6 independent runs. The disorder values are $\epsilon = 0$ (pure case) and $\epsilon = 1$ (case with maximum disorder).

4.3.2 Autocorrelation and Response Functions

Definitions and Limiting Behaviors

Next, we focus on the autocorrelation and response functions. The *autocorrelation function* is defined as

$$C(t, t_w) = \frac{1}{N} \sum_{i=1}^N [\langle S_i(t_w) S_i(t) \rangle - \langle S_i(t_w) \rangle \langle S_i(t) \rangle]. \quad (4.13)$$

The *response function* is defined as follows. If a small field $h(\vec{r}, t)$ is turned on for the interval (t_1, t_2) after the quench, then the magnetization for $t \geq t_2$ is

$$\langle m(\vec{r}, t) \rangle_h = \langle m(\vec{r}, t) \rangle_{h=0} + \int d\vec{r}' \int_{t_1}^{t_2} dt' R(\vec{r} - \vec{r}', t, t') h(\vec{r}', t') + O(h^2). \quad (4.14)$$

Then, the linear response function is

$$R(\vec{r} - \vec{r}', t, t_w) = \left. \frac{\delta \langle m(\vec{r}, t) \rangle_h}{\delta h(\vec{r}', t_w)} \right|_{h=0}. \quad (4.15)$$

The corresponding *autoresponse function* is

$$R(t, t_w) \equiv R(0, t, t_w). \quad (4.16)$$

Before we show numerical results for these quantities, let us make a few general observations. One important property of aging phenomena is the separation of time-scales. Let us assume that t_w and the time-step $\tau (= t - t_w)$ are sufficiently large. Then, the time-step can be categorized into two parts: (1) short times, i.e., $\tau \ll t_w$, and (2) late times, i.e., $\tau \gg t_w$. For short τ , the system appears locally equilibrated at the final temperature, i.e.,

$$\begin{aligned} C(t, t_w) &= C_{\text{eq}}(\tau, T), \\ R(t, t_w) &= R_{\text{eq}}(\tau, T). \end{aligned} \quad (4.17)$$

The two quantities are time-translation-invariant (TTI), and exhibit the same behavior as if equilibrium at the final temperature of the quench has been reached.

At the other limit, i.e., for $\tau \gg t_w$, the true off-equilibrium behavior of the system is observed and the scaling form of the quantities can be written as

$$\begin{aligned} C(t, t_w) &= C_{\text{ag}}(t, t_w) = t_w^{-b} h_C \left(\frac{t}{t_w} \right), \\ R(t, t_w) &= R_{\text{ag}}(t, t_w) = t_w^{-(1+a)} h_R \left(\frac{t}{t_w} \right), \end{aligned} \quad (4.18)$$

where a, b are non-negative exponents and h_C, h_R are scaling functions. The scaling form of Eq. (4.18) also illustrates that relaxation at late stages is controlled by t_w only. Thus, the existence of fast and slow degrees of freedom becomes characteristic of aging or slow relaxation dynamics.

In the context of domain growth in a ferromagnetic system, the fast degrees of freedom are responsible for the thermal fluctuations within the ordered domains, and the slow ones can be thought of as labels of domains. For a given t_w , the typical size of a domain is $L(t_w) \sim t_w^{1/z}$, and it takes an interval of time $\tau \sim t_w$ for a domain wall to sweep the whole domain. Thus, in the short-time regime, the slow degrees of freedom do not evolve much and the main contribution comes from the fast degrees of freedom in the decay of two-time quantities, yielding the behavior in Eq. (4.17). Similarly, in the asymptotic state (i.e., at $\tau \gg t_w$), the off-equilibrium behavior is dominated by the motion of domain walls and the scaling form is given by Eq. (4.18).

However, the interpretation of aging behavior in terms of fast and slow degrees of freedom is less clear when the system is quenched to the critical temperature T_c . In the quench to T_c , stationary and aging behaviors match multiplicatively, whereas in the quench below T_c , the matching is additive [1].

For the quench to T_c , the analytical calculation of the exponents a, b and the scaling functions h_C, h_R is done through expansion methods, e.g., the ϵ -expansion [17, 18, 19]. On the other hand, for quenches below T_c , a Gaussian auxiliary field (GAF) approximation of the OJK type in Sec. 1.4.5 is successfully applied [20, 21, 22, 23, 24]. However, the computation of the autoresponse function $R(t, t_w)$ remains very complicated. For this reason, the study of aging in quenches below T_c relies heavily on numerical simulations, although the accurate numerical computation of $R(t, t_w)$ is not straightforward [25, 26].

Autocorrelation Function

In Fig. 4.5, we show the time-dependence of the autocorrelation function $C(t, t_w)$ for $\epsilon = 0, 1$. In Figs. 4.5(a) and (b), we plot $C(t, t_w)$ vs. t . In Figs. 4.5(c) and (d), we plot $C(t, t_w)$ vs. t/t_w . In the latter case, a nice data collapse is observed, which is consistent with simple aging. Our scaling plot implies that $b = 0$, which is also found in the pure case. Also note that the observed scaling form of the autocorrelation function is consistent with the algebraic form of the growth laws.

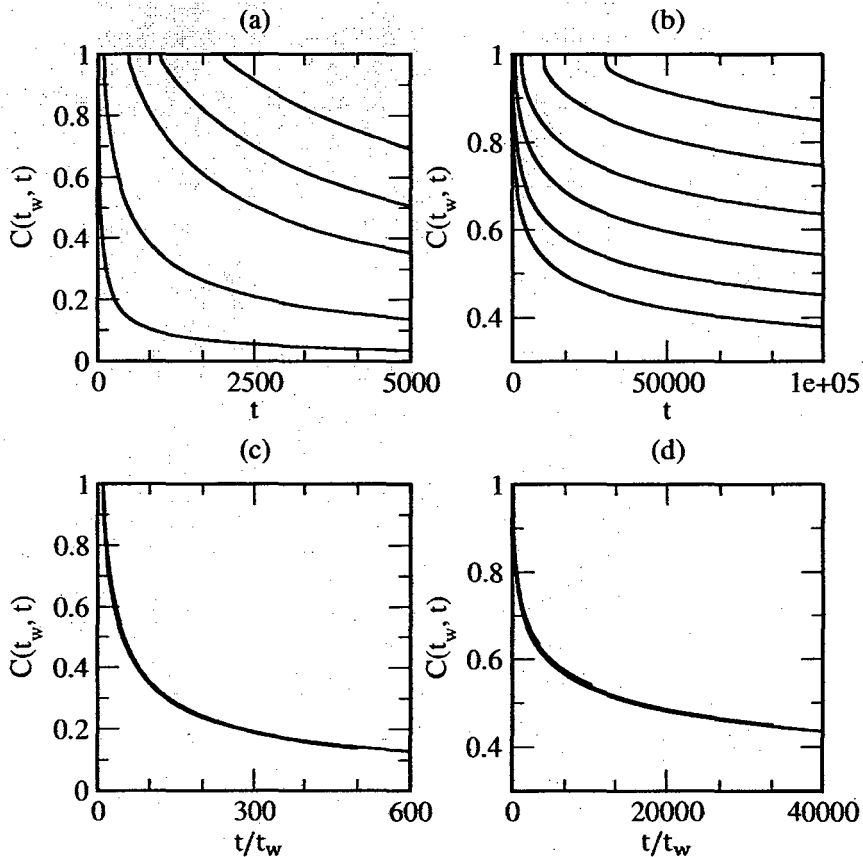


Figure 4.5: (a) Plot of autocorrelation function, $C(t, t_w)$ vs. t , for $\epsilon = 0$. The waiting times are (from left to right) $t_w = 100, 200, 500, 1000, 2000$. (b) Analogous to (a), but for the case $\epsilon = 1.0$. The waiting times are $t_w = 100, 300, 1000, 3000, 10000$ and 30000 . (c) Scaling plot of data in (a), $C(t, t_w)$ vs. t/t_w . (d) Scaling plot of data in (b), $C(t, t_w)$ vs. t/t_w .

Response Function and Related Quantities

Let us next consider the autoresponse function, which was defined in Eq. (4.15). With a time-independent external field, Eq. (4.14) takes the form

$$\langle m(\vec{r}, t) \rangle_h = \langle m(\vec{r}, t) \rangle_{h=0} + \int d\vec{r}' \zeta(\vec{r} - \vec{r}', t, t_1, t_2) h(\vec{r}') + O(h^2), \quad (4.19)$$

where $\zeta(\vec{r} - \vec{r}', t, t_1, t_2)$ is the *integrated linear response function*:

$$\zeta(\vec{r} - \vec{r}', t, t_2, t_1) = \int_{t_1}^{t_2} dt' R(\vec{r} - \vec{r}', t, t'). \quad (4.20)$$

We can derive two important quantities from the definition of the integrated linear response function. The first is the *thermoremanent magnetization* (TRM), corresponding to the choice $t_1 = 0, t_2 = t_w$:

$$\rho(\vec{r}, t, t_w) = \zeta(\vec{r}, t, t_w, 0). \quad (4.21)$$

The second quantity is the *zero-field-cooled* (ZFC) susceptibility with $t_1 = t_w, t_2 = t$:

$$\chi(\vec{r}, t, t_w) = \zeta(\vec{r}, t, t, t_w). \quad (4.22)$$

A direct numerical calculation of the autoresponse function $R(t, t_w)$ is considerably more difficult than the evaluation of $C(t, t_w)$. The reason is that $R(t, t_w)$ is much more noisy than $C(t, t_w)$. One way to handle this difficulty is to study less noisy integrated response functions, e.g., TRM [Eq. (4.21)], ZFC susceptibility [Eq. (4.22)]. Below the critical temperature T_c , using the additive structure of the response function, the

ZFC susceptibility can be written as

$$\chi(t, t_w) = \chi_{\text{eq}}(t, t_w) + \chi_{\text{ag}}(t, t_w), \quad (4.23)$$

where the first component satisfies stationarity, and the second part is the contribution of aging. Again, χ_{ag} can be written as

$$\chi_{\text{ag}}(t, t_w) = \int_{t_w}^t dt' R_{\text{ag}}(t, t'). \quad (4.24)$$

Hence, the scaling form of this quantity can be written as [cf. Eq. (4.18)]

$$\chi_{\text{ag}}(t, t_w) = t_w^{-a} h_{\chi}(x), \quad (4.25)$$

and for large x , $h_{\chi}(x) \sim x^{-a}$. This implies that the asymptotic form can be written as

$$\chi_{\text{ag}}(t, t_w) \sim t^{-a}. \quad (4.26)$$

An intuitive argument, due to Barrat [27], predicts that $\chi_{\text{ag}}(t, t_w)$ should be proportional to the density of defects at the time t_w , which behaves as $L(t_w)^{-m}$, where $m = 1$ and 2 for a scalar and vector order parameter, respectively. However, analytical results which involve exact solutions of the large- N model [28], $d = 1$ Ising model [29], as well as other approximate calculations show that the exponent a has a linear dependence on d . The relevant expression is [1]

$$a = \frac{m}{z} \left(\frac{d - d_L}{d^* - d_L} \right), \quad (4.27)$$

where d_L is the lower critical dimension, and d^* is the upper critical dimension. For the 2- d Ising system without disorder, we have $d = 2$, $d^* = 3$, $d_L = 1$ and $z = 2$, $m = 1$. Thus the product $az = 1/2$. In this chapter, we study the corresponding relationship for the RBIM.

Let us next present results for the exponent a and the form of the scaling function. In our simulations, we measure the quantity

$$\chi_{\text{ag}}(t, t_w) = \frac{1}{Nh_0^2} \sum_{i=1}^N \overline{\langle S_i \rangle h_i}, \quad (4.28)$$

where h_i is a quenched configuration of uncorrelated random fields with values $\pm h_0$ and $h_0 = 0.05$. The angular brackets denote an average over independent initial conditions. The overbar denotes an average over random field configurations. The simulation has been done at temperature $T = 0.5$. (Note that the critical temperature $T_c \simeq 2.269$.) We have also extended the calculation of $\chi_{\text{ag}}(t, t_w)$ taking into consideration the presence of quenched disorder. First, we obtain the value of a by plotting $\chi_{\text{ag}}(t, t_w)$ vs. t_w for a fixed ratio of $x = t/t_w = 10$ in Fig. 4.6. A clean power-law behavior is observed, which enables us to identify a . The values of t_w in Fig. 4.6 are 50, 100, 200, 500, 1000. The statistical data is obtained as an average over 100 independent initial conditions and disorder configurations.

Next, we present results for the scaling function χ_{ag} . In Fig. 4.7, we plot $T\chi_{\text{ag}}$ vs. t for the pure case, i.e., $\epsilon = 0$. The asymptotic power-law decay provides an independent value of $a \simeq 0.30$, which is consistent with the value from Fig. 4.6(a).

In Figs. 4.8 and 4.9, we plot $T\chi_{\text{ag}}$ vs. t for the disorder values $\epsilon = 0.5, 0.75$.

Finally, we obtain data for z [14] and the value of a from our numerical calculation, to ascertain the validity of Eq. (4.27). Our understanding is that the product az is independent of the disorder, and $az = 0.5$. The plot of az vs. ϵ is shown in Fig. 4.10.

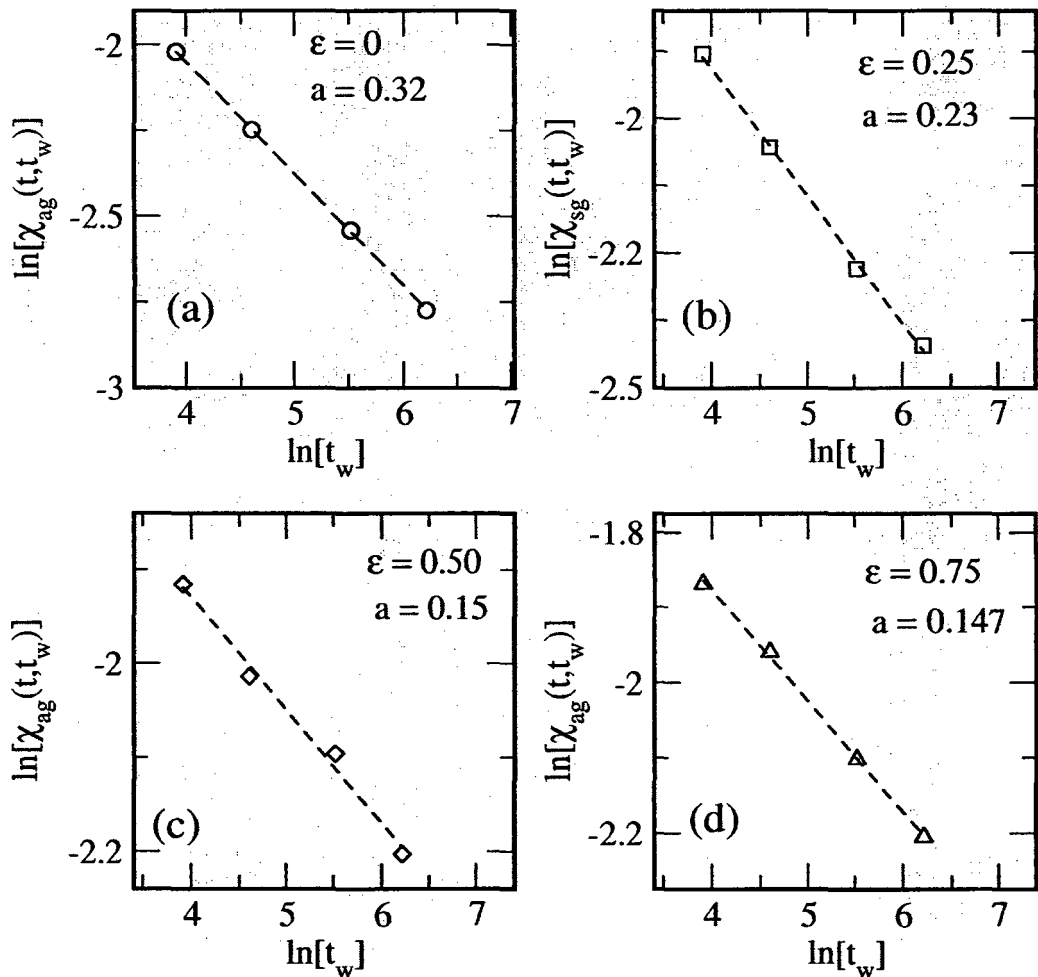


Figure 4.6: Log-log plot of $\chi_{ag}(t, t_w)$ vs. t_w for the Glauber-RBIM with fixed $x = t/t_w = 10$. The various frames correspond to (a) $\epsilon = 0$ (pure case); (b) $\epsilon = 0.25$; (c) $\epsilon = 0.5$; and (d) $\epsilon = 0.75$; The best linear fits to the data are shown as dashed lines – these determine the exponent a .

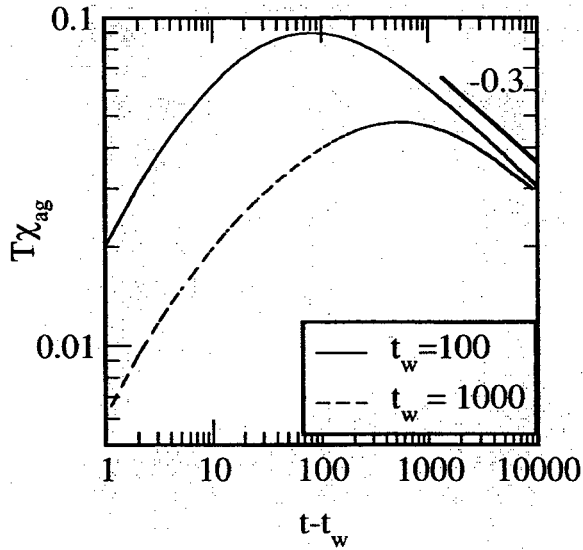


Figure 4.7: Plot of $T\chi_{ag}(t, t_w)$ vs. $\tau = t - t_w$ for disorder value $\epsilon = 0$. The asymptotic is power law with exponent $a \simeq 0.30$. The simulation has been done on a 4096^2 lattice with an average over 15 independent runs. We show data for waiting times $t_w = 100, 1000$.

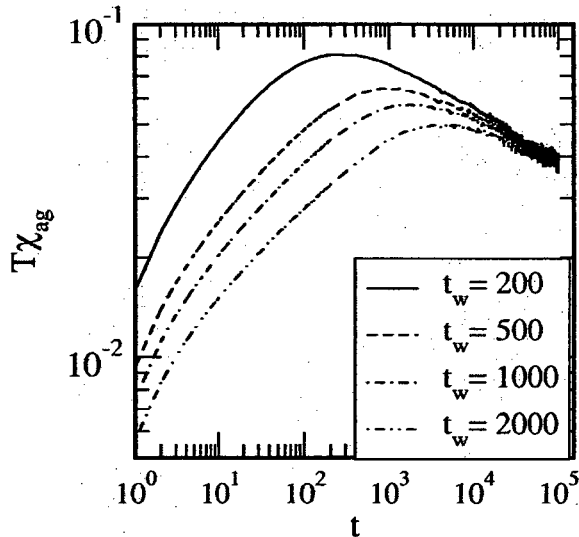


Figure 4.8: Analogous to Fig. 4.7 but for $\epsilon = 0.5$. The simulation has been done on a 4096^2 lattice with an average over 85 runs. The waiting times are $t_w = 200, 500, 1000, 2500$.

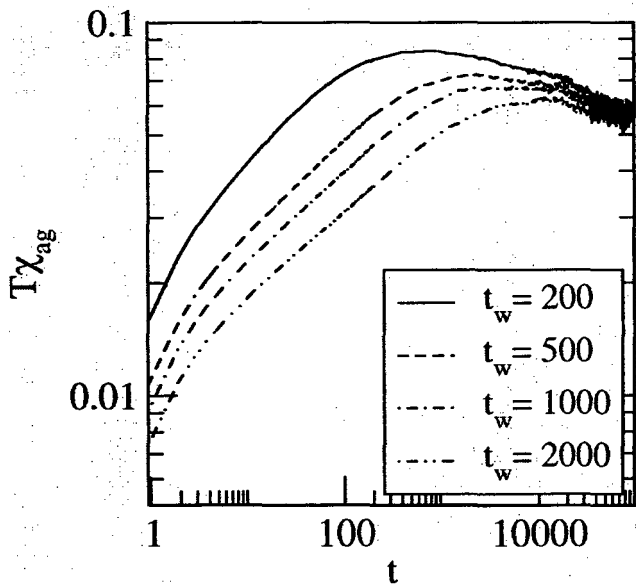


Figure 4.9: Analogous to Fig. 4.7 but for $\epsilon = 0.75$. The simulation has been done on a 4096^2 lattice with an average over 85 runs. The waiting times are $t_w = 200, 500, 1000, 2500$.

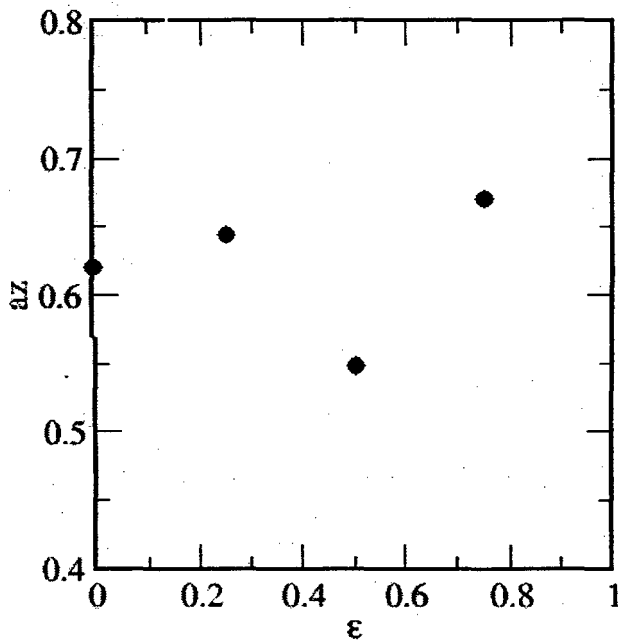


Figure 4.10: Plot of az vs. ϵ .

4.4 Summary and Discussion

We conclude this chapter with a summary and discussion of the results presented here. In this chapter, we have focused on domain growth in ferromagnets with quenched disorder. We modeled this system via a *random-bond Ising model* (RBIM) with Glauber spin-flip kinetics. The disorder amplitude was such that the bonds were always ferromagnetic. In this chapter, we have studied the morphological features of domain growth, as well as aging and slow relaxation.

We found that the scaled correlation functions and structure factors for the Glauber-RBIM are independent of the disorder amplitude. These are numerically indistinguishable from the corresponding functions for the pure case. We refer to this as *super-universal scaling* of the correlation function and structure factor. The domain growth laws show a power-law behavior, $L(t) \sim t^\theta$, with an exponent θ which depends on the disorder amplitude and temperature. Our results for domain growth are consistent with a scenario where the coarsening domains are trapped by quenched disorder sites with an energy barrier which grows logarithmically with the domain size.

We also studied two-time functions like the autocorrelation function and the response function. We have obtained detailed numerical results for the behavior of these quantities at late times. In particular, we have quantified the exponent which governs the power-law decay of the autoresponse function in the asymptotic regime.

Bibliography

- [1] S. Puri and V. K. Wadhawan (eds.), *Kinetics of Phase Transitions*, CRC Press, Boca Raton, Florida (2009).
- [2] J. P. Bouchaud, L. F. Cugliandolo, J. Kurchan and M. Mezard, in *Spin Glasses and Random Fields*, A. P. Young (ed.), World Scientific, Singapore (1997).
- [3] L. C. E. Struik, *Physical Aging in Amorphous Polymers and Other Materials*, Elsevier, Amsterdam (1978).
- [4] Z. W. Lai, G. F. Mazenko and O. T. Valls, *Phys. Rev. B* **37**, 9481 (1988).
- [5] D. A. Huse and C. L. Henley, *Phys. Rev. Lett.* **54**, 2708 (1985).
- [6] G. S. Grest and D. J. Srolovitz, *Phys. Rev. B* **32**, 3014 (1985).
- [7] J. H. Oh and D. I. Choi, *Phys. Rev. B* **33**, 3448 (1986).
- [8] B. Biswal, S. Puri and D. Chowdhury, *Physica A* **229**, 72 (1996).
- [9] H. Ikeda, Y. Endoh and S. Itoh, *Phys. Rev. Lett.* **64**, 1266 (1990).
- [10] V. Likodimos, M. Labardi and M. Allegrini, *Phys. Rev. B* **61**, 14440 (2000).
- [11] V. Likodimos, M. Labardi, X. K. Orlik, L. Pardi, M. Allegrini, S. Emonin and O. Marti, *Phys. Rev. B* **63**, 064104 (2001).

- [12] S. Puri and N. Parekh, *J. Phys. A* **24**, 4127 (1992).
- [13] M. F. Gyure, S. T. Harrington, R. Strilka, and H. E. Stanley, *Phys. Rev. E* **52**, 4632 (1995).
- [14] R. Paul, S. Puri and H. Rieger, *Europhys. Lett.* **71**, 061109 (2005).
- [15] C. L. Henley, *Phys. Rev. Lett.* **54**, 2030 (1985).
- [16] R. Rammal and A. Benoit, *Phys. Rev. Lett.* **55**, 649 (1985).
- [17] H. K. Janssen, B. Schaub and B. Schmittmann, *Z. Phys. B Cond. Matter* **73**, 539 (1989).
- [18] H. K. Janssen, in *From Phase Transitions to Chaos: Topics in Modern Statistical Physics*, G. K. Gyorgyi, L. I. Sasvari and T. Tel (eds.), World Scientific, Singapore (1992).
- [19] P. Calabrese and A. Gambassi, *J. Phys. A Math. Gen.* **38**, R133 (2005).
- [20] Y. Oono and S. Puri, *Mod. Phys. Lett. B* **2**, 861 (1988).
- [21] G. F. Mazenko, *Phys. Rev. Lett.* **63**, 1605 (1989).
- [22] G. F. Mazenko, *Phys. Rev. B* **42**, 4487 (1990).
- [23] A. J. Bray and K. Humayun, *Phys. Rev. E* **48**, R1609 (1993).
- [24] S. De Siena and M. Zannetti, *Phys. Rev. E* **50**, 2621 (1994).
- [25] E. Lippiello, F. Corberi and M. Zannetti, *Phys. Rev. E* **71**, 036104 (2005).
- [26] E. Lippiello, F. Corberi and M. Zannetti, *Phys. Rev. E* **72**, 056103 (2005).
- [27] A. Barrat, *Phys. Rev. E* **57**, 3629 (1998).

[28] F. Corberi, E. Lippiello and M. Zannetti, Phys. Rev. E **65**, 046136 (2002).

[29] E. Lippiello and M. Zannetti, Phys. Rev. E **61**, 3369 (2000).

Chapter 5

Introduction to Dynamical Properties of Granular Gases

5.1 Granular Systems

Granular systems are one of the most fascinating forms of organization of matter. They are large collections of discrete macroscopic particles (e.g., sand, beads, pellets, seeds, nuts, ball-bearings, etc.), and physical dimensions ranging from $1 \mu\text{m}$ to 1mm . Granular materials are also ubiquitous in nature and play a crucial role in many industrial applications, geological phenomena and other segments of everyday life. On the other hand, granular materials are extremely complicated to handle since they reveal many interesting behaviors under different circumstances: an excited granular materials often resembles a fluid. It flows through pipes or flows inside a hour-glass. It also behaves like a solid sometimes, e.g., a heap of sand does not flow like liquid. There are also intermediate stages, e.g., a vibrated granular material shows convective flows and also forms static surface structures which do not dissolve. Again, extremely dilute granular materials under certain conditions exhibit a gas-like

phase. The energy of a granular gas dissipates quickly and it transforms into a liquid or solid phase. However, without gravity or any other external force, the gaseous state persists for long times. Granular gases have been found in the planetary rings (e.g., Saturn's rings) of our solar system.

Although granular materials demonstrate such a rich phenomenology, they remain a challenge to physicists to come up with a successful theory to explain their behavior. Engineers have already gathered enormous amount of technical and experimental details, but our technical understanding of granular materials are still poor as compared to that of other materials: silos and hoppers continue to collapse, though they are constructed with state-of-the-art technology.

There is also need for numerical simulations of granular materials for various reasons. Since there is no comprehensive theory developed yet, predictions of numerical simulations optimize the function of machinery of powder technology. Also, experiments with granular materials are expensive and time-consuming. In such cases, numerical simulations can supplement or partly replace experiments.

5.1.1 Dynamical Properties of Granular Gases

In this thesis, we have studied freely-evolving inelastic granular gases via molecular dynamics simulation. A granular gas is a collection of continually colliding macroscopic particles – the typical time between successive collisions among the particles is much larger than the time of contact during collisions. In fact, in simulations, the collision process is modeled as being instantaneous.

Let us examine the dynamical evolution in more detail. The system is initially prepared in a state of thermal equilibrium with temperature T_0 . However, due to the inelastic nature of the collisions, the particles slow down, i.e., loose part of their

kinetic energy. The *granular temperature* $T(t)$ of the gas is described as the average kinetic energy of the grains, i.e.,

$$\frac{d}{2}T(t) = \left\langle \frac{1}{2}m\bar{v}^2 \right\rangle = \frac{1}{N} \sum_{i=1}^N \frac{1}{2}m\bar{v}_i^2, \quad (5.1)$$

where d is dimensionality of the system, m is mass of the granular grains and \bar{v}_i is the velocity of the i^{th} particle. This is analogous to the temperature in the theory of molecular gas.

Loss of average kinetic energy or cooling makes a granular gas very different from a molecular gas, where collisions between particles are considered elastic. The size of the granular particles is also large enough that they are not subjected to thermal fluctuations.

During the first stage of the evolution, the granular gas remains homogeneous in the density field. This part of the evolution is known as the *homogeneous cooling state* (HCS). However, the average kinetic energy $E(\tau)$ of the system decreases exponentially when measured in τ , where τ is average number of collisions suffered per particle. This decay of energy is known as *Haff's law* in the literature.

However, the HCS with a spatially uniform density and temperature, and with a vanishing flow field is unstable against long-wavelength spatial fluctuations. This leads finally to a state with large-scale clusters in the density field $n(\vec{r}, t)$ as well as in the flow field $\vec{u}(\vec{r}, t)$ (vortices). This is illustrated in the MD simulations of Fig. 5.1 and Fig. 5.2 [also see Fig. 6.2 and Fig. 6.3].

In this state, cooling slows down and large deviations from Haff's law occur. The asymptotic state is known as the *inhomogeneous cooling state* (ICS). The formation of clusters can be explained by some simple arguments. Let us consider some fluctuations in the density field. In denser regions, the particles collide more frequently than in

dilute regions. More collisions imply that particles loose energy rapidly, thereby dense regions cool down faster than dilute regions, and the local pressure in these regions decrease comparatively. Hence, a pressure gradient is set up in the density field and particles are sucked into the dense regions and this increase the density further. From this argument, it follows that initial small fluctuations in the density field is highly unstable due to a pressure instability, which results in formation of clusters.

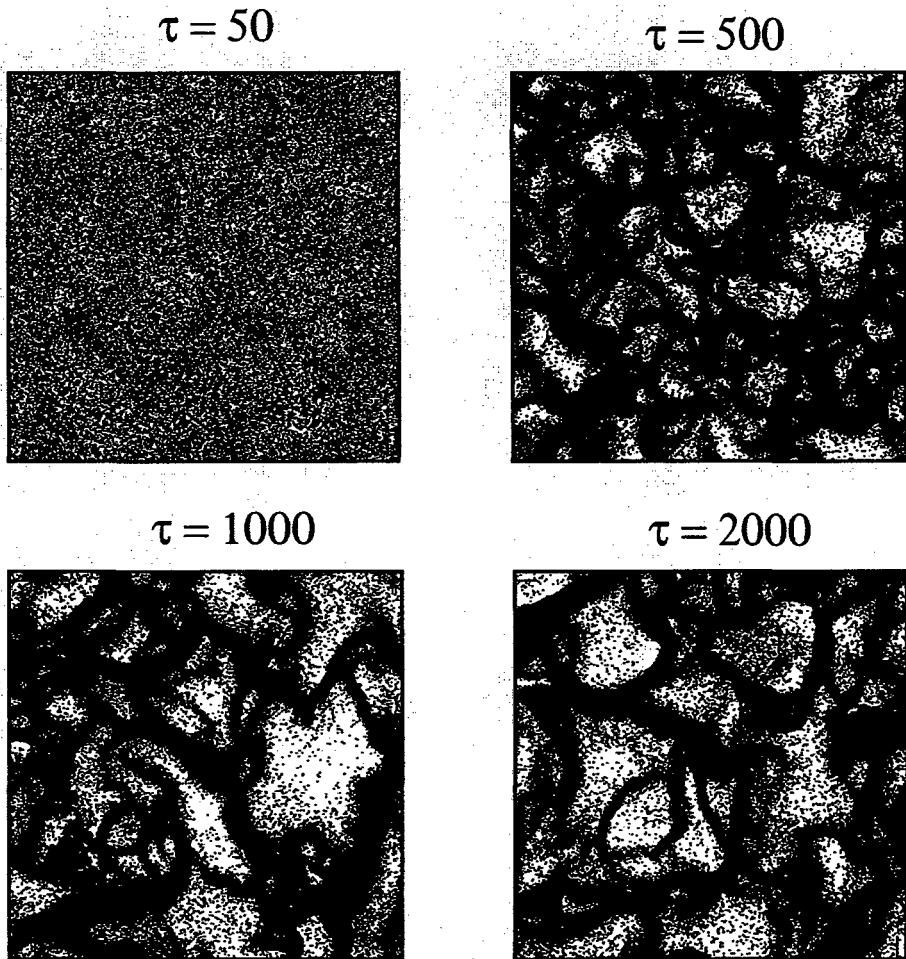


Figure 5.1: A 2- d evolution picture of a freely-evolving inelastic granular gas from a homogeneous initial condition [cf. Fig. 1.2]. The number density of the system is $n = 0.30$ and coefficient of restitution $e = 0.9$. The system size is 2048^2 . The initial kinetic energy of the system is $E(0) = 200$ (dimensionless units). The snapshots are labeled by the average collision time τ .
Cluster

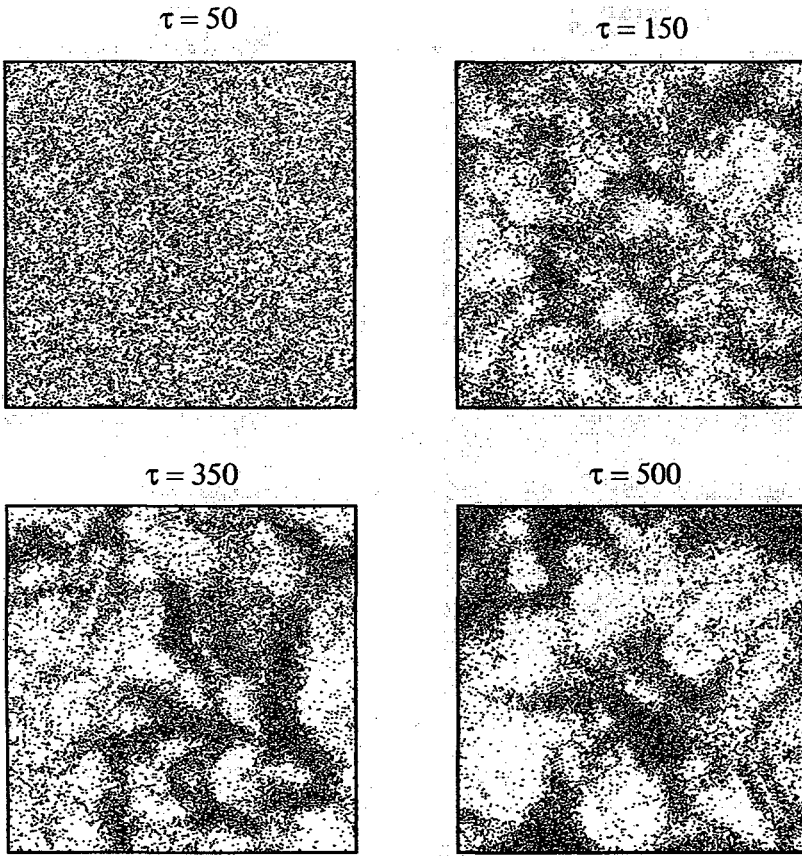


Figure 5.2: A 3- d evolution picture of a freely-evolving inelastic granular gas from a homogeneous initial condition. The snapshots shown lie in a 2- d slice of the XY plane at $z = 0$ with a thickness $\delta z = 2$. The number density of the system is $n = 0.30$ and coefficient of restitution $e = 0.7$. The system size is 80^3 . The initial kinetic energy of the system is $E(0) = 20000$ (dimensionless unit). The snapshots are labeled by the average collision time τ .

5.2 Implementation of Event-Driven Algorithm

The general approach of molecular dynamics is to solve Newton's equations of motion for a system of particles:

$$\ddot{\vec{r}}_i = \frac{1}{m} \vec{F}_i(\vec{r}_1, \vec{v}_1; \dots; \vec{r}_N, \vec{v}_N). \quad (5.2)$$

This scheme has been successfully implemented in diverse cases; however there are some specific examples where force-based calculations of molecular dynamics are not

that effective, for instance dilute granular systems. A granular gas is modeled as a collection of interacting hard spheres colliding inelastically with one other; they propagate along a trajectory with constant velocity unless interrupted by collisions. Therefore, instead of any fixed time-step, the pair-wise collision of particles can be considered an instantaneous event and each of those events may be treated separately.

The main assumption for applying event-driven molecular dynamics is that at any instant of time in the entire system there occurs only one collision of infinitesimal time duration. The collision changes the velocity of the involved particles according to the laws of collision. The benefit of such algorithm is to avoid time expensive calculation of trajectories of all particles according to Eq. (5.2), and dynamics of the system is determined by a sequence of discrete events.

5.2.1 Collision of Particles

In an inelastic collision, the total linear momentum is always conserved. Hence, we can write the conservation equation as

$$m_i \vec{v}_i' + m_j \vec{v}_j' = m_i \vec{v}_i + m_j \vec{v}_j. \quad (5.3)$$

Here, \vec{v}_i' and \vec{v}_j' are post-collisional velocities, and \vec{v}_i and \vec{v}_j are pre-collisional velocities. We also assume that the spheres are perfectly smooth, and consequently only the normal component of velocities of the colliding particles is diminished by a factor e , which is defined as

$$(\vec{v}_i' - \vec{v}_j') \cdot \hat{n} = -e (\vec{v}_i - \vec{v}_j) \cdot \hat{n}, \quad (5.4)$$

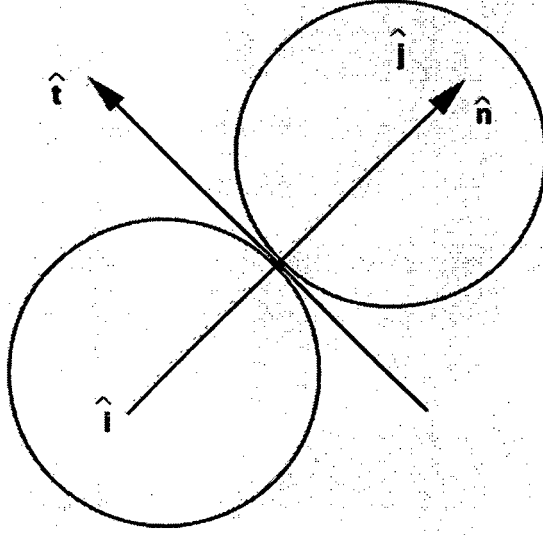


Figure 5.3: Collision of hard spheres.

where \hat{n} is a unit vector joining the centers of particles i and j . This is illustrated in Fig. 5.3.

Now, combining Eq. (5.3) and Eq. (5.4), we obtain

$$\begin{aligned}\vec{v}_i' \cdot \hat{n} &= \left(\frac{m_i - em_j}{m_i + m_j} \right) \vec{v}_i \cdot \hat{n} + \left(\frac{m_j}{m_i + m_j} \right) (1 + e) \vec{v}_i \cdot \hat{n}, \\ \vec{v}_j' \cdot \hat{n} &= \left(\frac{m_j - em_i}{m_i + m_j} \right) \vec{v}_j \cdot \hat{n} + \left(\frac{m_i}{m_i + m_j} \right) (1 + e) \vec{v}_j \cdot \hat{n},\end{aligned}$$

which can be further simplified by introducing the variable $\vec{v}_{ij} = \vec{v}_i - \vec{v}_j$. The final form of the collision rule is

$$\begin{aligned}\vec{v}_i' &= \vec{v}_i - \left(\frac{m_j}{m_i + m_j} \right) (1 + e) [(\vec{v}_i - \vec{v}_j) \cdot \hat{n}] \hat{n}, \\ \vec{v}_j' &= \vec{v}_j + \left(\frac{m_i}{m_i + m_j} \right) (1 + e) [(\vec{v}_i - \vec{v}_j) \cdot \hat{n}] \hat{n}.\end{aligned}\tag{5.5}$$

Equation (5.5) determines the velocity change after an inelastic collision. The above

result can be further simplified if we consider identical hard spheres, i.e., $m_i = m_j$:

$$\begin{aligned}\vec{v}_i' &= \vec{v}_i - \left(\frac{1+e}{2}\right) [(\vec{v}_i - \vec{v}_j) \cdot \hat{n}] \hat{n}, \\ \vec{v}_j' &= \vec{v}_j + \left(\frac{1+e}{2}\right) [(\vec{v}_i - \vec{v}_j) \cdot \hat{n}] \hat{n}.\end{aligned}\quad (5.6)$$

5.2.2 Sketch of the Algorithm

An algorithm for the simulation of granular gas using the collision rule in Eq. (5.6) is given below.

- (1) The system is initialized with random positions, and velocities are chosen with fixed magnitude but random directions so that $\sum_i \vec{v}_i = 0$.
- (2) Determine the 1st collision time t_{\min} , when the next collision occurs in the system. If two particles i and j collide in time t^* , then the equation

$$|[\vec{r}_i + (t^* - t) \vec{v}_i] - [\vec{r}_j + (t^* - t) \vec{v}_j]| = R_i + R_j, \quad (5.7)$$

has a real solution t^* . This equation can be further simplified to a quadratic equation, and the smallest root can be found as

$$t^* = t - \frac{\vec{r}_{ij} \cdot \vec{v}_{ij}}{v_{ij}^2} - \sqrt{\left(\frac{\vec{r}_{ij} \cdot \vec{v}_{ij}}{v_{ij}^2}\right)^2 + \frac{R_{ij}^2 - \vec{r}_{ij}^2}{v_{ij}^2}}, \quad (5.8)$$

where $\vec{r}_{ij} = \vec{r}_i - \vec{r}_j$, $\vec{v}_{ij} = \vec{v}_i - \vec{v}_j$, $R_{ij} = R_i + R_j$, R_i being the radius of the i^{th} particle. The sufficient condition that a real solution of Eq. (5.8) exists is as follows:

$$\vec{r}_{ij} \cdot \vec{v}_{ij} < 0. \quad (5.9)$$

This implies that particles must approach each other. The discriminant of the quadratic equation must also have real roots, i.e.,

$$\sqrt{\left(\frac{\vec{r}_{ij} \cdot \vec{v}_{ij}}{v_{ij}^2}\right)^2 + \frac{R_{ij}^2 - r_{ij}^2}{v_{ij}^2}} > 0. \quad (5.10)$$

If both conditions given in Eq. (5.9) and Eq. (5.10) are fulfilled, real solution t^* for the collision of the two particles i, j can be obtained from the Eq. (5.8). And t_{\min} will be global minimum time of all possible t^* obtained by calculating the collision time of all particles in the system.

(3) Update the position of all particles at time t_{\min} , given by

$$\vec{r}_i(t_{\min}) = \vec{r}_i(t) + (t_{\min} - t)\vec{v}_i. \quad (5.11)$$

(4) Calculate the new velocities of the colliding particles according to Eq. (5.6).

(5) Update system time $t = t_{\min}$.

(6) Proceed to step 2.

The simple algorithm described above is very time-consuming and inefficient when the system has large number of particles. In fact, it can be shown that the complexity of the overall algorithm is $O(N^2)$. Hence, a more sophisticated algorithm is necessary to handle the simulation. In the next section, we will give the details of the advanced code. We give illustration of part of code in respective sections. The complete code is attached in a CD with this thesis.

5.3 Improved Event-Driven Algorithm

Before we explain the improved algorithm, it will be useful to briefly explain the important classes used in the code. We begin with the *sphere class*:

Listing 5.1 sphere.h

```
1 // sphere.h : Sphere Class
2 #ifndef SPHERE_H_
3 #define SPHERE_H_
4 #include<vector>
5 #include<string>
6 using namespace std;
7 #include"Myvector.h"
8 class particle{
9 private:
10     Vector r; // position vector
11     Vector v; // velocity vector
12     Double T; // inherent particle clock
13     const Double _R ; // radius of a particle
14     Double _D ; // min distance between two spheres
15     Double _L; // Box Size
16     void setDia(){_D = Double(4.0)*(_R)*(_R); }
17     int _Row; // hold row
18     int _Column; // hold Column
19     void SetRowIndex(const int&i){_Row=i;}
20     void SetColmnIndex(const int&i){_Column=i;}
21 public:
22     // rest of the code ...
23 #endif
```

Importance of the variable T in Listing 5.1 will be explained during the “asynchronous updating” stage. The class *Myvector.h* contains the definition of mathematical vector class taken from the book *Computational Granular Dynamics: Models and Algorithms* [1].

Listing 5.2: EventClass.h

```

1 // description of events that will be used
  // in priority queue
3
4 #ifndef EVENT_CLASS1_H_
5 #define EVENT_CLASS1_H_
6     typedef long double Double;
7     class PrioritizeTasks;
8
9     class Event{
10     private:
11         Double priority; // scheduled_time;
12         int event_type; // DDC or VDC
13         int partner;
14         int c;//check invalid events
15     public:
16         Event( const Double time, const int type,
17               const int partner1, const int c1 );
18         friend class PrioritizeTasks; // to set the priority
19                                         // of the events
20         Double Return_Scheduled_Time()
21             const{return priority; }
22         // code continue ..
23         Event MIN (const Event &j1, const Event &j2) const;
24         bool operator==(const Event & q);
25     };
26 #endif

```

An event class holds two types of events:

- (a) *Disk-disk collision* or DDC.
- (b) *Virtual wall collision* or VWC.

Priority of a particular event over all other events is determined by the value of the variable *priority* which holds the corresponding time interval for either a DDC or VWC event. The role of variable *c* will be discussed later on during the “Deletion of events” stage.

Listing 5.3 Box.h

```

//box.h contains the definition of box
2 #ifndef BOX_H_
   #define BOX_H_
4
   #include<iostream>
6 using namespace std;
   #include"Varr.h" // This contains some array operations
8 // insertion, erase of any element etc.
   class cell_matrix{
10 private:
       vector<vector<vector<int> > > cellmatrix; // 3d array
12       vector<int> narr; // holds list of neighbouring particle
                               // for a given particle
14       const int row; // no of unit cells along row
       const int colm; // no of unit cells along column
16
       const Double X_SPACING; // width of an unit cell
18       const Double Y_SPACING; // width of an unit cell

20 // code continues ...
   };
22 #endif

```

The class “box.h” implements the idea of domain decomposition or dividing the space in smaller boxes. This is realized through a 3-*d* array `cell_matrix` as shown in Listing 5.3. The first two index of the array `cell_matrix` denotes the location of the box in space and the third index record the list of particles which belong to that cell. The array is defined via “vector” which is the simplest of the STL container classes. One of the most important properties of STL class vector is that the number of elements in a vector may vary dynamically and memory management is automatic. Finally we define “container.h” in Listing 5.4, which contains all the classes discussed so far and other functions to drive the dynamics.

Listing 5.4: container.h

```

// container.h : it has paricle class and cell class
2 //it also contains all the major important functions
#ifndef CONTAINER_H_
4 #define CONTAINER_H_
#include<vector>
6 #include <functional>
#include <queue>
8 #include<fstream>
#include<string>
10 using namespace std;
#include"Myvector.h"
12 #include"sphere.h"
#include"box.h"
14 #include"event_class1.h"
class Container{
16 private:
//*****
18 vector<particle> HardSphere; // array of particles
const int _No_Of_Particles; // max # of particle
20 const Double _R ; // Radius of the particle
const Double _Lbox ; // Box length
22 const Double Vmax;

24 vector<int> _MYNARR; // neighbour list
int _MYNARR_LENGTH; // size of the neighbour list
26 // cell_matrix Cell; // box
//*****here we do the crucial time management with ARRAY
28 typedef priority_queue<Item, vector<Item>,
PrioritizeTasks> PQ; //task_queue;
30 vector<int> _C; // C matrix
vector<Item> lml; // local minima list
32 vector<int>FEL; // Future event list
vector<PQ> localList; // for each particle
34
// code continues ...
36 };
#endif

```

Now that we are familiar with basic structure of the code, we can focus on how different ideas have been implemented. The algorithm is based on three goals. These are

- 1 Minimum number of predicted collisions.
- 2 Minimum number of particle updates.
- 3 Efficient management of events.

5.3.1 Domain Decomposition

The first goal is achieved by dividing the original domain into an array of $l_x \times l_y$ rectangular cells of lengths l_x and l_y respectively. This technique of domain decomposition is also used in force-based molecular dynamics simulation to reduce the time consuming force calculation. In Listing 5.5 we have defined how domain decomposition is implemented. Figure 5.4 shows a typical domain decomposition picture. The benefit of domain decomposition is that calculation of collision partners of particles is confined only to the 9 neighboring boxes. This function greatly reduces the expensive calculation of particle-particle collisions and the search only confines in the neighboring boxes only.

It is also important to understand that because of the domain decomposition particles move from one cell to the other. This gives rise to another type of events called *virtual-wall crossing* (VWC) apart from regular *disk-disk collision* (DDC) events. So it is also important to keep track of those particles moving across the boxes. However during VWC, only the location of the particle in the box is updated and everything is left unaltered.

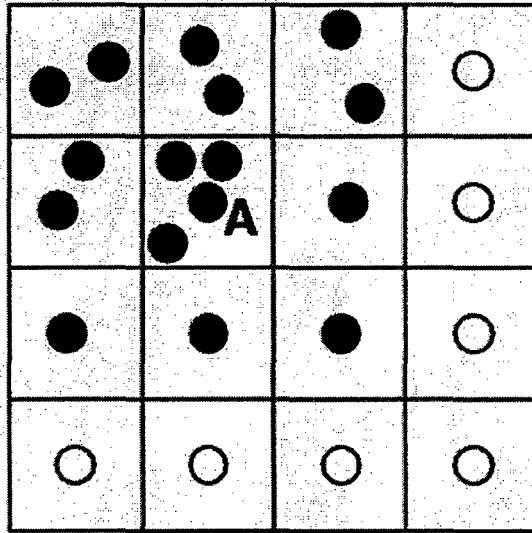


Figure 5.4: Simulation area is divided into boxes. The particle A and its neighboring particles are shown in black. Only neighboring particles are considered potential collision partners.

Listing 5.5: Neighbourhood()

```

1 // get the neighbour hood box particles for particle "disk"
  void Container:: Neighbourhood(const int &idisk )
3 {
    int cell_of_idisk[2];
5    int_clear(_MYNARR);
    const int Round = int(_NO_BOX_X);
7
    HardSphere[idisk].GetPosition(cell_of_idisk); // Locate the cell
9
    for ( int i= cell_of_idisk[0]-1; i<cell_of_idisk[0]+2; i++)
11    for ( int j= cell_of_idisk[1]-1; j<cell_of_idisk[1]+2; j++)
        int_union(_MYNARR, Cell.Box( PbcInt(i, Round), PbcInt(j, Round)) );
13
        // Ref. to Varr.h
    if (int_remove(_MYNARR, idisk))
        // Ref. to Varr.h
15    Set_MYNARR_LENGTH();
}

```

5.3.2 Asynchronous Updating

The second goal is achieved by what is known as *asynchronous updating* [2]. Apart from global time, each particle is associated with a clock (see Listing 5.1). After a collision event, only the state of the colliding particle is updated and the clock of the colliding particles is synchronized with the global time. However, the rest of the particles remain untouched. Each time when some calculations like collision time etc., need to be made, particles are propagated in space by a time step ($T_G - \tau_i$), where T_G is the global time and τ_i is the individual particle clock time.

5.3.3 Event Management

Finally, the third goal is achieved by using local event list ($local_i$), the local minima list (lml), and future event list (FEL) (see Listing 5.4). Each event (either a VWC or DDC) is stored in $local_i$, which has a data structure of that of a priority queue (see Listing 5.4 and line 30 and line 34). Other than normal data structure like array, Priority queue is very efficient and fast in handling data according to the given priority, i.e., in this case, minimum time. The events which will occur in the shortest time are picked from each $local_i$ and is placed in a local minima list (lml). The minima of lml , will be the next event to occur in the actual dynamics. However, for better management of data, the events from lml , are organized in a tournament tree, i.e., FEL . This is also the most efficient method to find the next minimum-event in the dynamics.

Figure 5.5 and Figure 5.6 show a simple 6-particle based tournament tree with construction and new entry insertion. In Listing. 5.6 and Listing. 5.7 implement the necessary details.

The tree is constructed as follows: each node has a value, which is smaller than its descendant. A pair-wise comparison is made between the particle levels according to the respective values in the *lml* list. The odd one gets promoted to next level without any comparison. The highest node contains the global minima. A typical benefit of using tournament tree is that, not only finding the global minimum time is very efficient, but also when next event will be inserted in the tree, one does not need to compare with all the events already in the tree, only a certain section of tree is needed to be scanned as shown in Fig. 5.6. Hence, finding the global minimum event speeds up massively. The implementation in code has two parts: (a) create a tournament tree, (b) update a tournament tree.

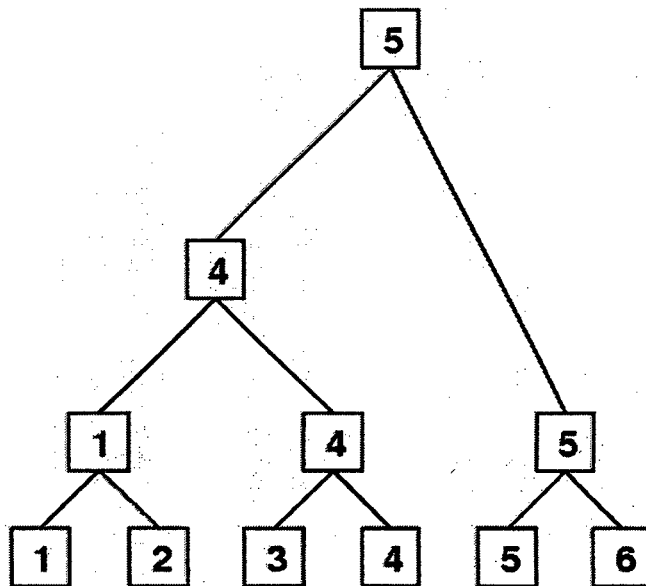


Figure 5.5: Tournament tree.

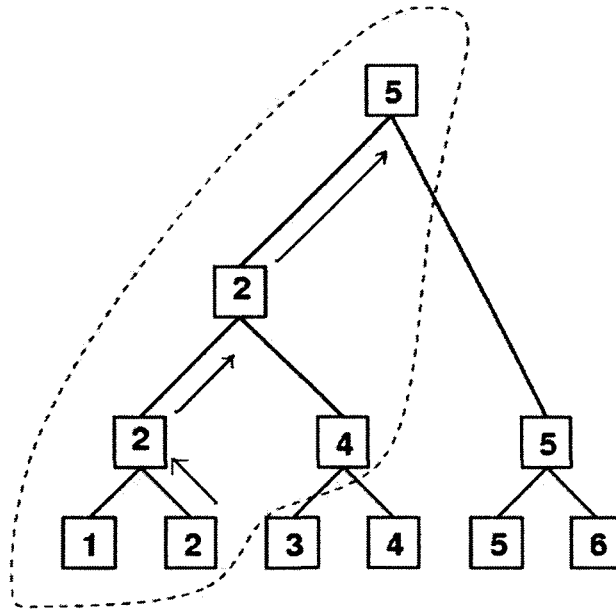


Figure 5.6: Insertion of a new event in the tournament tree. Notice that when a label (say 2 in this case) gets updated with a new entry, only a limited region (marked in dashed lines) need to scan to get the global minimum.

```

1 void Container::create_cbt()
  {
3 // This routine is used to choose the first event only
  // if the number of leaves is odd, the odd one gets promoted with no
5 // competition in the first round. Binary search tree is used

7 int fel_l= int(2*_No_Of_Particles-2);

9 // can treat arrays now as having even no of leaves

11 while(fel_l > 0)
    {
13     Event MINEVENT;
        int i =FEL[fel_l];
15     int j =FEL[fel_l-1];
        if ( MINEVENT.MIN(lml[i],lml[j] )==lml[i])
17         {

```

```

        FEL[(fel_1-2)/2] = FEL[fel_1];
19     }
    else
21     {
        FEL[(fel_1-2)/2] = FEL[fel_1-1];
23     }
        fel_1 = fel_1-2;
25 }
}

```

```

1 void Container::update_cbt(const int &disk)
{
3 // remove invalid DDC events from cbt
    if (lml[disk].Return_Event_Type() == DDC)
5     {
        if (lml[disk].Return_C() !=_C[lml[disk].Return_Partner()])
7         {
            localList[disk].event_list_remove
9            (lml[disk].Return_Scheduled_Time());

11            localList[disk].pop(); //single delete of the min value
                Item Temp;
13            Temp = localList[disk].top();
                lml[disk] = Temp;
15        }
    }
17 int cbtp = _No_Of_Particles +disk -1;

19 // cbtp is odd
    while (cbtp > 0)
21     {
        Event MINEVENT;
23     if (cbtp % 2)
        {
25     if ( MINEVENT.MIN(lml[FEL[cbtp]],lml[FEL[cbtp+1]])
            ==lml[FEL[cbtp]])
27         FEL[int(cbtp-1)/2] = FEL[cbtp];
        else
29         FEL[int(cbtp-1)/2] = FEL[cbtp+1];

```

```

        cbtp = (cbtp-1)/2;
31     }
    else
33     {
        if ( MINEVENT.MIN(lml[FEL[cbtp]],lml[FEL[cbtp-1] ] )
==lml[FEL[cbtp]])
35
        FEL[int (cbtp-2)/2] = FEL[cbtp];
37     else
        FEL[int (cbtp-2)/2] = FEL[cbtp-1];
39     cbtp = (cbtp-2)/2;
    }
41 }
}

```

5.3.4 Deletion of Invalid Events

Apart from all these improvements discussed so far, another important thing is to efficiently discard invalid events. An event become invalid in the event list, after a particle-particle collision event or when particles change boxes. Hence, after each event, the event-list (*lml*) has to be updated.

When two particles i and j collide, all entries in the event list of i and j , i.e., $local_i$ and $local_j$ become invalid. Moreover, entries in the list of other particle k also become invalid, where either i or j was one of the next potential candidates. There is a simple, but powerful trick by Martin et al. [3] to bypass the removal of such invalid entries arising out of collision by introducing a collision counter. Each particle counts the total number of collisions it was involved so far. When adding an entry for the particle-particle collision to the event list, the number of collisions in which the partner was involved so far is now stored. The entries in the collision list of i now contain the index of the partner j , the collision time, and the value of the collision counter j when the entry was recorded (see Listing 5.2). When reading the entry

in the list of the particle i , its validity can easily be checked. If the present counter value of j is larger than the number in the list of i , the entry is not valid since j has meanwhile suffered collision with other particles (see Listing 5.7 and line 6). Hence, when two particles i and j collide, there is no need to remove the entries from other particles k which may refer to either i or j . By evaluating the collision counter we avoid searching the list of invalid events. The implementation is as follows:

```

1 //1. Decides Collision type, disk, partner and
2 // returns min of Time this also do the efficient
  // time management, sort, deltion, etc., by calling
4 // one of the routines
  Double new_event(int &colltype, int &disk,
6                 int &partner, Container &Q)
  {
8     Double time=-1.0;
     bool go = true;
10
     if (disk ==-1&& partner==-1)
12 {
     //cout<<"Dynamics to be started\n";
14 Q.create_cbt(); // this function is called
     // only once after initialisation
16 }
     else
18 {
     Q.update_cbt(disk); // update disk in CBT
20 if (int(partner) >=0 && partner < int(Q._No_Of_Particles))
     // by choice for VWC events
22 // colltype set negative
     Q.update_cbt(partner); // update partner in CBT
24 }

26 do
  {
28 disk = Q.FEL[0]; // disk with highest priority
  partner = Q.lml[disk].Return_Partner(); // partner
30 colltype = Q.lml[disk].Return_Event_Type(); // type of events

```

```

time      = Q.lml[disk].Return_Scheduled_Time(); //Scheduled
32                                                    Time

34 // now 3 kind of situation may rise
// 1. a disk disk collision,
36 // 2. a wall crossing
// 3. is invalid event: which means
38 // one of the disk or partner
// had a prior collision with other disk,
40 // so the time list need
// to be updted
42
// For invalied event to occur
44 if (colltype == DDC && Q.lml[disk].Return_C()
      != Q._C[partner])
46 {
      Q.update_cbt(disk); // this to ensure
48                               that partner is particle
      }
50 else if(colltype ==DDC) //case handling
                               with disk disk collision
52 {
      Q.Event_list_AllClear(disk); //all the time
54                               list of disk invalid
      Q._C[disk]++;
56 Q.Event_list_AllClear(partner); //so for partner
                               also only in DDC mode
58 Q._C[partner]++;
      go = false; // order to leave the loop
60 }
else if(colltype ==VWC) //caes with box crossing
62 {
      Q.localList[disk].pop(); // remove only the
64                               recent box crossing evnt
      go = false;
66 }
} while(go);
68 return time;
}

```


Using the described data structure and improvements in the algorithm, the computational effort rises as $O(N \log N)$, which is a significant improvement over the original code. In this thesis, we successfully simulated $N = 2 \times 10^6$ on a workstation with a 2.0 GHz AMD cpu – 2000 collisions per particle took about 140 hours. However, the demerit of this code is that it is highly RAM demanding; in fact, memory requirement grows linearly with number of particles.

5.4 Kinetic Theory of Granular Gases

The *kinetic theory of gases* (KTG) is a novel method of extracting information about macroscopic quantities like pressure, temperature etc. from a microscopic description of many particle systems. The goal of kinetic theory is to set up Boltzmann-Enskog (BE) type equations for a particular model of interaction. The solution of these equations should give either the equilibrium state solution of the system, or it should describe the approach of the distribution function to the asymptotic state.

The classical KTG assumes the gas to be of hard spheres and type of collision is strictly elastic and instantaneous, so there is no loss of energy during evolution dynamics. This assumption enables us to derive a time-independent velocity distribution function (VDF), i.e., the Maxwell-Boltzmann (MB) velocity distribution function, which is

$$f_{MB}(\vec{v}, t) = \left(\frac{1}{\pi v_0^2}\right)^{d/2} \exp\left(-\frac{\vec{v}^2}{v_0^2}\right), \quad (5.12)$$

where, v_0^2 is defined as $v_0^2 = 2 \langle \vec{v}^2 \rangle / d$ and d is the dimensionality of the system.

The granular gas in the elastic limit (i.e., $e = 1$) quickly relaxes to the MB form of the velocity distribution. Though granular gases in the elastic limit merely behave like an ideal gas, they are inelastic by nature which renders the VDF as time dependent

of kinetic energy and average velocity. However, when $e \sim 1$, the early phase (or HCS) of the dynamics is spatially uniform state and the velocity field is also flux free. This resembles an ordinary molecular gas. The velocity distribution function is very close to Maxwellian distribution. Its deviation from Maxwell-Boltzmann statistics is characterized by coefficients of Sonine-polynomials expansion. Thus to incorporate inelastic collision for granular gas, the concept of kinetic theory needs to be suitably adjusted.

5.4.1 The Boltzmann-Enskog Equation for Inelastic Gases

The fundamental equation of KTG is the *Boltzmann-Enskog equation*, which was derived by Boltzmann, and was modified by Enskog to account for the finite volume effects in dense gas. The velocity distribution function $f(\vec{r}, \vec{v}, t) d\vec{r}d\vec{v}$ denotes the number of particles in a small phase space volume $d\vec{r}d\vec{v}$ located at $(\vec{r} + d\vec{r}, \vec{v} + d\vec{v})$ at time t . The distribution function has the following properties:

$$\int f(\vec{r}, \vec{v}, t) d\vec{r}d\vec{v} = N, \tag{5.13}$$

where N is total number of particles present in phase-space volume. For a homogeneous, force-free system, the $f(\vec{r}, \vec{v}, t)$ is translationally invariant, i.e., independent of spatial variable \vec{r} . Thus, the velocity distribution function has the following properties:

$$\int f(\vec{v}, t) d\vec{v} = \frac{N}{V} = n, \tag{5.14}$$

$$\int \vec{v} f(\vec{v}, t) d\vec{v} = n \langle \vec{v} \rangle = 0, \tag{5.15}$$

$$\int \frac{1}{2} m v^2 f(\vec{v}, t) d\vec{v} = n \left\langle \frac{1}{2} m v^2 \right\rangle = \frac{3}{2} n T(t). \tag{5.16}$$

It is evident from these equations that distribution function and its moments are related to macroscopic variables namely, temperature (T), density (n), etc.

Next we consider a collection of smooth inelastic hard discs or spheres. The interaction between two hard spheres is modeled by instantaneous collisions with abrupt change in velocities. Consider at certain time interval Δt , the number of particles in a small phase space volume ($d\vec{r}d\vec{v}$) at location (\vec{r}, \vec{v}) will change due to particle collision. After such collisions, particle in that phase space volume will move with different velocities, i.e., direct collisions result in a decrease in number of particles in that volume. However, after inverse collisions which are collisions among the particles which do not belong to that velocity range $(\vec{v}, \vec{v} + d\vec{v})$, might result an influx of particles in the phase-space volume($d\vec{r} \cdot d\vec{v}$), thereby increasing the number of particles. The Boltzmann-Enskog equation quantifies the effects of direct and inverse collisions.

Let us consider an inelastic collision (direct) between two particles i, j , hence post-collisional velocities can be written as [cf. Eq. (5.6)]

$$\begin{aligned}\vec{v}'_i &= \vec{v}_i - \left(\frac{1+e}{2}\right) [(\vec{v}_i - \vec{v}_j) \cdot \hat{n}] \hat{n}, \\ \vec{v}'_j &= \vec{v}_j + \left(\frac{1+e}{2}\right) [(\vec{v}_i - \vec{v}_j) \cdot \hat{n}] \hat{n}.\end{aligned}\tag{5.17}$$

Hence, the loss of energy in one such collision can be directly calculated as

$$\begin{aligned}\Delta E &= \frac{1}{2}m (\vec{v}'_i{}^2 + \vec{v}'_j{}^2) - \frac{1}{2}m (\vec{v}_i{}^2 + \vec{v}_j{}^2) \\ &= -\frac{1}{4}\epsilon (\vec{v}_{ij} \cdot \hat{n}),\end{aligned}\tag{5.18}$$

where $\epsilon = 1 - e^2$, is the measure of inelasticity of the system.

Next we calculate pre-collisional velocities (\vec{v}''_i, \vec{v}''_j) in terms of post-collisional

velocities (\vec{v}_i, \vec{v}_j) by inverting Eq. (5.6) to obtain

$$\begin{aligned}\vec{v}_i'' &= \vec{v}_i - \left(\frac{1+e}{2e}\right) [(\vec{v}_i - \vec{v}_j) \cdot \hat{n}] \hat{n}, \\ \vec{v}_j'' &= \vec{v}_j + \left(\frac{1+e}{2e}\right) [(\vec{v}_i - \vec{v}_j) \cdot \hat{n}] \hat{n}.\end{aligned}\quad (5.19)$$

Considering these collision rules, the BE equation can now be written [4] as

$$\begin{aligned}\frac{\partial f(\vec{v}_1, t)}{\partial t} &= g(\sigma) \sigma^{d-1} \int d\vec{v}_2 \int' d\hat{n} (\vec{v}_{12} \cdot \hat{n}) \left\{ \frac{1}{e^2} f(\vec{v}_1'', t) f(\vec{v}_2'', t) - f(\vec{v}_1, t) f(\vec{v}_2, t) \right\} \\ &= \chi \sigma^{d-1} I(f, f),\end{aligned}\quad (5.20)$$

where \hat{n} is the unit vector normal to the collision surface, σ and d are the diameter and dimensionality of the system respectively. The factor $g(\sigma)$ incorporates finite volume size effect (as suggested by Enskog) which depends on packing fraction of the system. Physically, the factor, $g(\sigma)$ accounts for an increased collision frequency due to extended volume effects. $I(f, f)$ is called the collision integral and is given by

$$I(f, f) = \int d\vec{v}_2 \int' d\hat{n} (\vec{v}_{12} \cdot \hat{n}) \left\{ \frac{1}{e^2} f(\vec{v}_1'', t) f(\vec{v}_2'', t) - f(\vec{v}_1, t) f(\vec{v}_2, t) \right\}. \quad (5.21)$$

Equations (5.20) and (5.21) also imply the restriction $\vec{v}_{12} \cdot \hat{n} > 0$ on the integral, i.e., we consider only the particles that move towards each other. The factor $(1/e^2)$ in the gain term originates following the transformation [4]

$$d\vec{v}_1'' d\vec{v}_2'' = \frac{D(\vec{v}_1'', \vec{v}_2'')}{D(\vec{v}_1, \vec{v}_2)} d\vec{v}_1 d\vec{v}_2. \quad (5.22)$$

The following scaling form has been suggested by Goldstein and Shapiro and by

Esipov and Poschel [5],

$$f(\vec{v}, t) = \frac{1}{v_T^d(t)} \hat{f}(\vec{c}), \quad (5.23)$$

where $\vec{c} = \vec{v}/v_T(t)$, and the thermal velocity $v_T(t)$ is defined as

$$T(t) = \frac{1}{2} m v_T^2(t), \quad (5.24)$$

and the temperature is defined as follows:

$$\frac{d}{2} n T(t) = n \left\langle \frac{m \vec{v}^2}{2} \right\rangle = \int d\vec{v} \frac{m v^2}{2} f(\vec{v}, t). \quad (5.25)$$

Following the scaling form in Eq. (5.23), we now try reduce the BE equation (5.20).

The LHS changes to

$$\frac{\partial}{\partial t} f(\vec{v}_1, t) = \left(-\frac{dn}{v_T^{d+1}} \tilde{f}(\vec{c}_1) + \frac{n}{v_T^d} \frac{\partial \tilde{f}}{\partial c_1} \frac{\partial c_1}{\partial v_T} \right) \frac{dv_T}{dt}. \quad (5.26)$$

Next, we try to generate a dimensionless form of the collision integral $\hat{I}(\hat{f}, \hat{f})$ in Eq. (5.21), as follows:

$$\begin{aligned} I(f, f) &= \int d\vec{v}_2 \int' d\hat{n} (\vec{v}_{12} \cdot \hat{n}) \left\{ \frac{1}{e^2} f(\vec{v}_1'', t) f(\vec{v}_2'', t) - f(\vec{v}_1, t) f(\vec{v}_2, t) \right\} \\ &= \sigma^{d-1} n^2 v_T^d v_T v_T^{-2d} \int d\vec{c}_2 \int' d\hat{n} (\vec{c}_{12} \cdot \hat{n}) \left\{ \frac{1}{e^2} f(\vec{c}_1'', t) f(\vec{c}_2'', t) - f(\vec{c}_1, t) f(\vec{c}_2, t) \right\} \\ &\equiv \sigma^{d-1} n^2 v_T^{-(d-1)} \hat{I}(\hat{f}, \hat{f}), \end{aligned} \quad (5.27)$$

where we have used, $d\vec{v} = v_T^d d\vec{c}$. The factors v_0 and v_0^{-2d} respectively arise from the length of the collision cylinder and from the product of the two distribution functions in the gain and loss terms. Finally, we write the Boltzmann equation for the scaled

velocity distribution function as

$$-\frac{1}{v_T^2} \frac{dv_T}{dt} \left(3 + c_1 \frac{\partial}{\partial c_1} \right) \tilde{f}(c_1) = g(\sigma) \sigma^{d-1} n \tilde{I}(\tilde{f}, \tilde{f}). \quad (5.28)$$

Now, with the help of Eq. (5.28), we can derive the temperature decay rate dT/dt for the inelastic granular gas. From the definition of temperature in Eq. (5.25), we can write

$$\begin{aligned} \frac{d}{dt} \left(\frac{d}{2} n T(t) \right) &= \int d\vec{v}_1 \frac{mv_1^2}{2} \frac{\partial}{\partial t} f(\vec{v}_1, t) \\ &= g(\sigma) \int d\vec{v}_1 \frac{mv_1^2}{2} I(f, f) \\ &= g(\sigma) \sigma^{d-1} n^2 v_T \frac{mv_T^2}{2} \int d\vec{c}_1 c_1^2 \tilde{I}(\tilde{f}, \tilde{f}) \\ &= g(\sigma) \sigma^{d-1} n^2 v_T T \mu_2, \end{aligned} \quad (5.29)$$

where μ_2 is the dimensionless collision integral which does not depend on time, and is defined as

$$\mu_p = - \int d\vec{c}_1 c_1^p \tilde{I}(\tilde{f}, \tilde{f}). \quad (5.30)$$

Thus the decay rate can be written as

$$\frac{dT}{dt} = -\frac{2}{d} B T \mu_2; \quad \text{and } B = v_T g(\sigma) \sigma^2 n. \quad (5.31)$$

If we put $v_T \sim \sqrt{T}$, the final form of the equation becomes

$$\begin{aligned} \frac{dT}{dt} &= -\gamma T^{3/2}, \\ \gamma &= (\sqrt{2\pi}/\Omega_d) \frac{\mu_2}{d}. \end{aligned} \quad (5.32)$$

The solution of Eq. (5.32) is

$$T(t) = \frac{T_0}{\left(1 + \frac{\gamma}{2} T_0^{1/2} t\right)^2}. \quad (5.33)$$

The solution of Eq. (5.32) can also be written as

$$T(t) = \frac{T_0}{(1 + \gamma t/t_0)^2}; \quad T(\tau) = T_0 \exp(-2\gamma\tau), \quad (5.34)$$

where τ is the number of average collisions per particle and is defined as $d\tau = \omega(T) dt$.

This is known as Haff's law for granular systems in the homogeneous cooling state. However, in late stages with formation of clusters, the assumptions of kinetic theory are no longer valid, and the system shows a departure from Haff's law [6].

5.5 Overview of Chapter 6: Our Studies of Dynamical Properties of Granular Gases

Let us conclude this chapter with a brief overview of our studies of the dynamical properties of granular gases in Chapter 6. The material presented in Chapter 6 can be divided into two parts. In the first part, we study the evolution of a monodispersed granular gas. We focus on the properties of the *homogeneous cooling state* (HCS) and the *inhomogeneous cooling state* (ICS). In this context, we draw an analogy with phase-separation dynamics of a binary mixture. We calculate different statistical quantities like the correlation function, structure factor, domain length scales, etc., which are found to be consistent with dynamical scaling.

In the second part of Chapter 6, we revisit the HCS of the freely-evolving granular gas. Real granular materials are not monodispersed – as a matter of fact, there

are many disparities between the granular particles, e.g., differences in restitution coefficients, difference in masses, difference in sizes, etc. In the second part of Chapter 6, we focus on polydispersed granular materials and study the HCS of such systems. We first present a brief overview of differential collision frequencies and differential collision rates for polydispersed hard spheres. Then, we discuss Haff's law for granular mixtures with two kinds of particles.

Bibliography

- [1] T. Poschel and T. Schwager, *Computational Granular Dynamics: Models and Algorithms*, Springer, Heidelberg.
- [2] B. D. Lubachevsky, *J. Comput. Phys.* **94**, 255 (1991).
- [3] M. Martin, D. Risso and P. Cordeo, *J. Comput. Phys.* **109**, 306 (1993).
- [4] N. V. Brilliantov and T. Poschel, *Kinetic Theory of Granular Gases*, Oxford University Press, Oxford (2004).
- [5] A. Goldstein and M. Shapiro, *J. Fluid Mech.* **282**, 75 (1995).
- [6] P. K. Haff, *J. Fluid Mech.* **134**, 401 (1983).

Chapter 6

Pattern Formation in Freely-Evolving Granular Gases

6.1 Introduction

Granular materials or powders have captured attention of scientists in recent decades [1, 2, 3, 4, 5]. These materials are of great scientific and technological importance – some properties are reminiscent of fluids whereas other properties are close to solid. Further there is a set of features which are unique to granular matter. The dynamical properties of granular systems are also of great interest. In this context, the most important characteristic of grains is that they undergo inelastic collisions. Through these collisions a granular system dissipates energy, i.e., the system is *cooled* by ongoing inter-particle interactions and finally settles into a static pile. This suggests two classes of dynamical problems for powders lows:

- (a) We can study systems when the cooling is compensated by the input energy (heating) from an external drive. There are various standard techniques of agitating a powder, e.g., rotation in a drum [6, 7, 8], horizontal and vertical

vibrations on a plate [9], pouring through a chute [10], etc. The system settles into a nonequilibrium steady state characterized by the balance between collisional energy loss and input of energy due to external forcing. Each of the above experimental situations give rise to complex pattern dynamics, which has been a subject of much interest.

- (b) Alternatively, we can study the evolution of an initially homogeneous granular system in absence of an external drive. The system loses energy continuously and finally settles into a static state. Naively, this evolution may appear to be somewhat boring and of limited scientific interest. However, this simple system shows a complex dynamical evolution enroute to its final state, and has been extensively studied in literature [11, 12, 13].

In this chapter, we focus on the dynamical problem mentioned in (b) above. First, let us briefly review the phenomenology observed in the system. At time $t = 0$, the particles are homogeneously distributed in space with (say) a Maxwell-Boltzmann (MB) distribution of velocities. The system evolves without any external drive, thereby losing energy due to inelastic granular collisions. In the initial stages, the density and velocity fields remain approximately uniform and the system evolves in a *homogeneous cooling state* (HCS). However, the uniform density and velocity fields are destabilized by long wave-length fluctuations, and the system crosses over into an *inhomogeneous cooling state* (ICS). The density field in the ICS is characterized by the emergence and growth of particle-rich clusters in conjunction with regions which are depleted in particles. There is also corresponding emergence of structures in the velocity field.

In this context, we mention the important work of Das and Puri (DP) [14] on domain morphologies of granular systems and the work of Ahmad and Puri (AP) [15]

on velocity distributions of granular systems. In particular, Ref. [14] has made the analogy between the ICS and a phase ordering system, i.e., the dynamical evolution of a two-component mixture which has been rendered thermodynamically unstable by a rapid quench below the critical temperature (see Chapter 1). The simulation results had been obtained with relatively small 2-dimensional system (upto $N = 0.4 \times 10^5$, where N is the number of particles). In this chapter, we revisit these problems with present-day computational techniques. We study a much larger systems (upto $N = 2.56 \times 10^6$) upto later times in dimensionalities $d = 2, 3$. This enables us to sharpen the analogy between the evolution of the ICS and that of a phase-separating system. The comprehensive molecular dynamics (MD) simulations reported here enable us to make conclusive statements about pattern dynamics in the ICS. These results will be of great utility to theorists and experimentalists interested in this problem.

This chapter is organized as follows. In Sec. 6.2, we provide the theoretical background for studying this problem. In Sec. 6.3, we provide detailed numerical results for morphologies and other properties of the HCS and ICS of a granular gas. In Sec. 6.4, we study the HCS for polydispersed granular materials. In Sec. 6.5, we present a summary and discussion of our results.

6.2 Theoretical Background

6.2.1 Haff's Law in Monodispersed Systems

The HCS was first studied by Haff [13], and it corresponds to a state with uniform density and temperature, and a coarse-grained velocity field which is identically zero. We consider a monodispersed (i.e., all grains are identical) and isotropic granular gas

with N particles and volume V , the number density being $n (= N/V)$. The system has no external force and the grains move irregularly with randomly distributed velocities. The temperature is defined as

$$\frac{d}{2}T = \left\langle \frac{1}{2}m\bar{v}^2 \right\rangle, \quad (6.1)$$

where m is the mass of a grain, and $\langle \bar{v}^2 \rangle$ is the squared average of the granular velocity distribution, and d is the dimensionality of the system. The average velocity of the particles is set to zero (i.e., $\langle \bar{v} \rangle = 0$) to avoid any macroscopic flows in the system. The dynamics is governed by a series of inelastic collisions between the granular grains, which causes continuous energy decay. However in the first stage of the dynamics, density remains uniform and homogeneity of the system is preserved.

The coefficient of restitution relates particle velocities before and after collisions. Hence, the velocity update rule is [see Eq. (5.6)]

$$\begin{aligned} \vec{v}'_i &= \vec{v}_i - \left(\frac{1+e}{2} \right) [(\vec{v}_i - \vec{v}_j) \cdot \hat{n}] \hat{n}, \\ \vec{v}'_j &= \vec{v}_j + \left(\frac{1+e}{2} \right) [(\vec{v}_i - \vec{v}_j) \cdot \hat{n}] \hat{n}, \end{aligned} \quad (6.2)$$

where \hat{n} is the unit vector parallel to the relative position of the particles, and $e (< 1)$ is the coefficient of restitution. In a hard-sphere collision model, the colliding grains are considered as perfectly smooth. Hence, the radial components of velocities of the colliding particles get updated, and the tangential components remain unaffected.

The loss of energy between the colliding particles can easily be calculated from

Eq. (6.2):

$$\begin{aligned}\Delta E &= E_f^n - E_i^n \\ &= \frac{1}{2} \left[-\frac{(1-e^2)}{2} v_{in}^2 - \frac{(1-e^2)}{2} v_{jn}^2 + (1-e^2) v_{in} v_{jn} \right].\end{aligned}\quad (6.3)$$

Here, v_{in} and v_{jn} are normal component of velocities of i^{th} and j^{th} particles.

Now taking average over all possible directions of the incident velocities, we finally obtain

$$\begin{aligned}\Delta E &= -\frac{1}{2} (1-e^2) \frac{\langle \bar{v}^2 \rangle}{d} \\ &= -\frac{\epsilon}{d} E.\end{aligned}\quad (6.4)$$

where d is the dimensionality and $\epsilon (= 1 - e^2)$ is called the *degree of inelasticity*.

So the average energy loss in time dt is

$$dE = -\frac{\epsilon}{d} E \omega(T) dt, \quad (6.5)$$

where $\omega(T)$ is the collision rate among hard sphere particles, given by [see Sec. 6.4.1]

$$\omega(T) = \omega(T_0) \sqrt{\frac{T}{T_0}}. \quad (6.6)$$

Here $\omega(T_0)$ is a constant rescaled with the initial temperature T_0 . Hence, the differential equation for temperature relaxation in a granular system can be written as

$$\frac{1}{T_0} \frac{dT}{dt} = -\frac{\epsilon}{d} \omega(T_0) \left(\frac{T}{T_0} \right)^{3/2} dt. \quad (6.7)$$

The solution of this equation leads to

$$T(t) = T_0 \left(1 + \frac{\epsilon \omega(T_0)}{2d} t \right)^{-2}. \quad (6.8)$$

Equation (6.8) is known as Haff's law for dilute granular system. However, Haff's law is generally expressed in terms of average collision number (τ), which is also more natural choice instead of real time t . For homogeneous granular system, average collision number τ can be written as

$$\tau = \int dt \omega(T) \quad (6.9)$$

and, using Eq. (6.7) and Eq. (6.8), $\omega(T)$ is given by

$$\omega(T) = \frac{\omega(T_0)}{\left(1 + \frac{\epsilon \omega(T_0)}{2d} t \right)}. \quad (6.10)$$

Thus, we have

$$\begin{aligned} \tau &= \int dt \left[\frac{\omega(T_0)}{\left(1 + \frac{\epsilon \omega(T_0)}{2d} t \right)} \right] \\ &= \frac{2d}{\epsilon} \ln \left(1 + \frac{\epsilon \omega(T_0)}{2d} t \right). \end{aligned} \quad (6.11)$$

Finally, Eq. (6.7) can be written in terms of the variable τ as

$$\frac{dT}{d\tau} = -\frac{\epsilon}{d} T, \quad (6.12)$$

which can be integrated and the final form of Haff's law is

$$T = T_0 \exp\left(-\frac{\epsilon}{d}\tau\right). \quad (6.13)$$

The Haff's law for the HCS was confirmed in $d = 1$ MD simulations by McNamara and Young [16], and Sela and Goldhirsch [17]; and in $d = 2$ MD simulations by Goldhirsch and co-workers [18], McNamara and Young [19], Luding et al. [20], and Luding and Herrmann [21]. In particular, Luding et al. [20], considered collisions of rough granular particles in $d = 2$, and confirmed that Haff's law applies for both translational and rotational energies. In Fig. 6.1, we show Haff's law for 2- d and 3- d systems.

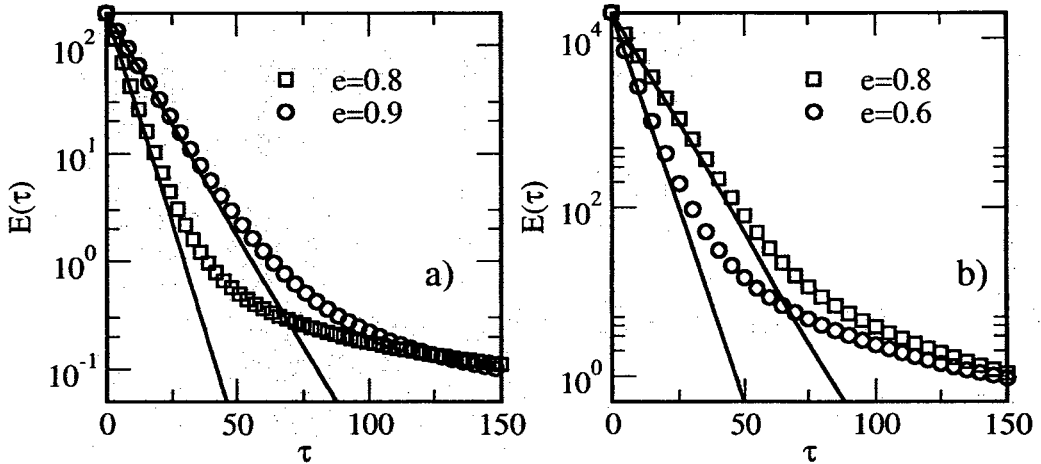


Figure 6.1: (a) Time-dependence of the granular temperature in $d = 2$, shown on a linear-log scale. The initial energy of the system is set to value 200 (in dimensionless unit). The coefficients of restitution's are $e = 0.8, 0.9$. The solid line is the theoretical plot as in Eq. (6.13). (b) Similar to the plot in (a), time-dependence of the granular temperature in $d = 3$ is shown. The initial energy is set to the value 20000 and coefficients of restitution are $e = 0.6, 0.8$. Notice that at par with Eq. (6.13), the energy decay rate in HCS is smaller in 3 d , i.e., the slope ϵ/d is smaller in 3- d than in 2- d . The departure from the theoretical curve marks the onset of ICS.

6.2.2 Formation of Clusters

The above picture is only valid for the early stage of the cooling process, i.e., as long as the system remains approximately homogeneous. Figures 6.2 and 6.3 show the evolution of the density and velocity fields for a $d = 2$ and $d = 3$ granular gas, respectively.

We see that the density field undergoes spontaneous clustering, and large-scale structures emerge in the velocity field (cf. Sec. 5.1.1). It is known that initial small fluctuations in the density field are highly unstable to pressure instability, which result in formation of clusters. The nature of these instabilities can be clarified by a linear stability analysis of the corresponding nonlinear hydrodynamics equation. A detailed discussion of the instabilities has been given by Brito and Ernst [22] and van Noije and Ernst [23]. The dynamics in the velocity field is driven by a long-wavelength instability in the shear mode for wave-vectors $k < k_{\perp}^c(\epsilon) \sim \sqrt{1 - e^2}$ for $e \rightarrow 1$. Similarly, clustering in the density field is driven by long-wavelength (small- k) instabilities in the heat mode. The critical wave-vectors for heat mode is denoted as $k_H^c(\epsilon)$, and satisfies $k_H^c(\epsilon) < k_{\perp}^c(\epsilon)$. Again, we have $k_H^c(\epsilon) \sim \sqrt{1 - e^2}$ for $e \rightarrow 1$. Thus, the system size L determines the instabilities which are observed:

- (a) For $L < 2\pi/k_{\perp}^c(\epsilon)$, there is no pattern formation in either the velocity or density fields. In this case, the system always remains in the HCS.
- (b) For $2\pi/k_{\perp}^c(\epsilon) < L < 2\pi/k_H^c(\epsilon)$, the system is characterized by vortex formation in the velocity field but no density inhomogeneities are formed. Again the system remains in the HCS for all time.
- (c) For $2\pi/k_H^c(\epsilon) < L$, the granular gas exhibits both vortex formation and clustering.

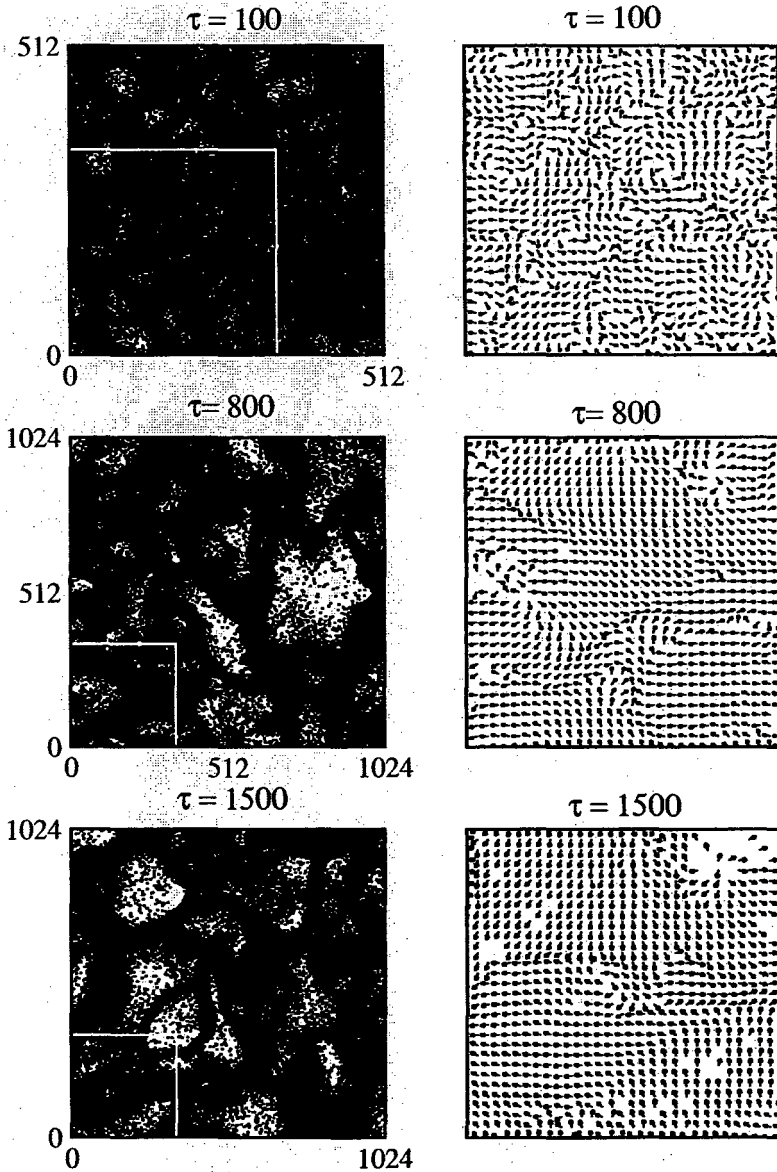


Figure 6.2: Evolution pictures of density field (left frame) and corresponding velocity field (right frame) for $d = 2$ granular gas. The collision times are $\tau = 100, 800, 1500$, density is $n = 0.3$, system size $L_x = 2896$ and restitution coefficient $e = 0.9$. The velocity field is obtained by coarse-graining the system into boxes of size $(5.66\sigma)^2$. The velocity field plotted in the right frame corresponds to the cluster regions marked by the white square in the left frame. Presence of vortices and anti-vortices can be seen in the early time snapshots, which coarsen with time and local parallelization of fields can also be observed in the late stage dynamics.

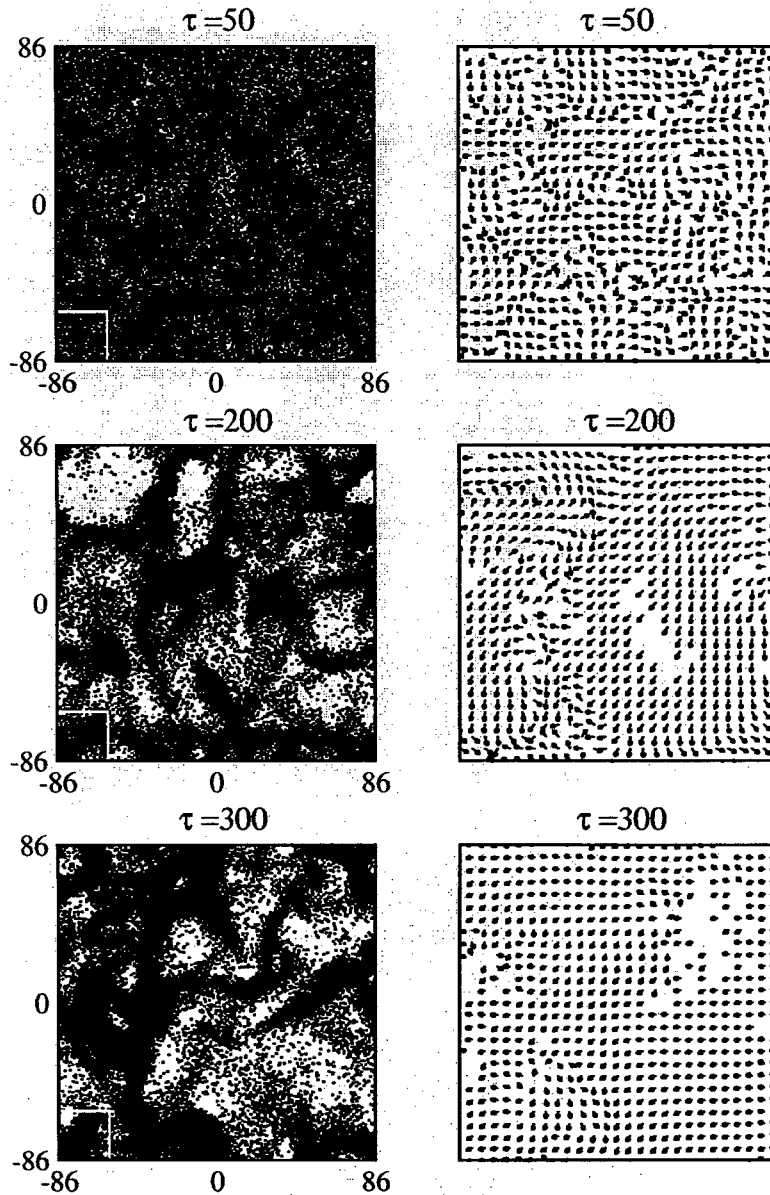


Figure 6.3: Evolution pictures similar to Fig. 6.2: The density field (left frame) and corresponding velocity field (right frame) for $d = 3$ granular gas is shown. The collision times are $\tau = 50, 200, 300$, density is $n = 0.4$, system size $L_x = 172$ and restitution coefficient $e = 0.8$. Here we show a slice of XY -plane at $z = 0$ and the thickness of the slice is 2.69σ . The velocity field is obtained by coarse-graining the slice into boxes of size $(2.69\sigma)^2$ and taking the projection of the velocity vector onto the XY -plane at $z = 0$. The velocity field plotted in the right frame corresponds to the cluster regions marked by the white square in the left frame. Presence of vortices and anti-vortices can also be seen in the early time snapshots, which coarse with time and local parallelization of fields can also be observed in the late stage dynamics.

The time-scale of the shear instability is considerably faster than that of the heat mode. Thus, there is a regime of vortex-mediated dynamics in the HCS before the crossover to ICS. Here, we are interested in the thermodynamic limits with $L \rightarrow \infty$, where the asymptotic state of the granular gas is the ICS. Das and Puri [14], have studied pattern dynamics in the non-linear ICS regime. They have drawn analogies between the clustering process in granular gases and phase-separation kinetics in binary mixtures. DP characterize pattern formation in the velocity and density fields viz. the domain growth laws, and scaling behavior of the time-dependent correlation functions and structure factors. DP argued that the *streaming and aggregation* dynamics of the granular gas results in conservation on the cluster length scale, which diverges with time. Thus, the asymptotic dynamics obeys a global conservation law, which is much weaker constraint than a local conservation law. In related work, Wakou et al. [24] have demonstrated that the evolution of the granular flow field can be described via a time dependent Ginzburg-Landau equation for a nonconserved order parameter.

6.3 Detailed Numerical Results

We characterize the dynamical evolution of the granular gas using various statistical quantities, e.g., equal-time correlation functions and structure factors for the coarse-grained density and velocity fields, domain growth laws for the characteristic length scales of the density and velocity fields, two-time aging. These are calculated as an average over eight independent runs. We consider systems with $N = 2.56 \times 10^6$ and number density $n \simeq 0.3$ and 0.4 in dimensionalities $d = 2$ and 3 , respectively.

6.3.1 Homogeneous Cooling State and Crossovers

We first briefly revisit HCS and the HCS \rightarrow ICS crossover. Figures 6.1(a) and (b) plot $\ln[E(\tau)]$ vs τ in $d = 2, 3$ dimensions. The initial exponential decay corresponds to Haff's cooling law, and the solid lines have slopes $-\epsilon/d$. There is a crossover time τ_c , after which Haff's law does not apply and the cooling rate becomes slower. The crossover time is defined as the point of deviation from Haff's law, i.e., where the data points no longer lie on the corresponding solid line. Brito and Ernst use mode-coupling techniques [22] to obtain the asymptotic energy decay (in the ICS) as

$$T(\tau) \approx \frac{T_0}{2n} \left(\frac{d-1}{\xi^d} + \frac{1}{\xi^d} \right) \left(\frac{4\pi\epsilon}{d} \tau \right)^{-d/2} \quad (6.14)$$

Figures 6.4(c) and (d) demonstrate the validity of this asymptotic expression by plotting $\ln[E(\tau)]$ vs $\ln \tau$. Notice that the asymptotic cooling behavior is consistent with $E(\tau) \sim \tau^{-1}$ in $d = 2$ and $E(\tau) \sim \tau^{-3/2}$ in $d = 3$ as per Eq. (6.14). Figure 6.5 explores the relation between real time t and the collision time τ . In HCS the dependence between real time t and average collision time τ is quite straightforward. In fig. 6.5(a) and fig. 6.5(c) we plot τ vs. t in the Haff's regime for $d = 2, 3$. The solid line is the theoretical plot of Eq. 6.11. Early time data matches with theoretical prediction and it deviates as soon as the system crossover from HCS \rightarrow ICS. We also plot τ vs. t in the ICS, shown in fig. 6.5(b) and fig. 6.5(d). Although our numerical results suggests a linear behavior in ICS, we still need a clear analytical arguments for comprehensive understanding of these fact.

2d

3d

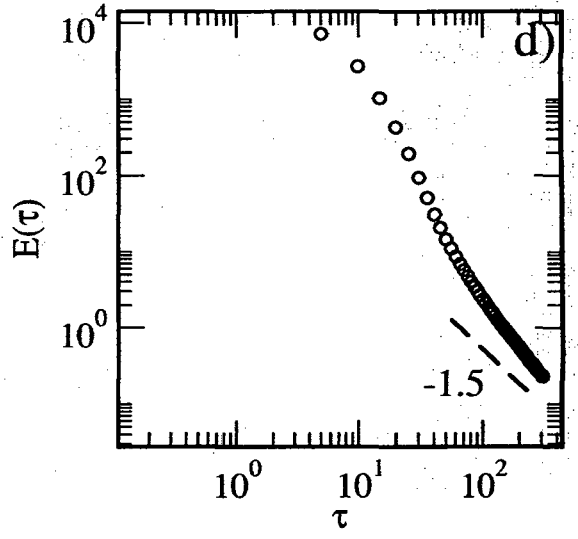
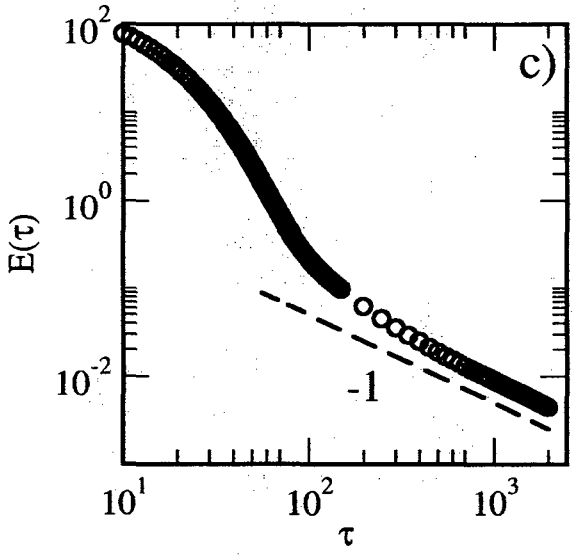
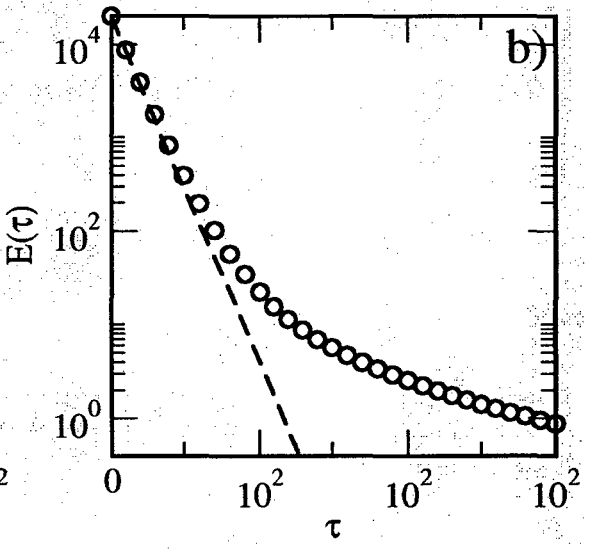
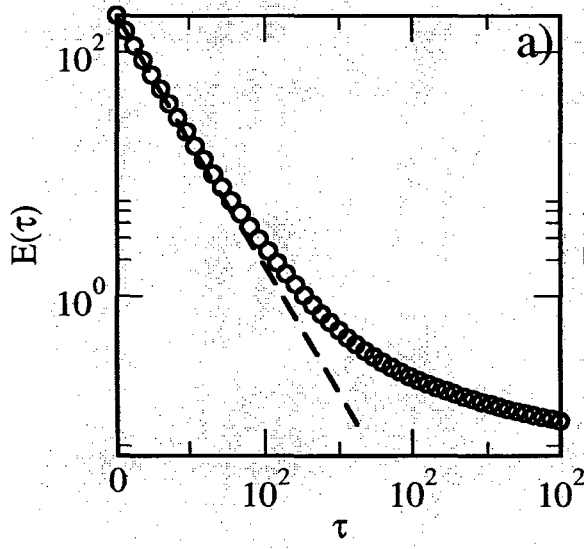


Figure 6.4: (a) and (b) Plot of Haff's law as $\ln[E(\tau)]$ vs τ in $d = 2, 3$ dimensions. We present data for $n = 0.3$ and $e = 0.9$ in 2-d and for 3-d, $n = 0.4$ and $e = 0.6$. The initial decays follows Haff's law shown by the dashed-line. (c) and (d) are $\ln[E(\tau)]$ vs. $\ln \tau$ plots for the same parameter values as in (a) and (b).

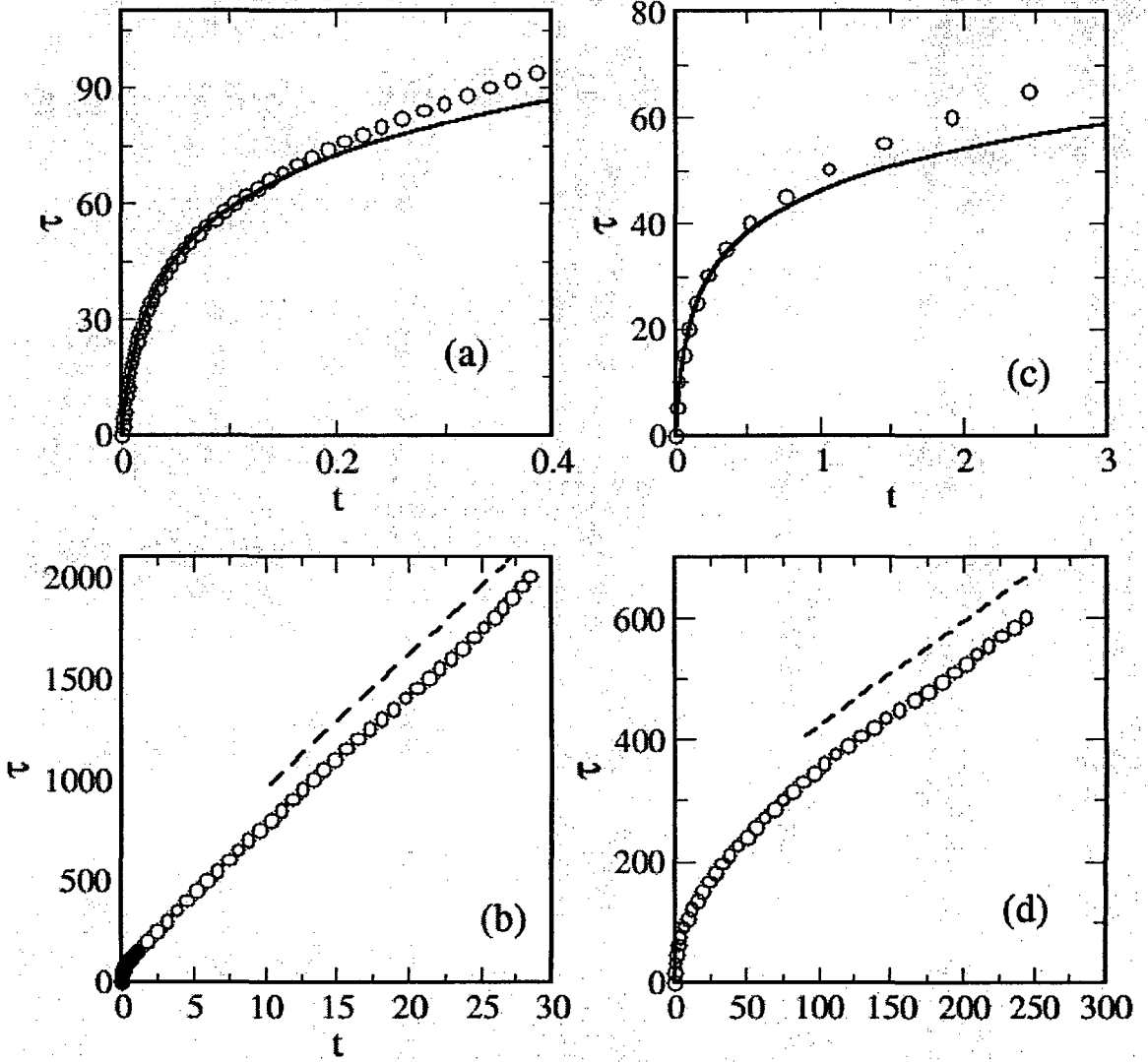


Figure 6.5: (a) and (c) Plot of τ vs t in $d = 2, 3$ dimensions respectively. We present data for $n = 0.3$ and $e = 0.9$ in 2- d and for 3- d , $n = 0.4$ and $e = 0.6$. The shown by the solid line is the theoretical prediction of Eq.6.11. (c) and (d) are τ vs. t plots in ICS. The data indicates a linear dependencies.

6.3.2 Inhomogeneous Cooling State

Next we focus on the asymptotic state of the evolution dynamics. Figures 6.2 and 6.3 are quite similar to the pattern formation as shown in Fig. 1.4, though the underlying mechanisms are quite different. In the case of granular gases, segregation arises in a purely dynamical context due to the reinforcement of density fluctuations arising from higher collision frequency in regions of higher density. Domain morphologies (self-similar pattern) also suggest that the evolving system is characterized by a domain length scale, which grows with time similar to the case of phase-separating mixtures. Thus, we expect the correlation function and structure factor to exhibit the dynamical-scaling property [cf. Eq. (1.56)]:

$$\begin{aligned} C(r, \tau) &= f\left(\frac{r}{L}\right), \\ S(k, \tau) &= L^d g(kL). \end{aligned} \tag{6.15}$$

We consider the coarse-grained density fields and velocity fields in the calculation of spatial correlation function and structure factor. In Fig. 6.6, particles and corresponding coarse-grained density field are shown. The coarse-grained density field is obtained by dividing the space into small boxes. Then we count number of particles in such unit boxes and associate a local density with that. Notice that for a homogeneous system, local density in any arbitrary place is equivalent to the density of the system. However, this is unlikely the case when system exhibit clusters (i.e., ICS phase). Therefore if local density $n(r)$ at any position is greater than the homogeneous density (i.e., N/V), we measure fluctuations in the density field $\psi(r)$ as +1 and we set $\psi(r) = -1$ otherwise.

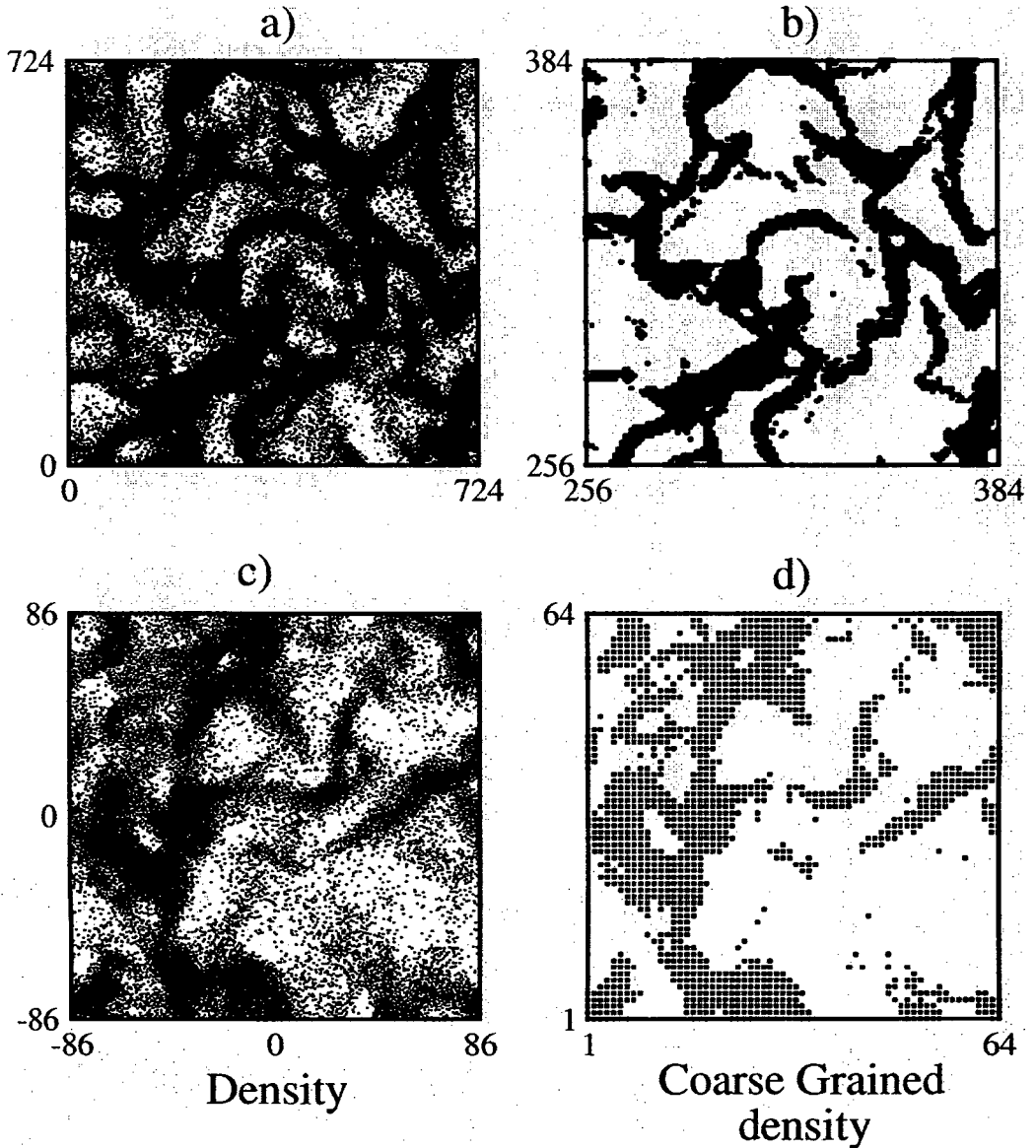


Figure 6.6: Particle and density field representation of granular gas. (a) is particle position in 2- d and (b) is corresponding coarse-grained density field. The system size is $L_x = 2896$, density $n = 0.3$, $e = 0.9$. The coarse grained unit length is $r = 11.3135$. Thus the position-space is reduced to a 256^2 coarse-grained lattice. Similar picture follows for 3- d granular system. (c) is a slice in (x, y) -plane at $z = 0$. The system size is $L_x = 172$, density $n = 0.4$, and $e = 0.8$. (d) Coarse-grained counterpart. For 3- d we use $r = 2.6875$, which reduce the density field to 64^3 lattice.

6.3.3 Correlation Functions and Structure Factors

Figures 6.7 and 6.8 demonstrate the dynamical-scaling property of the correlation function. Figure 6.7(a) superposes a 2- d simulation data for $C(r, \tau)/C(0, \tau)$ vs. r/L of the density field. The characteristic length L is defined as the distance over which the correlation function decays to 0.1 times its maximum value at $r = 0$. Figure 6.7(b) is the similar plot of correlation functions for the velocity fields. In Figs. 6.8(a) and (b) we present equivalent results from the 3- d simulations. The data collapse is reasonable suggesting that a single length scale $L(\tau)$ governs the evolution.

Figures 6.9 and 6.10 shows dynamical scaling of structure factor. Similar to phase-ordering dynamics, the nature of defects in the ordering system determines general properties of the structure factor. The presence of m -component defects (e.g., vortices in $d = 2$ and $m = 2$ or monopoles in $d = 3$ and $m = 3$) yields a power law or *generalized Porod* tail for the scaled structure factor, i.e., $f(p) \sim p^{-(d+m)}$ as $p \rightarrow \infty$] [25], which can be seen in Fig. 6.9(a)-(b) and Fig. 6.10(a)-(b).

Next, let us investigate the time-dependence of the cluster length scale. Figures 6.11 and 6.12 plot $\ln[L(\tau)]$ vs. $\ln \tau$ in $d = 2, 3$ dimensions respectively. In the early time regime (i.e., HCS) there is no growth of length scale, then there is a crossover to the ICS, where the cluster scale grows with time. In related work, Luding and Hermann (LH) [26] estimated the time dependence of average cluster size (for $d = 2$): $L(t)$ with a power law growth $L(t) \sim t^\theta$, where $\theta \simeq 0.3$. On the other hand, DP [14] found growth exponent for $d = 2$ as $\theta = 0.5$. However, our simulation indicates a universal scaling form of the growth law for both $d = 2, 3$ and the exponent obtained is $\theta = 0.33$.

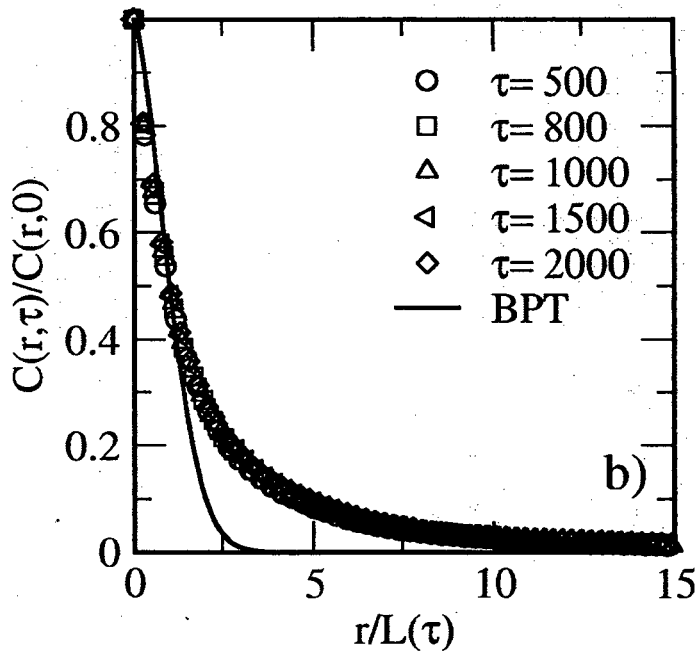
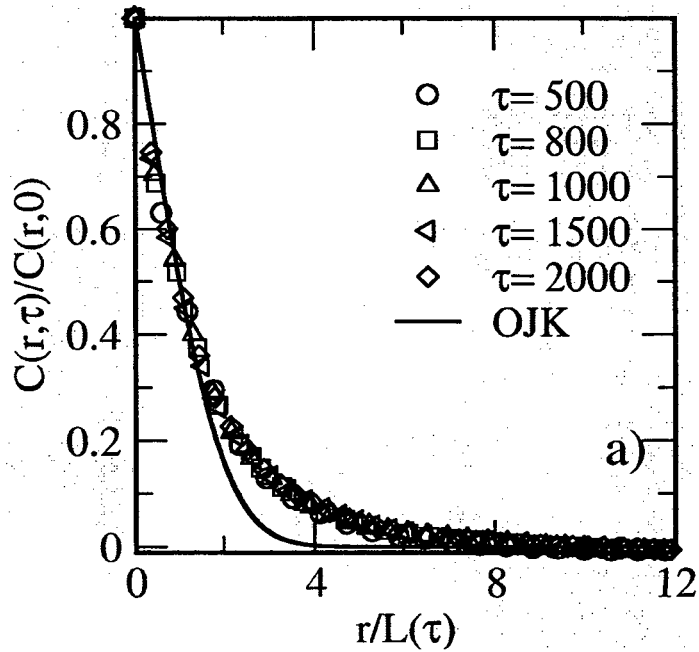


Figure 6.7: (a) Dynamical scaling of correlation function $C(r, \tau)$ of the coarse-grained density field for a 2- d granular system. (b) Analogous to (a), but for the coarse-grained velocity fields. We superpose data for different times $\tau = 500, 800, 1000, 1500, 2000$. The coefficient of restitution $e = 0.9$. The solid line in (a) is the OJK correlation function (see Sec. 1.4.5). In (b), we plot the 2-component Bray-Puri-Toyoki or BPT function [25].

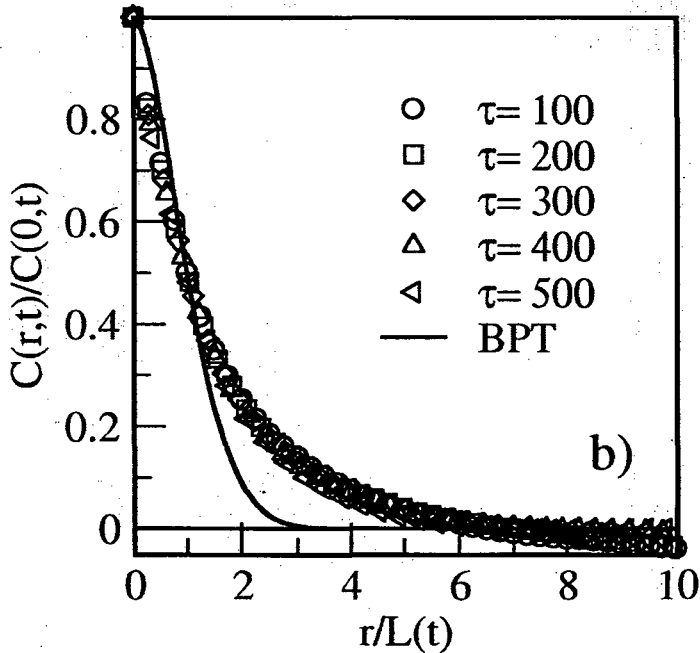
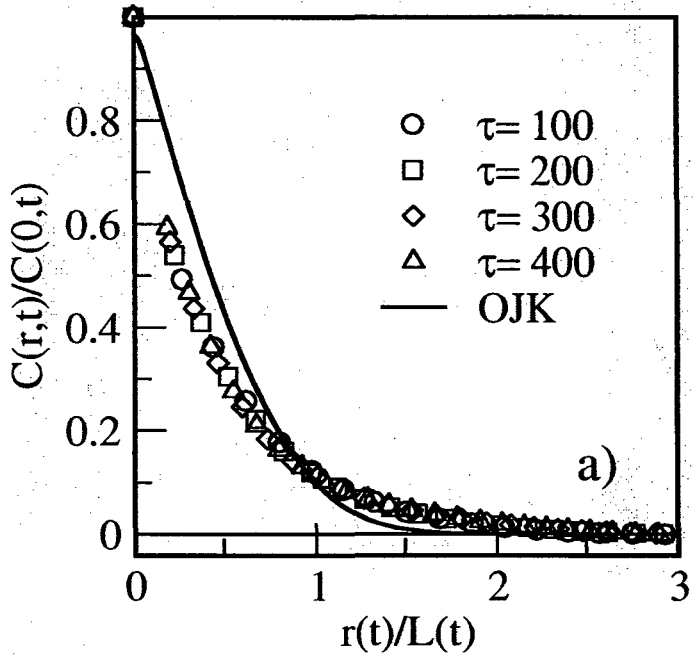


Figure 6.8: (a) Similar to Fig. 6.7, scaling of correlation function $C(r, \tau)$ of the coarse-grained density field for a 3- d granular system. (b) Analogous to (a), but for the coarse-grained velocity fields. We superpose data for different times $\tau = 100, 200, 300, 400$. The coefficient of restitution $e = 0.7$. The solid line in (a) is OJK correlation function (see Sec. 1.4.5). In (b), we plot the 3-component BPT function [25].

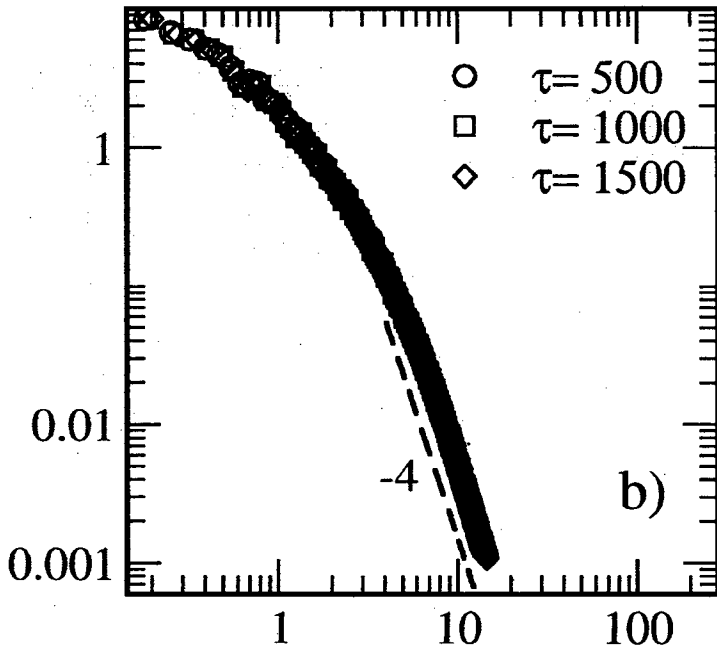
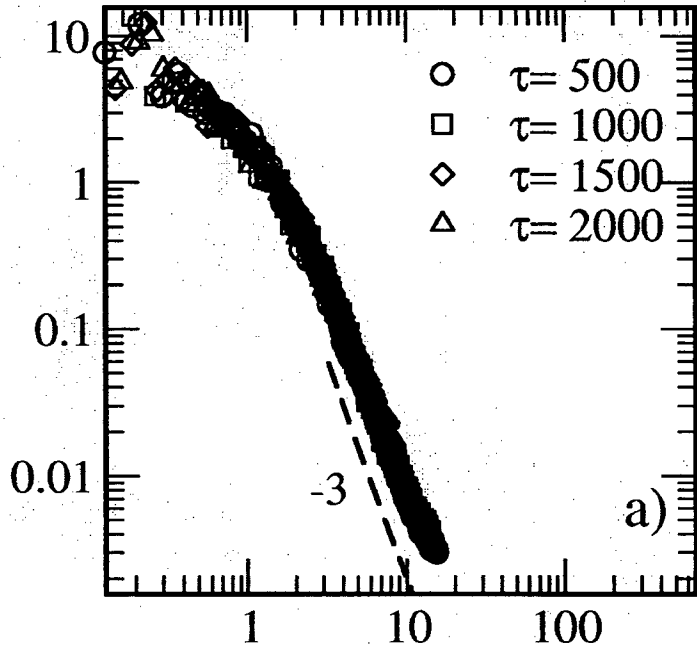


Figure 6.9: (a) Scaled structure factors for the coarse-grained density field in 2- d granular gas for parameters $n = 0.3, e = 0.9$. Data is plotted for $\tau = 500, 1000, 1500, 2000$. (b) Analogous to (a), but for coarse-grained velocity field.

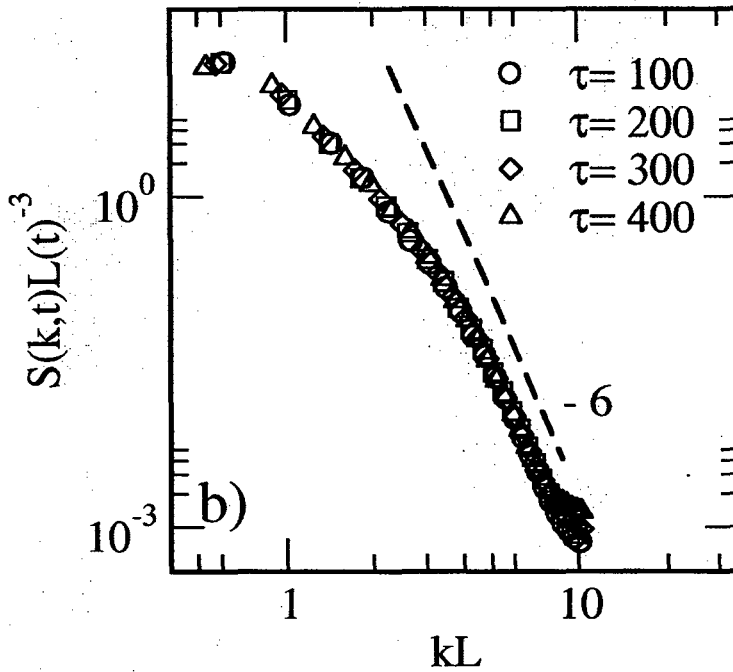
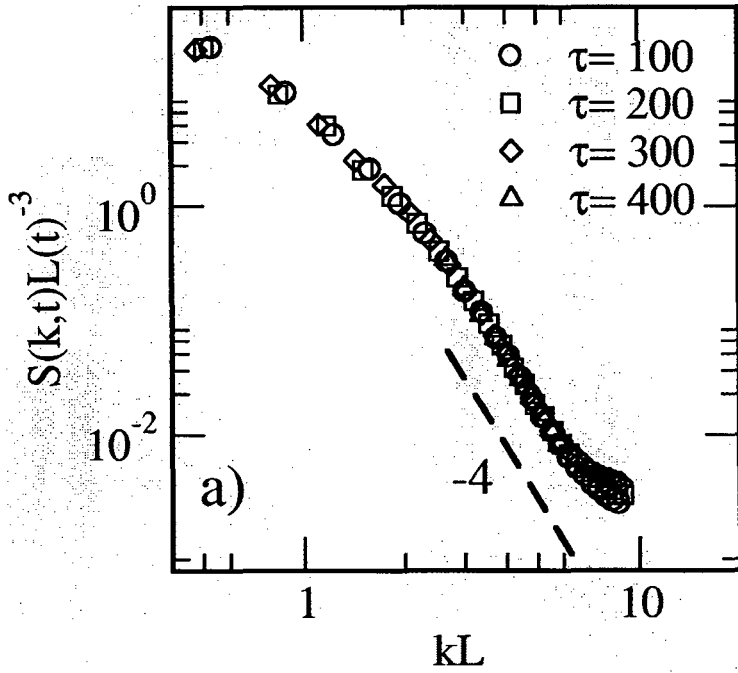


Figure 6.10: (a) Scaled structure factors for the coarse-grained density field in 3- d granular gas for parameters $n = 0.4, e = 0.8$. Data is plotted for $\tau = 100, 200, 300, 400$. (b) Analogous to (a), but for coarse-grained velocity field.

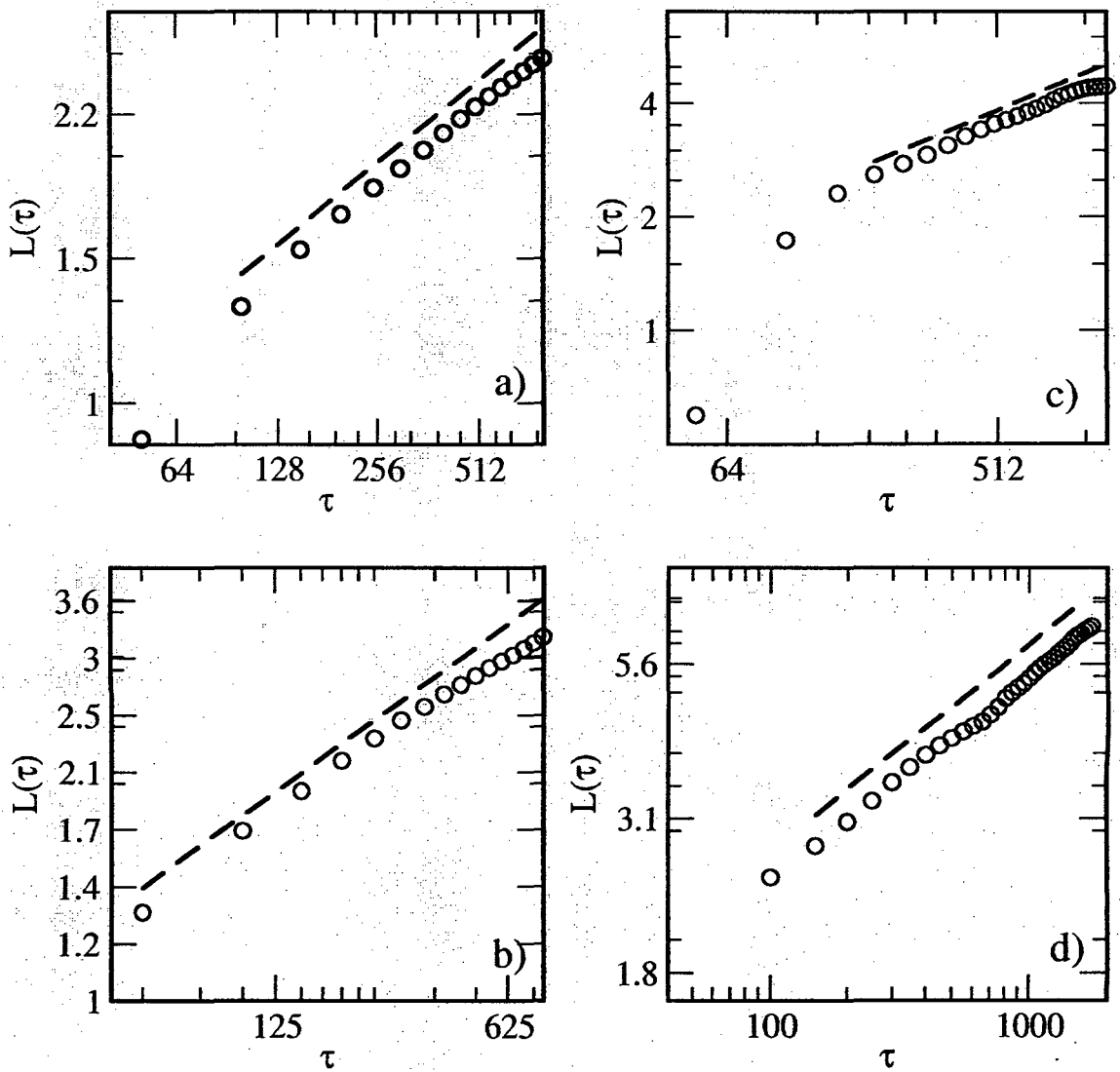


Figure 6.11: Plot of $\ln[L(\tau)]$ vs. $\ln \tau$ in $d = 2$. The characteristic length scale $L(\tau)$ is obtained from the correlation-function data. We present data for $n = 0.3$ and $e = 0.8, 0.9$. (a) Shows growth law of density field for $e = 0.8$, and (b) corresponding growth in the velocity field. Similarly, (c) and (d) present growth laws for density field and velocity field for $e = 0.9$. The dashed line has slope $\theta = 0.33$.

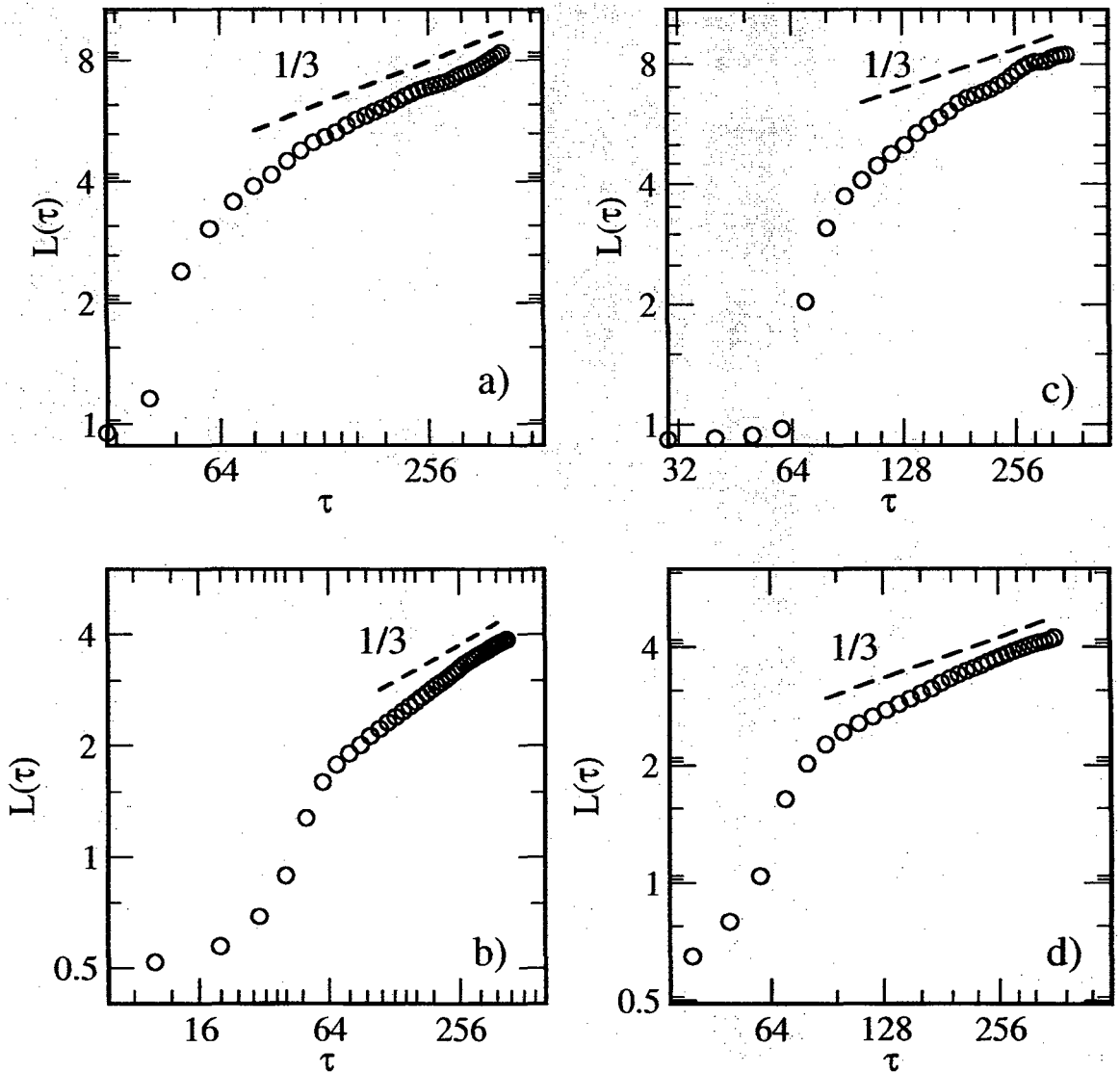


Figure 6.12: Plot of $\ln[L(\tau)]$ vs. $\ln \tau$ in $d = 3$. The characteristic length scale $L(\tau)$ is obtained from the correlation function data. We present data for density $n = 0.4$. (a) Shows growth law of density field for $e = 0.7$, and (b) corresponding growth in the velocity field. Similarly, (c) and (d) present growth laws for density field and velocity field for $e = 0.9$. The dashed line has slope $\theta = 0.33$.

6.3.4 Aging in Granular Gases

In Chapter 4, we have studied aging phenomena or two-time autocorrelation function in the context of domain growth in a ferromagnetic system. The nonequilibrium evolution of the granular gases also gives rise to an aging or non-stationary behavior of the autocorrelation function, which we will discuss here.

As we have discussed earlier, granular gases are dissipative systems. They lose energy through successive inelastic collisions. During such collisions, the normal component of the relative velocity is diminished by a factor e (coefficient of restitution) and kinetic energy is continuously lost by the system, however parallel component of the relative velocity remains intact. This results in the local parallelization of the particle velocities (see Figs. 6.2 and 6.3). The correlated motion of particles results in the formation of regions where collision rates are different. Regions with more collisions cool faster and, hence, temperature and pressure gradients are formed. We have already quantified various aspects of the cluster formation through study of spatial correlation functions, structure factors, and length scale. Another physically relevant quantity is the autocorrelation function, which is defined as,

$$A(t_w, t) = \frac{1}{V} \int d\vec{R} \left[\langle \vec{\psi}(\vec{R}, t_w) \cdot \vec{\psi}(\vec{R}, t) \rangle - \langle \vec{\psi}(\vec{R}, t_w) \rangle \cdot \langle \vec{\psi}(\vec{R}, t) \rangle \right]. \quad (6.16)$$

where t_w is referred to as the *waiting time* or the age of the system. For an stationary system, the corresponding autocorrelation function depends only on the time interval $(t - t_w)$. For nonequilibrium systems, this quantity explicitly depend upon t_w and t . The known scaling form of the autocorrelation function can be written as

$$A(t_w, t) = h \left(\frac{t - t_w}{t_w} \right). \quad (6.17)$$

In this section, we are more interested in the velocity autocorrelation function which can be defined as [see Eq. (6.16)]

$$A(t_w, t) = \frac{1}{N} \sum_{i=1}^N \langle \vec{v}_i(t_w) \cdot \vec{v}_i(t) \rangle, \quad (6.18)$$

where we have used the fact that the system has zero overall momentum, i.e., $\sum_i \vec{v}_i(t) = 0$. Note that for granular system it is more reasonable to work with collision time τ , instead of the real time t . Hence, Eq. (6.18) can be written as

$$A(\tau_w, \tau) = \frac{1}{N} \sum_{i=1}^N \langle \vec{v}_i(\tau_w) \cdot \vec{v}_i(\tau) \rangle. \quad (6.19)$$

Analytical calculation of the quantity $A(\tau_w, \tau)$ is possible for HCS [27], and it obeys

$$\begin{aligned} A(\tau_w, \tau) &= A(\tau_w, \tau_w) \exp \left[-\frac{(1+e)}{2d} (\tau - \tau_w) \right] \\ &= dT_0 \exp \left(-\frac{\epsilon}{d} \tau_w \right) \exp \left[-\frac{(1+e)}{2d} (\tau - \tau_w) \right]. \end{aligned} \quad (6.20)$$

However at later times, the decay becomes slower than exponential as velocity correlations build up prior to the ICS. let us now focus on the decay of the autocorrelation function in the asymptotic state (i.e., $\tau \gg 0$). In this context, it is relevant to discuss the results obtained by Ahmad and Puri (AP) [28]. They had shown that $A(\tau_w, \tau)$ does not exhibit the scaling form as in Eq. (6.17). Instead data set is fits in an empirical form

$$f(\tau) = [1 + a(\tau - \tau_w)]^{-1}, \quad (6.21)$$

where a is a fitting parameter which depends on τ_w .

Figures 6.13 and 6.14 present our MD simulation data for autocorrelation function in $d = 2, 3$. We also use Eq. (6.21). Our 2- d simulation data shows excellent fit with the Eq. (6.21) for different values of e ($= 0.9, 0.8$). These data is also of a longer period than that which presented by AP [28]. The 3- d results also conforms with our expectation, however only a short interval of data was available in the asymptotic limit. The late-stage behavior of the autocorrelation function, i.e., $f(\tau) \sim \tau^{-d/2}$ has also been reported in the literature. We mention the work of Hayakawa and Otsuki [29], who have calculated the autocorrelation function for the velocity field, shear stress, and the heat flow. They find that autocorrelation functions for the velocity field and shear stress obey as $f(\tau) \sim \tau^{-d/2}$ at long times.

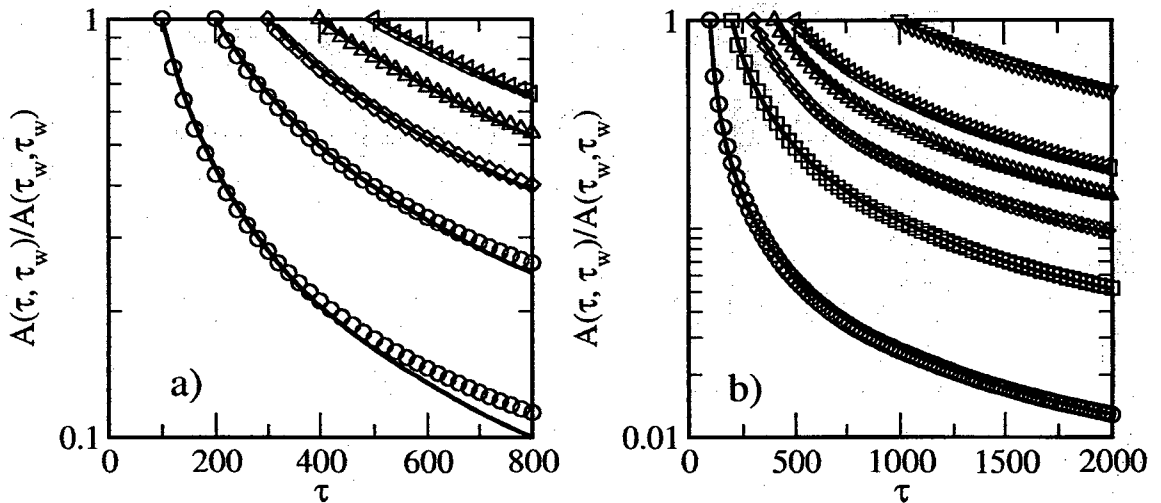


Figure 6.13: Autocorrelation functions for the $d = 2$ case with different values of the waiting time $\tau_w = 100, 200, 300, 400, 500$. We plot $A(\tau_w, \tau)$ vs. τ in log-linear scale. (a) corresponds to data for $e = 0.8$ and (b) corresponds to data for $e = 0.9$. The solid lines superposed on the data sets are the best fits to the function $f(\tau) = 1/[1 + a(\tau - \tau_w)^{-1}]$.

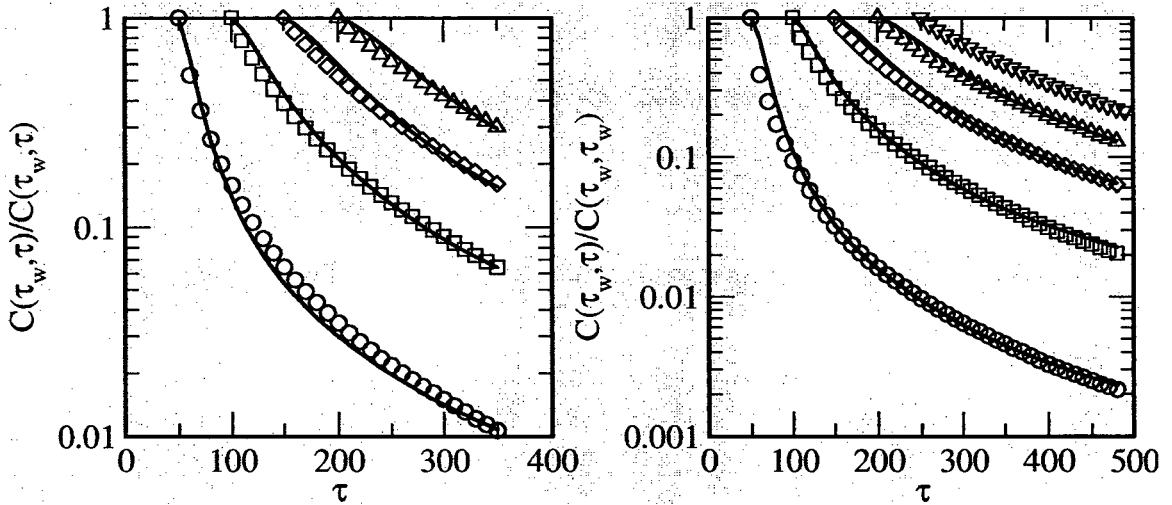


Figure 6.14: Autocorrelation functions for the $d = 3$ case with different values of the waiting time $\tau_w = 50, 100, 150, 200, 250$. (a) corresponds to data for $e = 0.6$ and (b) corresponds to data for $e = 0.8$. The solid lines superposed on the data sets are the best fits to the function $f(\tau) = 1/[1 + a(\tau - \tau_w)^{-3/2}]$.

6.4 Haff's Law in Polydispersed Systems

6.4.1 Differential Collision Frequency and Differential Collision Rate

This section generalizes Haff's law, taking into consideration polydispersity effects among grains. In previous sections, we had assumed that parameters like mass (m), coefficient of inelasticity (e), size of the grains (σ), etc. are identical for all grains. These parameters have an influence in the overall dynamics as they explicitly appear in various terms like velocity update [see Eq. (5.5)], collision frequency, etc. Thus it will be nice to see, how these parameters control overall dynamics. In this section, we will incorporate these differences and investigate the HCS with polydispersed grains. For simplicity, we consider the case where there are two types of granular particles.

We first present a brief derivation of differential collision frequencies and differential collision rates for hard sphere interactions. Then we will extend the theory including polydispersities of different kinds of granular materials in the succeeding sections.

The concept of collision frequency and collision rate plays an important role in the description of many particle systems. The derivation is done for kinetic theory of gas, however it can be successfully applied to dilute granular gas in HCS phase. We consider a simple model of elastic hard spheres, hence interaction radius can be defined as

$$\rho = (d + d_F) / 2, \quad (6.22)$$

where d is the diameter of a test particle and d_F is the diameter of field particle.

A collision would occur when separation between two particles or impact parameter (b) is smaller than the ρ . Next we consider a simple model, where a test particle is moving with constant velocity g and neighboring field particles remain stationary – see Fig. 6.15.

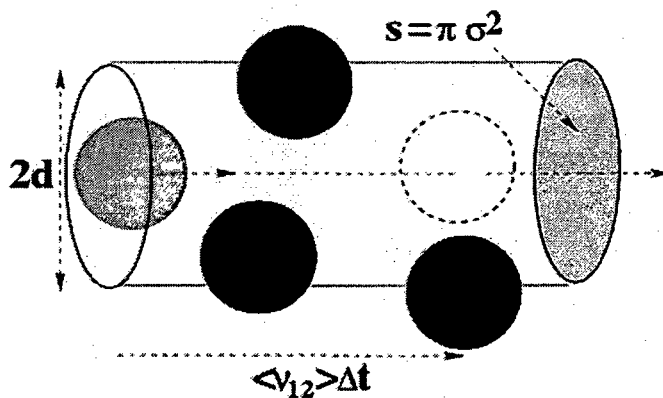


Figure 6.15: A simple model of collision cylinder of gray particle. Only those particle whose centers lie inside the collision cylinder of radius σ and length $\langle \vec{v}_{12} \rangle \delta t$ will collide with the gray particle.

The collision frequency for this simple model is

$$\mu = n_F g S, \quad (6.23)$$

where n_F is the density for the field particles, and $S = \pi \rho^2$ is the area of collision cross-section. Next we assume that there are group of test particles (N) with density n , and all of them moving with constant speed n , the collision rate now can be written as

$$\omega = \frac{N}{V} n_F g S = n n_F g S. \quad (6.24)$$

Here, the collision rate ω represents the total number of collisions per unit time and unit volume. The hard sphere collision model however does not consider the facts that test particles can have different velocities or field particles need not to be always stationary. Hence it is necessary to write collision frequency and collision rate in differential form. We also introduce differential cross-section $\sigma d\Omega$ and replace total collision cross-section S , where σ is differential collision cross-section and $d\Omega = \sin \theta d\theta d\phi$ is differential solid scattering angle with θ as the scattering angle and ϕ is azimuthal angle. We also assume that the distribution function of field particles is the Maxwell-Boltzmann distribution, i.e.,

$$f_0(\vec{v}_F) = \left(\frac{m_F}{2\pi k_B T_F} \right)^{d/2} \exp \left(-\frac{m_F v_F^2}{2k_B T_F} \right), \quad (6.25)$$

where v_F and m_F are velocity and mass for a field particle, k_B is Boltzmann constant, and T_F is the temperature. Hence differential collision frequency $d\mu$ for the test

particle can be written as

$$d\nu(v, v_F, \theta, \phi) = n_F f_0(\vec{v}_F) |v - v_F| \sigma \sin\theta d\theta d\phi dv_F, \quad (6.26)$$

where $\sigma = \rho^2/4$ is the differential collision cross-section for hard sphere interaction.

Further if we assume that velocity distribution of test particles is also Maxwellian, i.e.,

$$f_0(\vec{v}) = \left(\frac{m}{2\pi k_B T}\right)^{d/2} \exp\left(-\frac{mv^2}{2k_B T}\right). \quad (6.27)$$

Thus we can rewrite Eq. (6.24) and differential collision rate as

$$d\omega(v, v_F, \theta, \phi) = n n_F f_0(\vec{v}) f_0(\vec{v}_F) |v - v_F| \sigma \sin\theta d\theta d\phi dv_F dv. \quad (6.28)$$

Finally, integrating Eq. (1.7), we obtain the collision rate for hard-sphere interactions [30, 31]

$$\omega = n n_F v_{av} \pi \rho^2, \quad (6.29)$$

where the average relative velocity $v_{av} = \sqrt{8k_B T'/(\pi m)}$, and $T' = \mu(T/m + T_F/m_F)$.

If we assume homogeneous particles, i.e., $m = m_F = 1$, $T = T_F$, $d = d_F$, the collision rate can be simplified to

$$\omega = \pi n^2 d^2 \sqrt{8k_B T/\pi} \sim \sqrt{T}. \quad (6.30)$$

6.4.2 Case with Different Inelasticities

In this section, we consider a mixture of two different types of inelastic particles, labeled as A and B. The particles are identical in all other respect, except for the restitution coefficient e which characterizes their collisions. We also consider that

system contains N_A number of particles of type A and N_B number of particles of type B so that total number of particles are $N = N_A + N_B$. Therefore, we can identify different types collisions between the particles: AA, BB, AB, where the collision type is denoted by the label of particular interaction. Now the average energy loss for a particle i having velocity \vec{v}_i after an inelastic collision can be written as

$$\begin{aligned}\Delta E_{\alpha\beta} &= -\frac{1}{2}(1 - e_{\alpha\beta}^2) \frac{\langle \vec{v}_i^2 \rangle}{d} \\ &= -\frac{\epsilon_{\alpha\beta}}{d} E_{\alpha\beta},\end{aligned}\tag{6.31}$$

where $\alpha\beta$ denotes the particle interaction type, i.e., whether the collision is of type AA, BB or AB. So, we can write

$$\begin{aligned}\epsilon_{AA} &= (1 - e_{AA}^2), \\ \epsilon_{BB} &= (1 - e_{BB}^2), \\ \epsilon_{AB} &= (1 - e_{AB}^2).\end{aligned}\tag{6.32}$$

We also note that the collision rate $\omega(T)$, is independent of the coefficient of restitution e , Eq. (6.30). Thus average loss of energy of particles in time dt can be written as

$$\Delta E = -(\epsilon_{AA}P_{AA} + \epsilon_{BB}P_{BB} + \epsilon_{AB}P_{AB})\omega(T)\frac{E}{d}dt,\tag{6.33}$$

where P_{AA}, P_{BB}, P_{AB} are probabilities that the given collision be of type AA, AB or

BB, i.e.,

$$\begin{aligned}
 P_{AA} &= \left(\frac{n_A}{n_A + n_B} \right)^2, \\
 P_{BB} &= \left(\frac{n_B}{n_A + n_B} \right)^2, \\
 P_{AB} &= \frac{2n_A n_B}{(n_A + n_B)^2}.
 \end{aligned} \tag{6.34}$$

Finally, cooling law of the mixture is given by:

$$\frac{dT}{dt} = -(\epsilon_{AA}P_{AA} + \epsilon_{BB}P_{BB} + \epsilon_{AB}P_{AB})\omega(T)\frac{T}{d}. \tag{6.35}$$

Equation (6.35) is identical to the cooling law for homogeneous case Eq. (6.9) or Eq. (6.31). Therefore the earlier cooling law in real time t and collision time τ should both apply with a replacement

$$\epsilon' \rightarrow (\epsilon_{AA}P_{AA} + \epsilon_{BB}P_{BB} + \epsilon_{AB}P_{AB}). \tag{6.36}$$

In simulation we consider two types of particles with different e -values i.e., for A-A type collision $e_{AA} = 0.8$, for B-B type collision $e_{BB} = 0.9$, and for A-B type or B-A type collision $e_{AB} = 0.85$. Considering a 1 : 1 mixtures of particles Eq.(6.36) can be easily evaluated and the new slope of the Haff's law comes out to be $\epsilon'/d = 0.138$ in 2-dimension. Figure 6.16 shows plot of numerical result with Eq. (6.35).

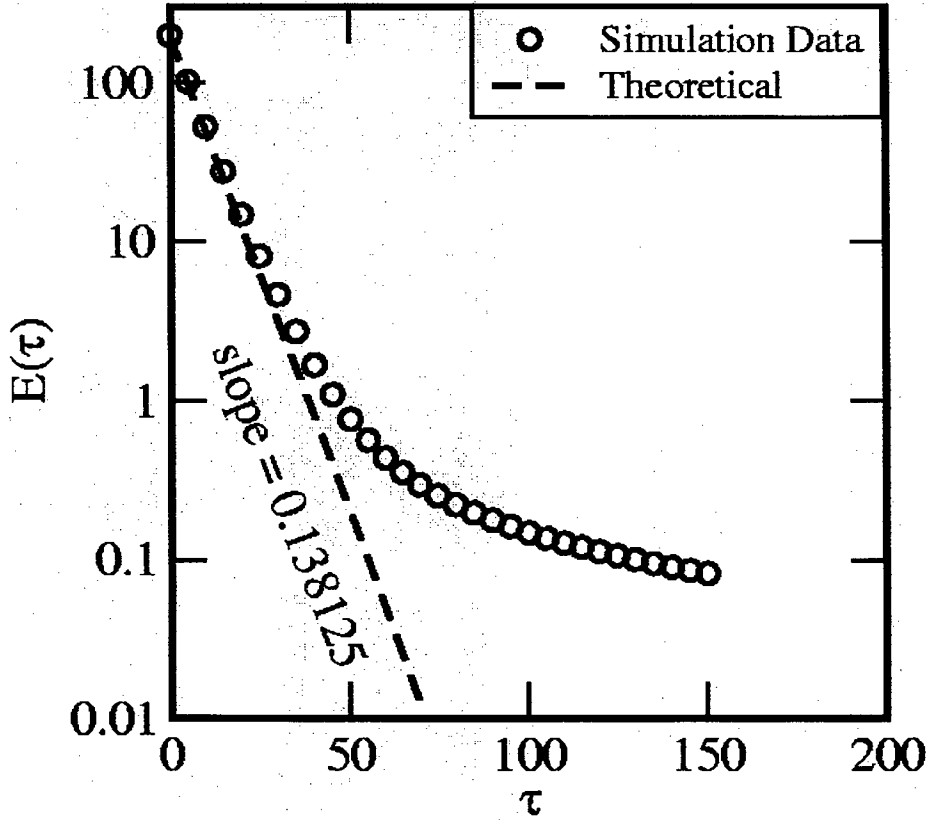


Figure 6.16: Time dependence of the granular temperature in $d = 2$ with different inelasticities, shown on a linear-log scale. We plot $E(\tau)$ vs. τ . The simulation is done with 1 : 1 mixture of two different types particles. We have taken $e_{AA} = 0.8, e_{BB} = 0.9, e_{AB} = 0.85$. The line denotes the generalized Haff's law for the mixture as calculated from Eq. (6.36).

6.4.3 Case with Different Masses

Next we consider inelastic particles labeled A and B; the particles are identical in all other respect, except that the masses of the particles are different. Again, we consider a mixture of particles of type A (n_A) and type B (n_B) in a 1 : 1 mixture. The velocity rule of colliding particles is

$$\begin{aligned}
 \vec{v}'_i \cdot \hat{n} &= \vec{v}_i \cdot \hat{n} - \left(\frac{m_j}{m_i + m_j} \right) (1 + e) [(\vec{v}_i - \vec{v}_j) \cdot \hat{n}] \hat{n}, \\
 \vec{v}'_j \cdot \hat{n} &= \vec{v}_j \cdot \hat{n} + \left(\frac{m_i}{m_i + m_j} \right) (1 + e) [(\vec{v}_i - \vec{v}_j) \cdot \hat{n}] \hat{n}.
 \end{aligned} \tag{6.37}$$

Thus, the average energy loss in one collision can be written by using Eq. (6.37) as

$$\begin{aligned} \Delta E_{ij} = & \frac{m_i}{2} \left[\frac{m_\mu^2 (1+e)^2}{m_i^2 d} (\langle v_i^2 \rangle + \langle v_j^2 \rangle) - \frac{2m_\mu (1+e)}{m_i d} \langle v_i^2 \rangle \right] \\ & + \frac{m_j}{2} \left[\frac{m_\mu^2 (1+e)^2}{m_j^2 d} (\langle v_i^2 \rangle + \langle v_j^2 \rangle) - \frac{2m_\mu (1+e)}{m_j d} \langle v_j^2 \rangle \right], \end{aligned} \quad (6.38)$$

where m_i is the mass of i^{th} particle and m_μ is the reduced mass of the colliding particles i and j , [$m_\mu = m_i m_j / (m_i + m_j)$]. This equation can be further simplified considering the type of collisions, i.e.,

$$\begin{aligned} \Delta E_{AA} &= -\frac{m_A (1-e^2)}{2} \frac{1}{d} \langle v_A^2 \rangle, \\ \Delta E_{BB} &= -\frac{m_B (1-e^2)}{2} \frac{1}{d} \langle v_B^2 \rangle, \\ \Delta E_{BB} &= -\frac{m_B (1-e^2)}{2} \frac{1}{d} (\langle v_B^2 \rangle + \langle v_B^2 \rangle). \end{aligned} \quad (6.39)$$

Considering an i^{th} particle of type A, it will lose energy when there is collision of type AA, i.e., the particle collides with another particle of type A, or it collides with other type of particle, viz. B. Hence loss of energy in time dt is

$$E_A = (P_A \Delta E_{AA} + P_B \Delta E_{AB}) \omega (T_A) dt, \quad (6.40)$$

where P_A is the probability that i^{th} particle, of type A, will collide with an A type particle, i.e., $P_A = n_A / (n_A + n_B)$ and P_B is the probability that it will collide with a B type particle, i.e., $P_B = n_B / (n_A + n_B)$.

Similarly for particle of type B we can write

$$dE_B = (P_B \Delta E_{BB} + P_A \Delta E_{AB}) \omega (T_B) dt. \quad (6.41)$$

Thus, we write the temperature relaxation for a particle as

$$\begin{aligned}\frac{dT_A}{dt} &= -\frac{(1-e^2)}{d} \left[\left(P_A + P_B \frac{m}{m_A} \right) T_A + P_B \frac{m}{m_B} T_B \right] \omega(T_A), \\ \frac{dT_B}{dt} &= -\frac{(1-e^2)}{d} \left[\left(P_B + P_A \frac{m}{m_B} \right) T_B + P_A \frac{m}{m_A} T_A \right] \omega(T_B),\end{aligned}\quad (6.42)$$

where $\omega(T)$ is the collision rate of the granular particles [Eq. (6.29)], which depend on the mass of the colliding particles. Finally, Eq. (6.42) are two coupled differential equations which can be solved numerically and simulation data has been compared in Fig. 6.17.

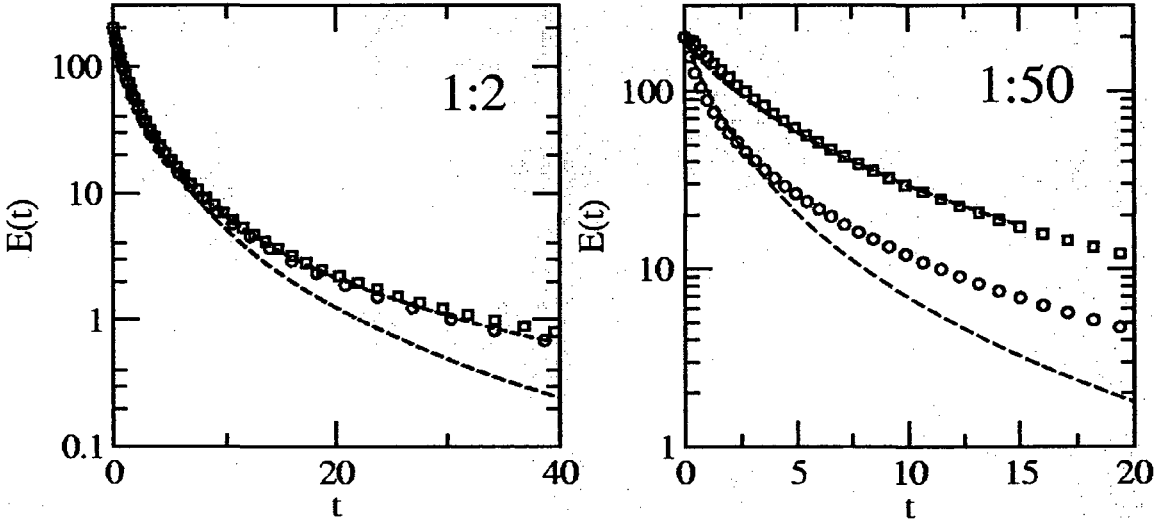


Figure 6.17: Time dependence of the granular temperature in $d = 2$ with different mass ratios, shown on a linear-log scale. We plot $E(t)$ vs. t . The simulation is done with 1 : 1 mixture of two different types particles. The line denotes the numerical solution for the mixture as calculated from Eq. (1.36) and Eq. (1.37).

6.4.4 Case with Different Initial Temperatures

Finally we consider a mixture (1 : 1) of two granular gases prepared such that initial temperatures of the species are different, i.e., A type gas having initial temperature T_A and B type gas has initial temperature as T_B and ($T_A > T_B$). However, velocity distribution of both the gas is Maxwellian and average momentum is set to zero. All other aspects of the grains remain identical.

Before we discuss granular grains, it is also interesting to review the elastic case, i.e., we first consider the grains collide elastically with each other. Elastic collision conserves energy and momentum. However energy exchange for a single collision can be calculated as [31]

$$\Delta E = k_B(T_B - T_A), \quad (6.43)$$

where we have considered grains with equal masses, $m_A = m_B$. Thus, it is found that energy exchange between different species of particle occurs, and the system finally reach an equilibrium state, where the final temperature is the mean of the initial temperatures,

$$T_{\text{final}} = \left(\frac{T_A + T_B}{2} \right). \quad (6.44)$$

This is known as *Newton's law of cooling* for an ideal gas. The thermal relaxation is exponential in nature which can also be verified from the numerical simulation. The evolution of the elastic gas is shown in Fig. 6.18(a). From dimensional analysis, it can also be argued that the decay constant λ depends on the mean temperature of the system:

$$\lambda \sim \sqrt{T_{\text{mean}}}. \quad (6.45)$$

Now we extend our simulation for the inelastic granular gases with different initial temperatures. The temperature relaxation is shown in Fig. 6.18(b).

Simulations indicate that there is a fast equilibration of temperature (Newton's cooling), and then the mixture follows the Haff's law, corresponding to the mean temperature of the system. Thus, two different time-scales of cooling are observed – the faster one corresponds to Newton's cooling and the slower one is Haff's cooling. Lastly we will show that these two time scales act independently of each other, i.e., Newton's cooling law in the early phase doesn't depend on the inelasticity of the granular gas and it's aspects follow that of elastic gas.

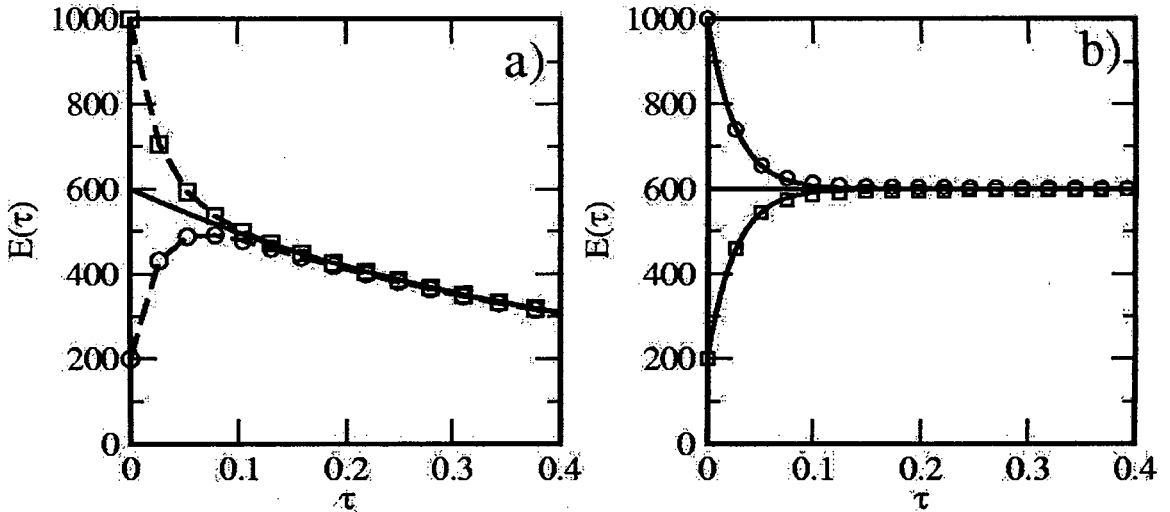


Figure 6.18: Time dependence of the granular temperature in $d=2$ with different initial temperatures mixtures. We plot $E(t)$ vs. t . The simulation is done with 1 : 1 mixture of two different types of particles, one being lower temperature 200 and the other at higher temperature 1000. Consequently mean temperature is 600. The coefficient of restitution being $e = 0.95$. (a) shows energy decay at the initial stage of such mixture. We have also superposed energy decay of a homogeneous system starting to evolve at mean temperature 600 (solid line). It is apparent from the graph that at long time scale two different curve superpose on each other and follow the mean temperature graph. (b) shows simulation of elastic gas prepared in same manner. It conserves the total energy of the system reflecting equilibration of temperatures only.

In view of the fact that Newton's cooling acts independent of that of the granular cooling law, we present the numerical data in tabular form. Various sets of temperature experiments have been done and the result has been compared with the elastic case.

Observations	Mean temp	Low temp	High temp	λ $e = 1$	λ $e=0.95$
Set 1	300	200	400	28.4865	28.5216
Set 2	600	200	1000	39.2228	39.3618
Set 3	1100	200	2000	51.8165	52.1926

Table 6.1: Data from simulations at various temperatures.

We also verify the Eq. (6.45) by evaluating the ratio of mean temperatures between any two sets and comparing it with the ratio of corresponding decay constant λ taken from Table 6.1, The equivalence of the data in Table 6.2 confirms that two cooling

Paring Of	Comparison of Mean Temperaure	Comparison of Decay Constant
Set 1 and Set 2	0.707	0.7246
Set 1 and Set 3	0.5222	0.5464
Set 2 and Set 3	0.7385	0.7542

Table 6.2: Data from simulations at various temperatures.

process (i.e., Newton's cooling and Haff's cooling) in the granular mixture having different initial temperatures are indeed independent of each other.

6.5 Summary and Discussion

We conclude this chapter with a summary and discussion of our results. There are two parts to this chapter. In the first part, we discuss pattern formation in freely-evolving

granular gases. This system loses energy through successive inelastic collisions. There are two regimes of cooling:

- (a) *Homogeneous cooling state* or HCS.
- (b) *Inhomogeneous cooling state* or ICS.

The HCS is an early phase of the dynamics, where the density remains uniform and the velocity field is flux-free. In the HCS, the energy decays exponentially with the collision time, which is known as Haff's law.

However, soon the system enters into the ICS, where there is a clustering of the density and velocity fields. The ICS is characterized by a slower decay rate of the energy. The clusters grow in size and evolution pictures suggest that the system obeys dynamical scaling, i.e., a single length scale can suitably describe the coarsening process. Using the analogy of phase ordering dynamics, we calculate various statistical quantities, e.g., the correlation function, structure factor, autocorrelation function, etc. The length scales are calculated from the correlation function, and show a universal growth law for $d = 2, 3$. Further, the tail of the structure factor is characterized by a generalized Porod's law [25]. Next, we focus upon the two-time autocorrelation function, which shows aging behavior. The autocorrelation function shows long-time tails in the collision time, $f(\tau) \sim \tau^{-d/2}$. This is consistent with the corresponding result for the elastic hard sphere gas.

In the second part of this chapter, we discussed the effect of polydispersity on freely-evolving granular gases. We considered granular mixtures with two different species having different, e.g., masses, inelasticity, and initial temperatures. The modification of Haff's cooling law has been discussed for these granular mixtures.

Bibliography

- [1] *Powders and Grains 97: Proceedings of the Third International Conference on Powders and Grains*, R. P. Behringer and J. Jenkins (eds.), Balkema, Rotterdam (1997).
- [2] *Powders and Grains 2001: Proceedings of the Fourth International Conference on Powders and Grains*, T. Kishino (ed.), Swets and Zeitlinger, Lisse (2001).
- [3] *Powders and Grains 2005: Proceedings of the Fifth International Conference on Powders and Grains*, R. Garcia-Rojo, H. J. Hermann and S. McNamara (eds.), Balkema, Rotterdam (2005).
- [4] J. Duran, *Sands, Powders and Grains*, Springer-Verlag, Berlin (2000).
- [5] N. V. Brilliantov and T. Poschel, *Kinetic Theory of Granular Gases*, Oxford University Press, Oxford (2004).
- [6] J. Rajchenbach, Phys. Rev. Lett. **65**, 2221 (1990); S. Das Gupta, D. V. Khakhar and S. K. Bhatia, Chem. Eng. Sci. **46**, 1531 (1991); Powder Technol. **67**, 145 (1991).
- [7] O. Zik, D. Levine, S. G. Lipson, S. Shtrikman and J. Stavans, Phys. Rev. Lett. **73**, 644 (1994).

- [8] S. Puri and H. Hayakawa, *Physica A* **270**, 115 (1999); *Physica A* **290**, 218 (2001).
- [9] F. Melo, P. B. Umbanhowar and H. L. Swinney, *Phys. Rev. Lett.* **75**, 3838 (1995);
P. B. Umbanhowar, F. Melo and H. L. Swinney, *Nature* **382**, 793 (1996).
- [10] G. Peng and H. J. Herrmann, *Phys. Rev. E* **49**, R1796 (1994); *Phys. Rev. E* **51**,
1745 (1995); O. Moriyama, N. Kuroiwa, M. Matsushita and H. Hayakawa, *Phys.*
Rev. Lett. **80**, 2833 (1998).
- [11] G. H. Ristow, *Pattern Formation in Granular Materials*, Springer-Verlag, Berlin
(2000).
- [12] H. M. Jaeger, S. R. Nagel and R. P. Behringer, *Rev. Mod. Phys.* **68**, 1259 (1996).
- [13] P. K. Haff, *J. Fluid Mech.* **134**, 401 (1983).
- [14] S. K. Das and S. Puri, *Europhys. Lett.* **61**, 749 (2003); *Phys. Rev. E* **68**, 011302
(2003).
- [15] S. R. Ahmad and S. Puri, *Europhys. Lett.* **75**, 56 (2006).
- [16] S. McNamara and W. R. Young, *Phys. Fluids A* **4**, 496 (1992); *Phys. Fluids A*
5, 34 (1993).
- [17] N. Sela and I. Goldhirsch, *Phys. Fluids* **7**, 507 (1995).
- [18] I. Goldhirsch and G. Zanetti, *Phys. Rev. Lett.* **70**, 1619 (1993); I. Goldhirsch,
M. -L. Tan, and G. Zanetti, *J. Sci. Comput.* **8**, 1 (1993).
- [19] S. McNamara and W. R. Young, *Phys. Rev. E* **53**, 5089 (1996).
- [20] S. Luding, M. Huthmann, S. McNamara and A. Zippelius, *Phys. Rev. E* **58**, 3416
(1998).

- [21] S. Luding and H. J. Herrmann, *Chaos* **9**, 673 (1999).
- [22] R. Brito and M. H. Ernst, *Int. J. Mod. Phys. C* **8**, 1339 (1998).
- [23] T. P. C. van Noije, M. H. Ernst, R. Brito and J. A. G. Orza, *Phys. Rev. Lett.* **79**, 411 (1997); T. P. C. van Noije, M. H. Ernst and R. Brito, *Phys. Rev. E* **57**, R4891 (1998); T. P. C. van Noije and M. H. Ernst, *Phys. Rev. E* **61**, 1765 (2000).
- [24] J. Wakou, R. Brito and M. H. Ernst, *J. Stat. Phys.* **3**, 107 (2002).
- [25] A. J. Bray and S. Puri, *Phys. Rev. Lett.* **67**, 2670 (1991); H. Toyoki, *Phys. Rev. B* **45**, 1965 (1992).
- [26] S. Luding and H. J. Herrmann, *Chaos* **9**, 673 (1999).
- [27] E. Ben-Naim and P. L. Krapivsky, *Phys. Rev. E* **66**, 011309 (2002).
- [28] S. R. Ahmad and S. Puri, *Phys. Rev. E* **75**, 031302 (2007).
- [29] H. Hayakawa and M. Otsuki, e-print no. 0706.3956.
- [30] S. Chapman and T. G. Cowling, *The Mathematical Theory of Non-Uniform Gases*, Cambridge University Press, New York (1970).
- [31] Y. Chang, *Phys. of Plasmas*. **10**, 12 (2003).

